UNIVERSITY OF CALIFORNIA

Los Angeles

Darkfield Imaging with a Plasmonic Focusing Lens:
Antenna Theory for
Near-field Scanning Optical Microscopes

A dissertation submitted in partial satisfaction of the

requirements for the degree Doctor of Philosophy

in Electrical Engineering

by

Japeck Tang

2009

The dissertation of Japeck Tang is approved.

Benjamin Williams

Giovanni Zocchi

Harold Fetterman, Committee Co-chair

Eli Yablonovitch, Committee Co-chair

University of California, Los Angeles

2009

TABLE OF CONTENTS

LIST OF FIGURES AND TABLES

ACKNOWLEDGEMENTS

First, I would like to thank Prof. Eli Yablonovitch for his guidance and support for the past few years in the investigation of the ideas in this dissertation.

I would also like to thank Prof. Harold Fetterman for agreeing to be a chair of the Doctoral Committee. I am also grateful to Prof. Benjamin Williams and Prof. Giovanni Zocchi for taking time out of their schedules to serve on the Doctoral Committee.

Next, I would like to thank my fellow lab members, past and present, who have helped me in my academic growth and contributed to this body of work. I would like to thank former lab member Josh Conway for starting the plasmonic dimple lens project, and fellow members of the plasmonic dimple lens fabrication team Shantha Vedantam and Hyojune Lee, who have done most of the fabrication of the plasmonic dimple lens. In particular, I would like to thank Shantha for her tutelage in the Nanolab and of fabrication procedures. I would also like to thank previous lab members Thomas Szkopek and Subal Sahni, as well as current lab members Xi Luo, Matteo Staffaroni, and Giovanni Mazzeo for their help and discussions.

Much of the fabrication in this project has taken place in the UCLA Nanoelectronics Research Facility (Nanolab). I would like to thank the Nanolab staff for their help: Steve Franz, Tom Lee, Hoc Ngo, Huynh Do, Ivan Alvarado, Wilson

Lin, and Joe Zendejas. I would also like to thank Sergey Prikhodko and especially Noah Bodzin for their help with the focused ion beam (FIB) work.

Lastly, I would like to thank all of the administrative staff who have made this possible. I am grateful to our group's administrators Jaymie Otayde-Mateo and Carmichael Aurelio, as well as the other administrative staff in the Electrical Engineering department.

Some of the material in this dissertation regarding the plasmonic dimple lens in Chapter 2 (in particular the figures) can also be found in the references listed in the Publications and Presentations section.

I would also like to acknowledge funding from the California NanoSystems Institute (CNSI), the Center for Nanoscience Innovation for Defense (CNID), and the NSF Nanoscale Science and Engineering Center for Scalable and Integrated Nanomanufacturing (SINAM).

VITA

August 23, 1982	Born, New Haven, Connecticut
2001	Summer Undergraduate Research Fellowship National University of Singapore Singapore
2002	Summer Undergraduate Research Fellowship Cornell University Ithaca, New York
2003	Summer Intern Mitsubishi Electric Advanced R&D Amagasaki, Japan
2004	B. S., Electrical and Computer Engineering California Institute of Technology Pasadena, California
2006	M. S., Electrical Engineering University of California, Los Angeles Los Angeles, California
2004-2009	Graduate Student Researcher Department of Electrical Engineering University of California, Los Angeles

PUBLICATIONS AND PRESENTATIONS

L. Chamberlain, J. Tang, M. Watugala, J. A. Adams, and M. Babish, "A Behavioral Architecture for Strategy Execution in the RoboFlag Game," 2003 American Controls Conference, (2003).

H. Lee, S. Vedantam, J. Tang, J. Conway, M. Staffaroni, and E. Yablonovitch, "Experimental Demonstration of Optical Nanofocusing by a Plasmonic Dimple Lens," in Plasmonics and Metamaterials, OSA Technical Digest (CD) (Optical Society of America, 2008), paper MMA2.

H. Lee, S. Vedantam, J. Tang, J. Conway, M. Staffaroni, and E. Yablonovitch, "Demonstration of a Plasmonic Dimple Lens for Nanoscale Focusing of Light," arXiv:0810.1553v1, (2008).

S. Vedantam, H. Lee, J. Tang, J. Conway, M. Staffaroni, J. Lu, and E. Yablonovitch, "Nanoscale Fabrication of a Plasmonic Dimple Lens for Nano-focusing of Light," Proc. of SPIE Vol. 6641, 66411J, (2007).

S. Vedantam, H. Lee, J. Tang, J. Conway, M. Staffaroni, and E. Yablonovitch, "A Plasmonic Dimple Lens for Nanoscale Focusing of Light," Nano Letters 9, 3447 (2009).

E. Yablonovitch, S. Vedantam, J. Tang, and M. Staffaroni, "Nanophotonic devices: spontaneous emission faster than stimulated (Invited Paper)," SPIE Optics + Photonics Conference 7395-77, (2009).

ABSTRACT OF THE DISSERTATION

Darkfield Imaging with a Plasmonic Focusing Lens:

Antenna Theory for

Near-field Scanning Optical Microscopes

by

Japeck Tang

Doctor of Philosophy in Electrical Engineering

University of California, Los Angeles, 2009

Professor Harold Fetterman, Co-chair

Professor Eli Yablonovitch, Co-chair

It is widely known that optical imaging is not strictly limited by the Rayleigh limit. Recently, a dimple-shaped plasmonic lens has been fabricated for focusing light to the nanoscale. This dissertation will begin with a discussion of the design, fabrication, and experimental measurements of this plasmonic dimple lens.

However, one of the drawbacks of the plasmonic dimple lens is that it is an open structure, so light from the input side is scattered and introduces noise into the output of the device. This background noise may be acceptable in some applications

that have an inherent threshold, such as for Heat Assisted Magnetic Recording (HAMR). In other applications, it may be desirable to have low background noise, such as for sensitive optical measurements, e.g. Near-field Scanning Optical Microscopes (NSOMs).

To this end, this dissertation subsequently presents the design, fabrication, measurement, and antenna model analysis of a novel darkfield plasmonic imaging device. There have been other approaches in literature that can also be considered to be darkfield devices, including the C-aperture structure and the bullseye pinhole. Although the device in this work can be viewed as a modification of the bullseye pinhole, this dissertation leverages the insight gained from the previously fabricated plasmonic dimple lens and couples it with an analysis via antenna theory to gain a better understanding of the limitations of NSOM probes.

Chapter 1 – Introduction

1.1 Motivation

Science has progressed from the macroscopic to the microscopic to the nanoscopic, and it has become increasingly difficult to interact with these new areas of study. In order for us to study the phenomena at each new level, we must be able to both modify the material being studied and subsequently observe the results of our modifications. Thus in order to push the limits of our scientific understanding and exploration, we must also develop new tools to assist in our studies at smaller and smaller sizes. Furthermore, the smaller size of the objects being studied leads to increased sensitivity to low levels of energy (e.g. a small number of photons for optical measurements or small forces/displacements for force measurements). This in turn engenders a need for eliminating any sources of noise, such as any stray background light in sensitive optical measurements.

Optical techniques are among the most well-established methods of observing objects, including those not visible to the naked eye. By comparison, other imaging techniques such as atomic force microscope (AFM) [1], transmission electron microscope (TEM) [2], and scanning electron microscope (SEM) [3] are relatively new. Although these newer techniques have better spatial resolution, optical techniques for probing a sample still retain some appeal in many applications.

For example, optical techniques can often be done without any alterations to the sample. These alterations can include sample damage due to contact imaging methods, or sample modifications for transparency/conductivity as required by electron microscopy. Thus, optical imaging has provided a method for non-invasive, in vivo imaging, with a history dating back to the use of microscopes for observing microorganisms, binoculars for watching birds, and telescopes for viewing the stars. Optical imaging can also be used for the imaging of light-sensitive samples, such as fluorescent markers in live cells [4], or to observe interactions between subcellular components via fluorescence resonance energy transfer (FRET) [5, 6]. Both of these methods provide information about the functionality of the still living specimens being studied, which is beyond just the physical characteristics (e.g. topology or density) that could be measured via other techniques.

Conversely, optical techniques can also be used for affecting changes in materials at various levels. One prime example of this is the patterning of photoresist in the semiconductor industry, where the absorption of light in unmasked areas during the exposure step increases the resist's solubility in a developer [7, 8]. Another example from biology is the use of optical tweezers [9, 10] to interact with DNA and proteins, which allows one to move molecules and to measure the forces acting upon them [11]. Another application that uses light to interact with a sample is the use of optical techniques for focusing energy to heat a sample. For example, laser surgery or laser ablation can use focused laser light to destroy or remove material. A less-conventional example of focusing energy is for heat-assisted magnetic recording (HAMR), where light is focused to a small spot to heat the magnetic material in hard drives [12, 13, 14, 15]. One can also apply this hard drive heating technology to photolithographic applications to create nanoscopic patterns in a resist material [16].

These optical interactions, both for modifying and observing a sample, can be tailored via material properties that are typically dependent upon the wavelength of light being used. In particular, the two most useful material properties are the material's refractive index and absorption coefficient (e.g. the real and imaginary parts of the material's dielectric constant for bulk materials [17] or absorption spectra for fluorescent dye molecules). A more recently discovered optical phenomenon, known as surface plasmon polaritons [18, 19], provides an additional range of ways to modify optical properties, including allowing for plasmonic versions of existing optical methods such as plasmonic optical tweezers [20]. A more detailed introduction to surface plasmons in general can also be found in Chapter 2. Higher order nonlinear interactions and other more complicated effects, including lasing, can also have interesting applications, even in plasmonics [21, 22, 23], but are outside the scope of this dissertation.

Although some applications for optical focusing such as photoresist and HAMR have inherent thresholds for changes due to the absorption of optical energy, optical sensing applications are more sensitive to stray light, especially considering the low throughput of many aperture-based sensing elements, as will be discussed in Chapter 3. Objects with small volumes can have interactions involving small amounts of energy. Furthermore, small objects do not radiate efficiently [24], which increases the difficulty of detecting signals. Thus, light from other areas of the sample may easily overwhelm the desired signal if the measurement system is not carefully designed to be "darkfield" by reject signals from outside the area of interest.

In summary, optical techniques have proven to be a reliable method for both observing and interacting with materials at the microscopic scale, and thus it is desirable to further extend these methods into the nanoscale. There have been many methods already proposed to accomplish this task, as will be discussed in the subsequent two sections of the introduction. However, each method has its own limitations. Thus, in order to improve upon existing optical focusing methods, two obstacles are considered in this dissertation: the limitations of optical resolution and the inability to detect low levels of light due to low throughput and background noise.

1.2 Focusing to the nanoscale

Optical imaging provides a unique method of interacting with certain specific properties of the materials being investigated. The utility of optical imaging, despite the invention of newer imaging methods [1, 2, 3], provides an incentive for improving upon one of its major limitations – that of its resolution. Traditionally, optical resolution, such as that of microscope objectives, has been limited by diffraction to the Rayleigh limit, approximately $\lambda/2n$ for light with a wavelength of λ in a medium with refractive index n [25]. For visible wavelengths in typical mediums, this limits the resolution to on the order of 100-200 nm.

One obvious method for improving optical resolution is to decrease the diffraction limited spot size. For example, the semiconductor industry has switched to shorter wavelength UV light to improve their resolution [26], and Intel plans to have 32 nm logic technology in production this year (2009) [27]. However, it might be preferable in other applications to continue to operate in the visible region, thereby retaining the aforementioned benefits with respect to material properties.

Besides changing the wavelength of operation, one could also increase the refractive index in order to decrease the spot size. This effect is of limited use in natural bulk materials, since materials that do not have significant optical absorption also have limited refractive indexes. However, tailored materials such as metamaterials can have high effective refractive indexes [28], while limiting the absorption losses. Similarly, one can view the surface plasmons discussed in Chapter 2 as modes propagating in a medium with a high effective refractive index [29], since the surface plasmons can have wavelengths much shorter than their corresponding free-space wavelengths [30, 31]. This reduction in wavelengths for surface plasmons is the basis of the work presented in this dissertation. There are even some surface plasmons that can be considered to have negative refraction [32].

An alternative method of focusing optical energy to the nanoscale is to utilize the enhancement of electric fields found near sharp metal tips. For non-optical measurements, the scanning tunneling microscope (STM) is one method which uses a sharp metal tip to cause current to tunnel through an insulating barrier (i.e. a vacuum gap) [33]. In the optical regime, a metallic tapered structure has been found to support surface plasmons that propagate to the tip, where they form a strong electric field at optical frequencies [34, 35]. Some more examples from the literature that use metal tips to create strong electric fields are the C-aperture [36, 37], bowtie apertures [38, 39], and bowtie structures [40]. In fact, even two closely spaced conducting surfaces, such as those of a capacitor, pinhole [41, 42, 43], or in a coaxial structure [44], can support a high electric field in the space between them. The plasmonic dimple lens concept described in Chapter 2 also utilizes this phenomenon to confine optical energy to a small gap between two conductors at its output.

1.3 Darkfield imaging

Since noise becomes a more serious issue for low signal levels at the nanoscale, it is necessary to decrease the noise by using a darkfield structure to limit the light coming from outside the area of interest. This is analogous to darkfield illumination in microscopy for improving contrast, where oblique angle illumination allows detection of only signal scattered from the interesting features of the sample while having no signal anywhere else [45]. Unfortunately, all of the aperture-based optical methods mentioned in the previous section, including the plasmonic dimple lens, are not truly darkfield since they have open areas adjacent to the focal spot that can allow extra light to be input to or extracted from a sample.

The solution to this, which has the drawback of decreased throughput, are aperture structures such as the metallized tapered fiber probes used in near-field scanning optical microscopy (NSOM) [46, 47] and pinhole-based devices, such as bullseye structures [39, 42, 43, 48], both of which are darkfield optical methods. Although the C-aperture is also mostly darkfield, it can be viewed as a tradeoff between a pinhole with low throughput and an open structure with just a sharp tip that has large amounts of background light. In contrast, this dissertation demonstrates an approach based on aperture devices to increase throughput without also allowing more background light through, thereby maintaining a completely darkfield device. This darkfield focusing device will be discussed in Chapter 3.

In addition to the enhanced electric fields found near metallic structures, the evanescent decay of electric fields into good conductors, as commonly considered for radio frequency (RF) and microwave electromagnetic radiation [49], helps to confine optical energy to a nanoscopic spot by preventing the leakage of light away from the exposed areas. This is the principle behind coating pulled fiber probes with metal for NSOM, as well as a key factor for the small spot size of the plasmonic dimple lens. There has also been work done on metal coated fiber tips without apertures [50, 51], but these devices must have a thin metal coating to allow energy to couple from inside the fiber through to the outside of the tip. Thus, light can still penetrate these metal films, and like metal-only tips [34, 35], these apertureless metal-coated fiber tips are not truly darkfield.

Although the metal layers of the dimple lens help to limit the spot size in one direction, the reason that the dimple lens is also not completely darkfield is because it does not have metal completely surrounding the focal spot. The presence of a thick metal film is a key factor for limiting background light, since light penetrates poorly through a good conductor. This allows one to make darkfield devices by using metal to block out the light from unwanted areas. Thus, the darkfield plasmonic lens improves upon the dimple lens by ensuring there is enough metal to block light outside the focal spot.

In addition to NSOM and surface plasmons, there have also been several other recent methods to improve the resolution of optical imaging beyond the diffraction limit. These methods do not necessarily focus light to the nanoscale, but they can obtain nanometer precision for measuring the location of light sources, while also having limited noise. For example, stimulated emission depletion (STED) [52] utilizes light to cause stimulated emission, which localizes the source of fluorescence to a small known area by preventing spontaneous emission from occurring outside of that area. Two more methods that also do not need a near-field probe are stochastic optical reconstruction microscopy (STORM) [53] and photoactivated localization microscopy (PALM) [54], which are both able to determine the locations of statistically sparse light sources with high precision. These methods are also essentially darkfield due to the suppression of light away from each effective point source.

However, for more general purpose imaging applications, a scanning near-field method is more versatile for measuring and transmitting arbitrary optical signals to interact with a sample. Thus, the approach presented herein to increase optical resolution is to exploit the interesting properties of surface plasmons by applying them to a new type of NSOM probe in order to maintain a darkfield measurement method.

1.4 Layout of the dissertation

In this chapter, we gave the background and motivation for this work, as well as a brief overview of existing techniques in this field. Chapter 2 will discuss the plasmonic dimple lens. The plasmonic dimple lens project was a group effort to create a device for efficient focusing of optical energy to the nanoscale. It began with the design and simulations of Josh Conway [55] and culminated in the fabrication and measurement of the first plasmonic dimple lens device by Hyojune Lee and Shantha Vedantam [56, 57]. For the plasmonic dimple lens, this dissertation will only go into some depth regarding the bulk silicon removal step of the fabrication process, which was my primary contribution to this project. For more detailed information about the plasmonic dimple lens, please refer to the references and publications.

Chapter 3 will discuss the darkfield plasmonic focusing lens, which was an idea that came out of the plasmonic dimple lens project as it became apparent that there would be a need for preventing background light while focusing to a nanoscale spot. That is, there are some applications where it is desirable to be "darkfield" – to have light only at the focal spot, but no scattered or background stray light anywhere else. This darkfield device will be the primary focus of this dissertation, from the design and analysis of the device to the fabrication and measurements of a proof-of-concept test structure. The analysis of this darkfield device also provides an interesting perspective on the theoretical limits of NSOM probes via antenna theory.

Chapter 4 will conclude with an overview of the two projects as well as comments on the insights gained along the way.

Chapter 2 – Plasmonic Dimple Lens

2.1 Background and motivation

As was discussed in the introduction, one of the major limitations of optical measurements is the resolution. This encompasses both the difficulty of focusing light to smaller than a diffraction-limited spot, and that of distinguishing between light sources that are more closely spaced than the Rayleigh criterion, due to their Airy diffraction patterns [25]. There have been several methods for focusing light to the nanoscale, but many are still lacking in throughput and/or resolution.

Meanwhile, surface plasmons have been shown to possess short wavelengths at optical frequencies [18]. Thus, in order to overcome the resolution limit of typical optical techniques, Conway proposed the use of a dimple-shaped surface plasmon focusing lens to efficiently focus optical energy to the nanoscale [55]. Such a device could be used both for focusing light to the nanoscale, as well as for extracting light locally from a nanoscale spot. Thus, the dimple lens device would allow efficient optical access to the nanoscopic world.

Since the plasmonic dimple lens is a sub-wavelength device, it can also be viewed via circuit theory, analogous to RF and microwave electronics. The metal at the focal spot of the lens acts as a sub-wavelength antenna, which radiates poorly to the far-field but can interact strongly in the near-field. This tiny antenna is connected to a grating coupler via a tapered transmission line. More about the transmission line theory of the plasmonic dimple lens can be found in reference [55], and a similar tapered structure can also be found in reference [58]. The grating coupler then acts as a larger antenna that converts between surface plasmons and free space electromagnetic radiation. Thus, the device overall effectively acts as both a receiving and transmitting antenna for matching free space light to a nanoscopic light source at the focal spot. Another example from the literature that relates these devices to antenna theory is where a pinhole is paired with a grating that acts as an antenna to control the directionality of its output [43, 59]. More about the antenna theory of such devices can be found in Chapter 3.

2.2 Theory and design

Surface plasmons are electromagnetic modes bound to the interface between a dielectric and a metal, where the real parts of the dielectric constants of the two materials are $\varepsilon'_d > 0$ and $\varepsilon'_m < -\varepsilon'_d$, respectively. These modes can have short wavelengths and hence a small spatial size, while still oscillating at optical frequencies. The dispersion relations for such modes in a lossless Au–SiO_2 system are shown in Figure 2-1, which are similar to that of the theoretical and experimental dispersion curves for various metal–insulator–metal (MIM) systems found in references [31, 55, 60].

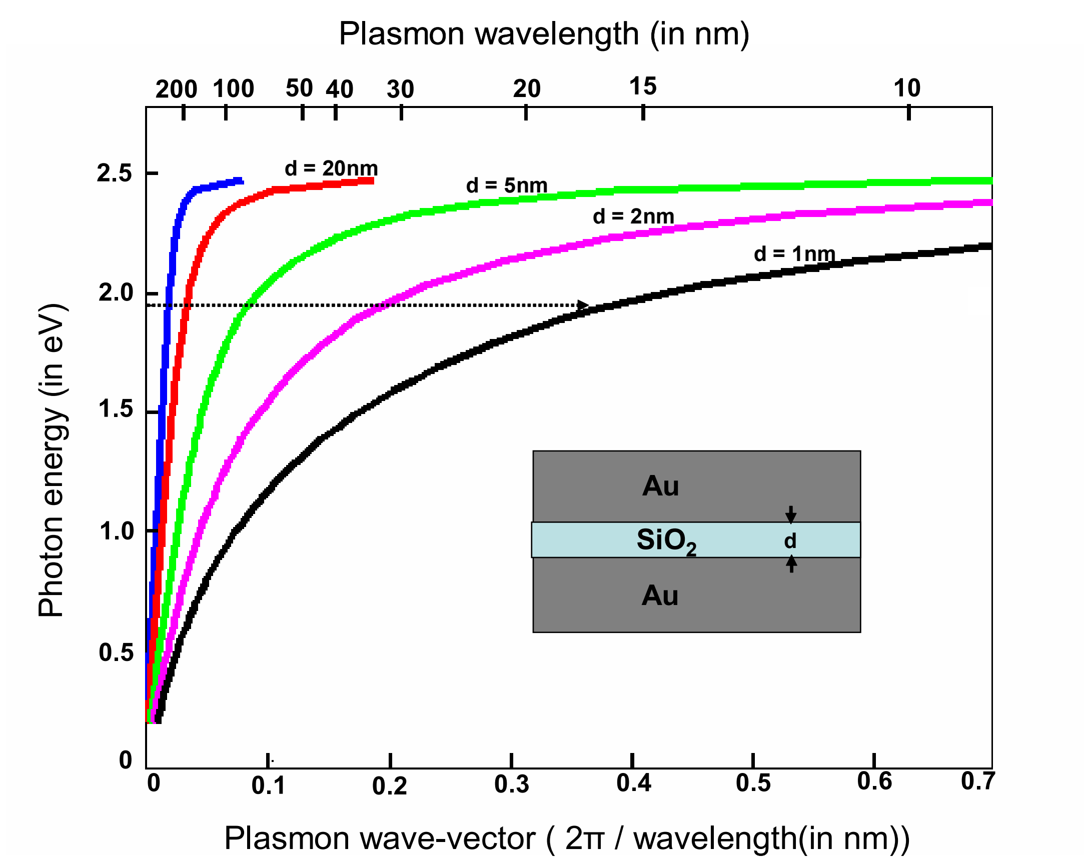

Figure 2-1. Au-SiO_2-Au dispersion relations
Calculated dispersion relations for the Au-SiO_2-Au stack for various thicknesses of the SiO_2 layer.

The spatial wavelength of single-sided surface plasmons is determined only by the dielectric constants of the two materials, which vary as a function of optical frequency. In general, the dielectric constants of transparent dielectric materials are relatively constant over the visible frequency range. In contrast, the real part of the dielectric constant for metals can vary greatly over this range, which gives rise to a resonance in the propagation constant k as a function of frequency, as $|\varepsilon'_m| \to \varepsilon'_d$. In order to obtain short wavelengths with single-sided surface plasmons, one would have to operate near this resonant single-sided surface plasmon frequency, which often coincides with increasing losses in the metal (i.e. as the real part of the dielectric constant $\varepsilon'_m \to 0$, the imaginary part ε''_m also increases and becomes large compared to ε'_m). In this regime, surface plasmon modes cannot propagate very far due to the losses in the metal. Since the losses in metal are a significant consideration in the design of the plasmonic dimple lens, metals with high conductivity (low loss) were compared for this device via their material Q factor, which is roughly dependent on the ratio of the real and imaginary parts of the metal's dielectric constant, $\varepsilon'_m/\varepsilon''_m$. As shown in reference [55], silver and gold are the two best candidates for the metal layers in terms of their material Q factors in the visible frequency range. The metal material properties in this work were taken from the optical dielectric constants found in references [61, 62, 63].

Double-sided surface plasmons (also called gap plasmons [58]), on the other hand, can have very short spatial wavelengths at a fixed frequency by scaling down the thickness of the dielectric spacing between the two metal layers. Thus, by using a lower frequency to limit propagation loss, one can still obtain a short spatial wavelength by decreasing the thickness of the dielectric spacer. These high k-vector modes allow for confinement of optical frequency light to nanoscale dimensions.

The plasmonic dimple lens utilizes this property of double-sided surface plasmons in order to focus optical energy to the nanoscale. A schematic of the plasmonic dimple lens is shown in Figure 2-2. In this device, a circular in-coupling grating is used to first couple free space light to a single-sided surface plasmon. The periodicity and height of the grating are chosen through theory and simulation. An optimized grating coupler can theoretically give up to ~50% efficiency in converting free space light into surface plasmons [64]. A linearly tapered structure with an optimized angle is then used to focus the light into high k-vector double-sided surface plasmons, thereby focusing the light to a nanoscale spot with as low as ~50% losses down the taper [55]. Additionally, there is an intermediate conversion step necessary for the single-sided surface plasmons generated by the grating to become double-sided surface plasmons in the taper, which also can have at most ~50% efficiency with our current geometry [55]. We did not make any attempt to optimize the efficiency of this conversion step.

The theoretical maximum efficiency for the power output, neglecting any propagation losses outside of the taper region (i.e. if the grating is far from the taper, or if there is a long narrow channel at the focusing end of the taper) would be the product of the above three steps. Thus, the best efficiency one can expect for such a device is that ~12.5% of the power input to the grating from free space would make it to the end of the taper. Please see reference [55] for additional information about the design of the plasmonic dimple lens.

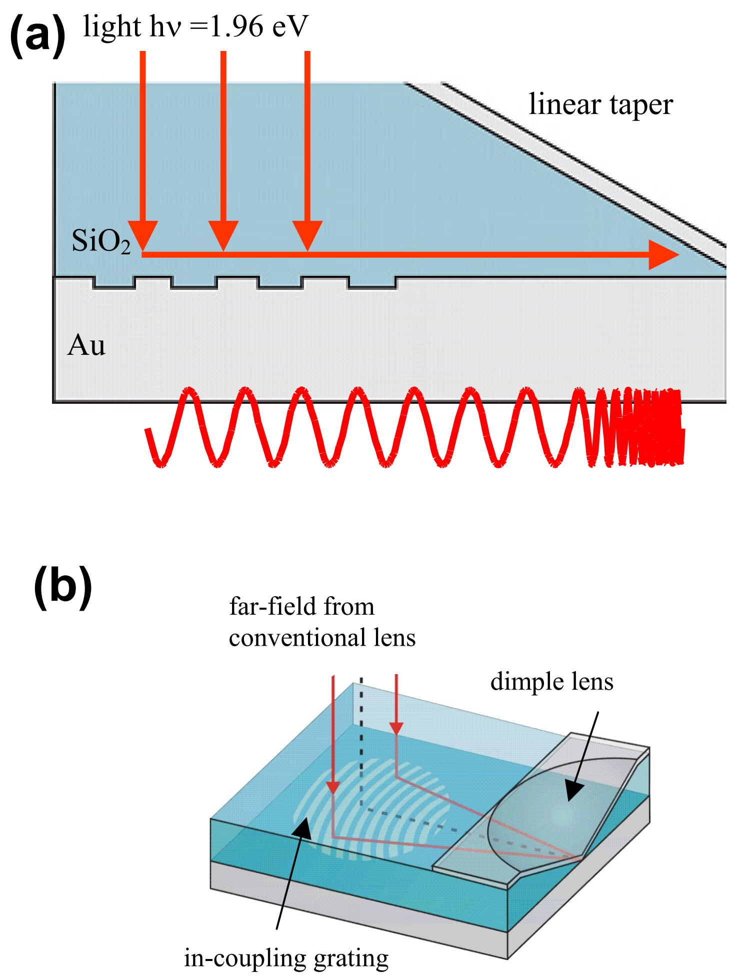

Figure 2-2. Dimple lens schematics
(a) Cross-sectional view schematic of the plasmonic dimple lens. Thickness of SiO2 layer tapers in vertical direction. (b) Perspective view of the plasmonic dimple lens.

As a comparison, pulled-fiber NSOM probes have very poor throughputs for small apertures, which can range from approximately 10^{-6} to 10^{-8} as the aperture sizes decrease from 100 nm to 50 nm [65, 66]. In part, this is due to the fact that experimental far-field measurements have low throughput because of poor radiation from small apertures. As will be discussed in Chapter 3, small apertures have radiation that has a quartic dependence on the aperture size [67, 68]. However, typical NSOM probes also have long tapers due to their small taper angles. So, there are significant propagation losses for when the fiber width is below the mode cutoff size, because the power decays exponentially with the length of the fiber beyond this point. This exponential decay in power down the tapered fiber occurs before it reaches the end and radiates to the far field, and is the analogue to the 12.5% maximum efficiency discussed above for the plasmonic dimple lens.

2.3 Fabrication considerations

In designing the fabrication scheme for the plasmonic dimple lens, there were four major considerations. Since the dielectric spacer thickness at the output determines the final spot size of our structure, it is desirable to be able to control this thickness to a few nanometers. Thus, we decided to use Low-Pressure Chemical Vapor Deposition (LPCVD) to provide a high-quality, thin, smooth layer for our dielectric.

The second consideration is that the metal–dielectric interfaces supporting the surface plasmon should be relatively smooth to minimize scattering losses. Since the roughness of the exposed surface for evaporated gold and silver is typically ~2-3 nm rms due to grain formation [69, 70], our fabrication process was designed so that surface plasmons would be propagating only on interior surfaces, where the smoothness is determined by the dielectric that the metal is evaporated against. In order to have two such smooth surfaces, it is necessary to release the dielectric film from its substrate to allow for evaporation from the other side. Since we used silicon as our substrate, we therefore had to have a bulk silicon removal step, which will be discussed in more detail in Section 2.5.

The third fabrication consideration is the shape of the tapered region of the dimple lens. Although we were unable to precisely control the angle or shape of the tapered dielectric layer, we were able to obtain a suitably tapered shape in polymethylmethacrylate (PMMA), a dielectric polymer. Using a grayscale exposure with electron-beam (e-beam) lithography, we obtained a dimple-shaped depression in the developed PMMA layer, which had a taper angle within the optimal range as determined by simulations [55].

The final consideration for the dimple lens device is that the out-coupling facet should be smooth and exactly at the center of the dimple lens. For this requirement, we chose to use an edge-polishing technique, similar to the polishing method already used in the hard drive industry for the fabrication of read heads [71]. Although the material Q of silver is better than that for gold (i.e. it is less lossy) [55], this polishing step also limited us to the use of gold for our metal layers due to excessive roughness when we attempted to polish silver layers (possibly due to corrosion).

2.4 Fabrication procedure and results

In light of the above considerations, we designed the process flow shown in Figure 2-3. This fabrication sequence is also found in references [56, 57]. A discussion of the fabrication issues we encountered can also be found in reference [72]. Appendix A provides a summarized list of the specific steps for most of the process flow, except neglecting the detailed parameters for the three e-beam lithography steps and the final mechanical edge-polishing step.

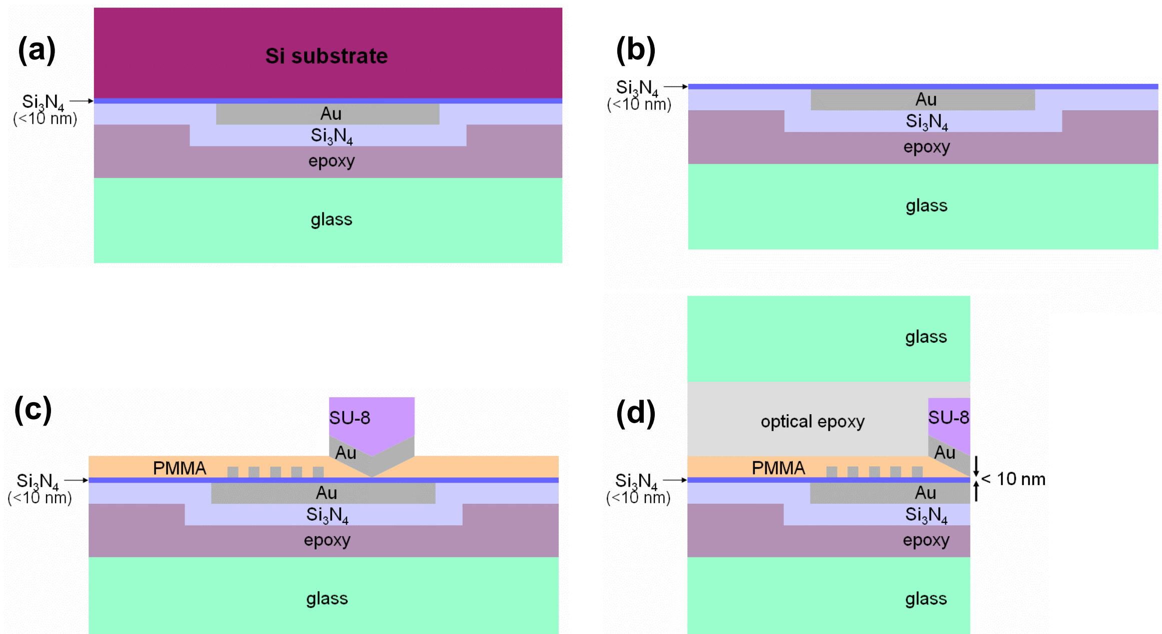

Figure 2-3. Fabrication sequence for dimple lens
(a) Au islands patterned on 10 nm LPCVD SiN on a Si-substrate. These islands are coated with 300 nm of PECVD SiN and bonded to a glass piece using silica-filled epoxy. (b) Si-substrate is completely etched away with HF+HNO_3 after thinning it down with DRIE process. (c) Semi-circular grating coupler and dimple profile in PMMA are patterned with e-beam lithography and second layer of Au is deposited and patterned. (d) The sample is bonded to glass using optically transparent epoxy and this stack is mechanically polished from one edge until the point when the circular dimple profile in PMMA is polished halfway through.

First, approximately 10 nm of LPCVD silicon nitride was deposited on a 300 μm thick double-side polished silicon wafer. This thin LPCVD silicon nitride serves as our critical dimension at the center of the dimple structure. Gold islands were then patterned on this smooth silicon nitride surface using photolithography, e-beam evaporation, and a liftoff process. These islands constitute the lower layer of gold in the gold–dielectric–gold stack shown in Figure 2-2a. These gold islands also include both the alignment markers for subsequent e-beam lithography steps, as well as the endpoint detection markers for the final edge-polishing step.

About 300 nm of plasma-enhanced chemical vapor deposition (PECVD) silicon nitride was then deposited on top of the gold islands to reduce the stress on the thin LPCVD silicon nitride during the forthcoming bulk silicon removal step. The patterned side of the sample was then bonded to a glass piece using a silica-filled low stress thermally cured epoxy (Optocast 3408) for support during the bulk silicon removal, resulting in the stack of materials shown in Figure 2-3a. The bulk silicon was thinned down from the exposed backside to less than 50 μm thickness using deep reactive ion etching (DRIE). The remaining silicon was removed using a wet etch comprised of a mixture of 1 part HF to 1 part HNO_3 (Figure 2-3b). This isotropic silicon wet etchant was chosen for its fast etch rate and high selectivity between silicon and silicon nitride. This bulk silicon removal step will be discussed in more detail in Section 2.5.

E-beam lithography, e-beam evaporation, and a liftoff process were then used to pattern a semi-circular gold grating of 30 nm height and 390 nm period on the newly exposed silicon nitride layer, above the gold islands. A circular dimple profile was then formed in a 100 nm layer of PMMA using a single spot exposure in e-beam lithography. Both the grating and the dimple were inspected using SEM and AFM, as can be seen in Figure 2-4. A 100 nm layer of gold was then evaporated on top of the dimple-containing PMMA layer using e-beam evaporation. This gold layer serves as the upper layer of the gold–dielectric–gold stack shown in Figure 2-2a.

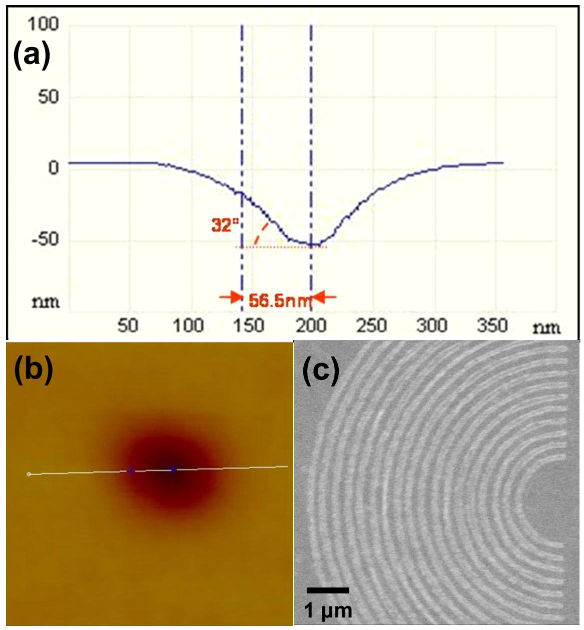

Figure 2-4. PMMA dimple and grating coupler
(a) Cross section and (b) surface scan acquired from the topographic AFM scan of the dimple profile in PMMA. The size of the scan is 400 nm x 400 nm (c) SEM image of the circular grating coupler.

In order to grant optical access to the gold grating coupler, the upper gold layer above the grating was then etched away using an argon ion dry etch with e-beam lithography patterned SU-8 resist as a mask, as shown in Figure 2-3c. The structure was then bonded to another piece of glass using optically transparent UV-curable epoxy (Norland 81) for additional support during the final edge-polishing step. Lastly, the sample was edge-polished until the center of the dimple was exposed at the facet, resulting in the final device shown by the schematic in Figure 2-3d.

The dimple region of the polished exposed facet was then scanned using AFM to inspect the quality of the polishing. The topographic and phase images of this AFM scan are shown in Figure 2-5. These scans show that there is approximately 1 nm of roughness in the polished end facet, with 5-10 nm steps between the different layers, which is due to varying material removal rates during polishing and possibly also swelling in the organic layers due to their exposure to an aqueous polishing environment.

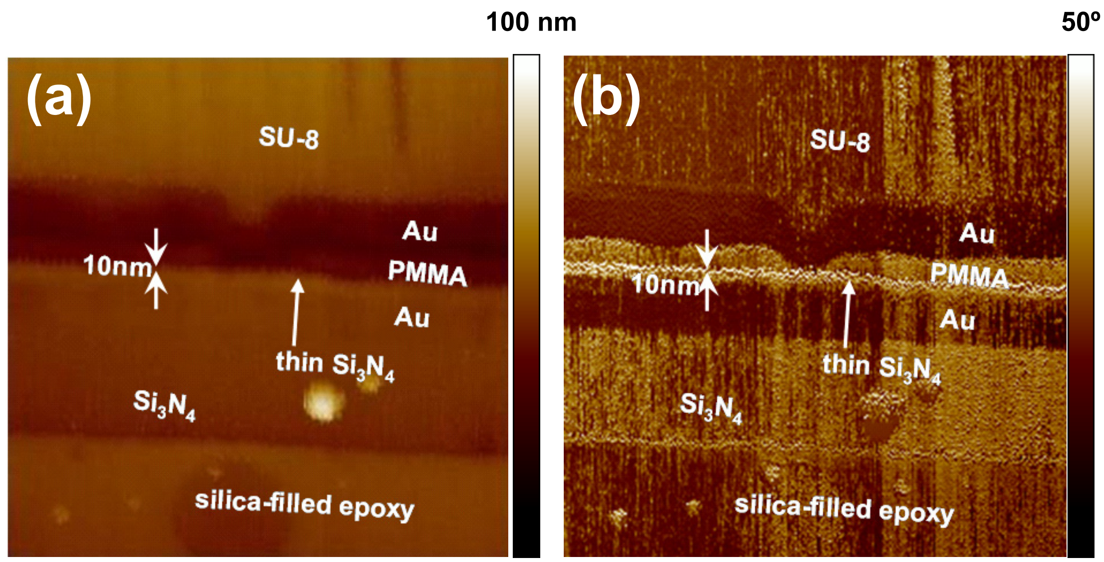

Figure 2-5. AFM scan of polished facet
(a) Topographic and (b) phase-shift AFM image of the out-coupling edge after mechanical edge-polishing. The size of the scan is 1.5 µm x 1.5 µm. Good polishing results with minimal polishing relief make distinguishing different layers in the topographic image difficult. Phase-shift image makes identification of different layers possible.

As a comparison, these layers have a differential thermal expansion of approximately 1 nm/ºC due to increase in temperature when a 10 µm square area is heated (i.e. from exposure to laser light and the subsequent thermal conduction). The linear thermal expansion coefficients, α, found in reference [73] were used for this estimate since the layers are constrained to expand in only one direction. Ceramic materials typically have $\alpha < 10\text{x}10^{-6}$ K^{-1}, whereas polymers can have α around 50-100x10^{-6} K^{-1}, with metals falling in between the two. Thus assuming ceramics have negligible expansion, we use the maximal value for the polymer PMMA from reference [74] as an upper bound for the difference in expansion coefficients. Thus, for $\Delta\alpha = \alpha_{PMMA} = 100\text{x}10^{-6}$ K^{-1}, $\Delta T = 1$ºC, and $L_0 = 10$ μm, the differential thermal expansion is calculated as $\Delta L = \Delta\alpha \cdot \Delta T \cdot L_0 = 1nm$.

The post-polishing AFM scans were used to assess the quality of the polishing as well as determine the endpoint for terminating the polishing step. The difference in quality of polishing when using silver versus gold layers is apparent from the perspective views of the AFM scans of the two types of samples, as shown in Figure 2-6. The superior polishing results of gold was the reason for choosing to use gold layers for the plasmonic dimple lens despite the lower material Q factor. As for determining when to terminate the polishing step, rough polishing was used until the gold islands were exposed, as viewed through a microscope. The fine polishing was repeated until AFM scans showed the desired minimum thickness. Although this method is not necessarily optimal, since the exact stopping point cannot be determined precisely and it is labor intensive, it was sufficient for our device. A more efficient method could involve some electrical end point detection where polishing a carefully aligned wire would result in an electrical short once the endpoint was reached.

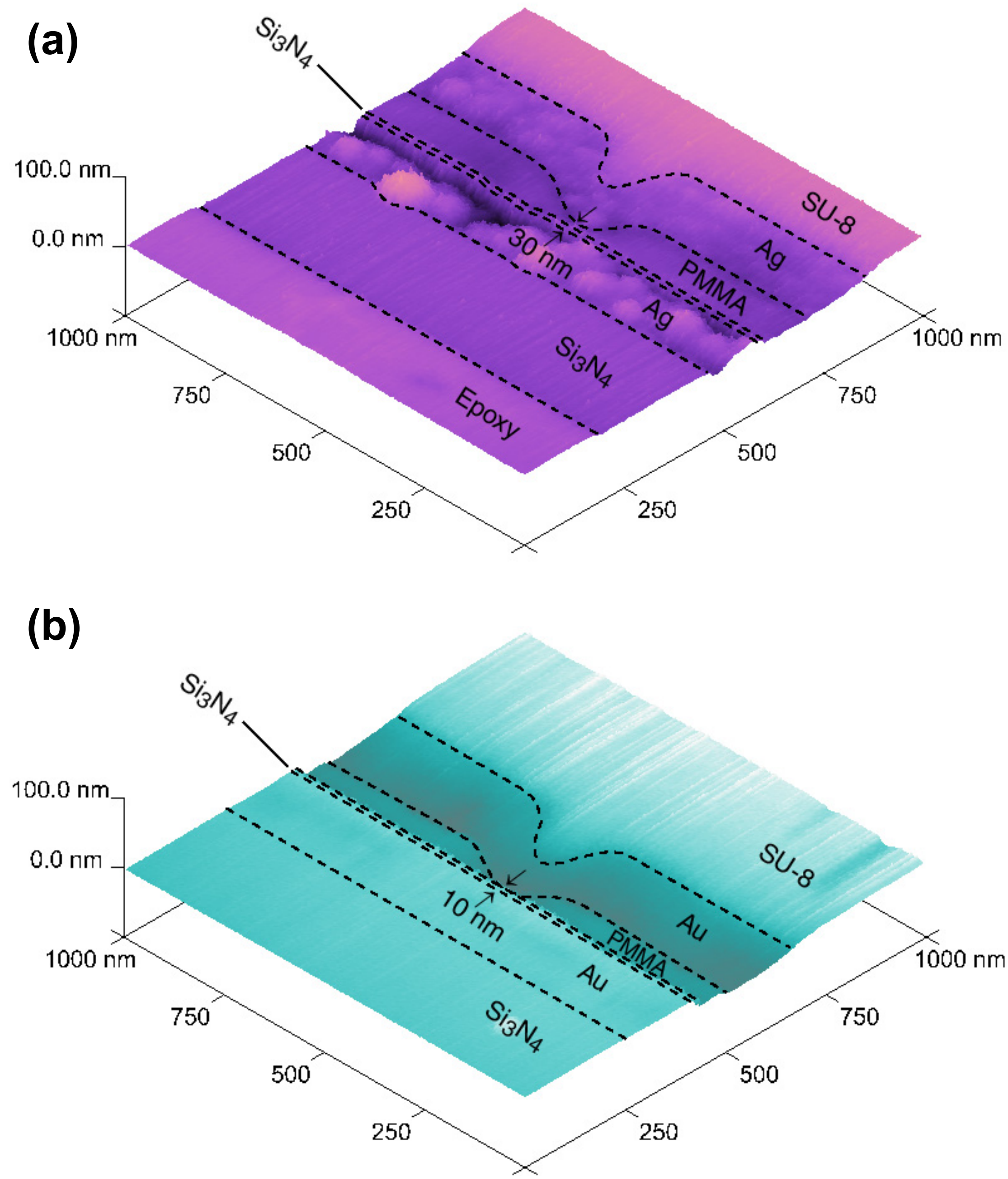

Figure 2-6. Polished facets: Ag vs Au
The out-coupling edge of the mechanical edge-polished device using (a) Ag and (b) Au as the metal layers, presented in 3D perspective view from AFM topographic scans. Roughness in the metal layers of the Ag device were overcome when these layers were switched to Au.

2.5 Bulk silicon removal

The tapered region of the plasmonic dimple lens was originally designed assuming perfectly smooth interfaces between the dielectric layer and the two metal layers [55]. This design accounted for the losses in the metal due to resistance for propagation over long distances. The resistive loss was optimized by trading off against the reflection losses from rapid tapering of the dielectric layer thickness, which can be viewed as analogous to reflection due to a mismatch in impedance along a transmission line. However, the presence of roughness in the two metal–dielectric boundaries would introduce additional scattering losses into the structure. Thus, we decided to evaporate metal against smooth dielectrics for both metal layers in order to ensure smooth interfaces and avoid these scattering losses. In order to do this, we needed to find a way to release the dielectric and first metal layer from the substrate prior to evaporating the second metal layer.

Since we were most familiar with silicon-based systems, we started with a plain silicon substrate. For the thin dielectric layer that determines the critical dimension separating the metal layers at the output, we considered two materials that could be deposited/grown on silicon: silicon nitride and silicon dioxide. The film needed to have a good etch selectivity relative to the silicon substrate to survive being etched, since the thin silicon wafers we used were ~300 μm thick, compared to a < 10 nm target thickness for the dielectric layer. For most silicon etching methods, silicon nitride has slower etch rates than silicon dioxide [75, 76], and thus silicon nitride has superior selectivity compared to silicon dioxide. Additionally, after removal of the silicon, the thin dielectric would either be a free-hanging membrane or it would have to be first bonded to another substrate using epoxy. Either way, the thin dielectric layer must also be strong, in order to support its own weight or withstand the stress of the epoxy. Thus, of the two, nitride was chosen for its superior strength and higher resistance to silicon etchants.

Next, given that we had decided to use a silicon nitride thin film on a silicon substrate, we had to choose whether to use a free-standing film or to support it before etching the silicon. We would then also need to find an etching method compatible with all of these materials. Since there is always some etching of the thin nitride layer, even with the best selectivity between silicon and nitride during etches, we could not leave the thin nitride layer exposed during the etching of the whole 300 μm substrate. Furthermore in order to have multiple devices on a single sample, it would be necessary to remove a majority of the substrate. Since we would eventually have to bond the structure to another piece of glass for the mechanical edge-polishing step anyhow, we decided to bond the sample prior to removing the substrate, in order to provide support for the thin film.

Since we would be using an epoxy to bond the sample to a piece of glass prior to bulk silicon removal, the thin nitride film would have to withstand the stress of the cured epoxy after being released from the silicon substrate. We tried several epoxies for this: two optically transparent epoxies (Norland 61, Norland 81) and one low stress silica-filled epoxy (Optocast 3408). We tested the stress on 100 μm square windows of a thick (initially ~800 nm) nitride film, which were exposed via KOH etching from the backside, by curing the different epoxies in the pyramidal pits. The deflection of the film was measured on the smooth side using a Veeco Dektak 6 profiler and a Veeco Wyko NT3300 Optical 3D Profiling System. Norland 61 and Norland 81 had 2.5 μm and 1.5 μm maximum deflections, respectively. An example of a Wyko scan of one of these nitride windows for a different type of epoxy, Norland 74, is shown in Figure 2-7. In contrast, the Optocast only had 100 nm of deflection, which was similar to that of a control sample without epoxy. Furthermore, during various wet etch tests, the two Norland epoxies were also slowly eroded, allowing the layers to peel apart. In contrast, after the epoxy was eroded for Optocast, the silica spheres remained behind and seemed to prevent further penetration of the etchant, possibly similar to sandbags. An example of this Optocast silica border can be seen in Section 2.5.2.

For large area silicon substrate removal, we also attempted to protect the edge of our sample using a black wax (Apiezon Wax W). However, elevated temperatures softened the wax during the wet etches, and the wax was not suitable for dry etches since any moisture could lead to the formation of HF. Fortunately, the self-limiting nature of etched Optocast epoxy seemed to be the best way to protect the edges of our samples. Thus we decided to use Optocast as the epoxy for this bonding step, which necessitated that we fabricate the lower side of the device first (as shown in Figure 2-3), since optical access is required for the top side which has the grating coupler.

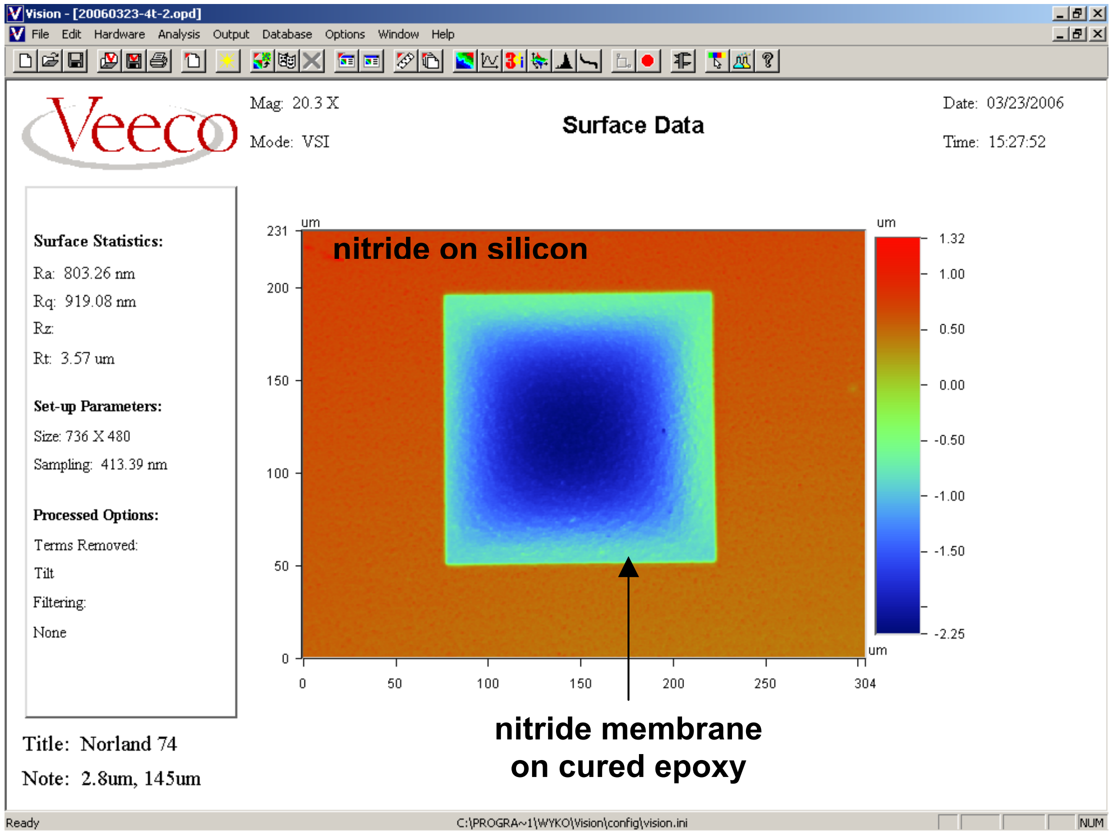

Figure 2-7. Nitride film deflection due to epoxy
A Wyko optical profiler image of a silicon nitride window that has been exposed via KOH etching. Epoxy has been cured inside the pyramidal KOH pit, and the deflection of the membrane demonstrates the stress of the epoxy on the film. The deflection is confirmed by Dektak measurements, but there is no discontinuity at the edge of the window, as implied by the Wyko scan. The discontinuity in the Wyko scan is due to the different materials below the nitride in these two regions.

However, despite the low stress levels of the Optocast, the thin 10 nm nitride film still cracked when larger areas of silicon were removed. So, we deposited a 300 nm layer of PECVD silicon nitride on top of the thin nitride after the first metal deposition of the gold islands, to help provide strength to the film and limit the stress on the thin nitride layer. Even with the thicker PECVD nitride layer, it was important to remove any bubbles in the Optocast during the bonding step, since this could lead to shattered films, as shown in Figure 2-8. The thicker nitride also caused stress on the gold islands, which led to bubbling in some of the larger gold islands due to poor adhesion and possible contamination, as can be seen in Figure 2-9. Since the thick PECVD silicon nitride was a less stoichiometric film than the thin LPCVD nitride film, it was also more susceptible to being etched by silicon etchants. So, any pinholes or damage in the thin nitride film could lead to significant damage of the underlying thick nitride film during the silicon etch process as can be seen in Figure 2-10.

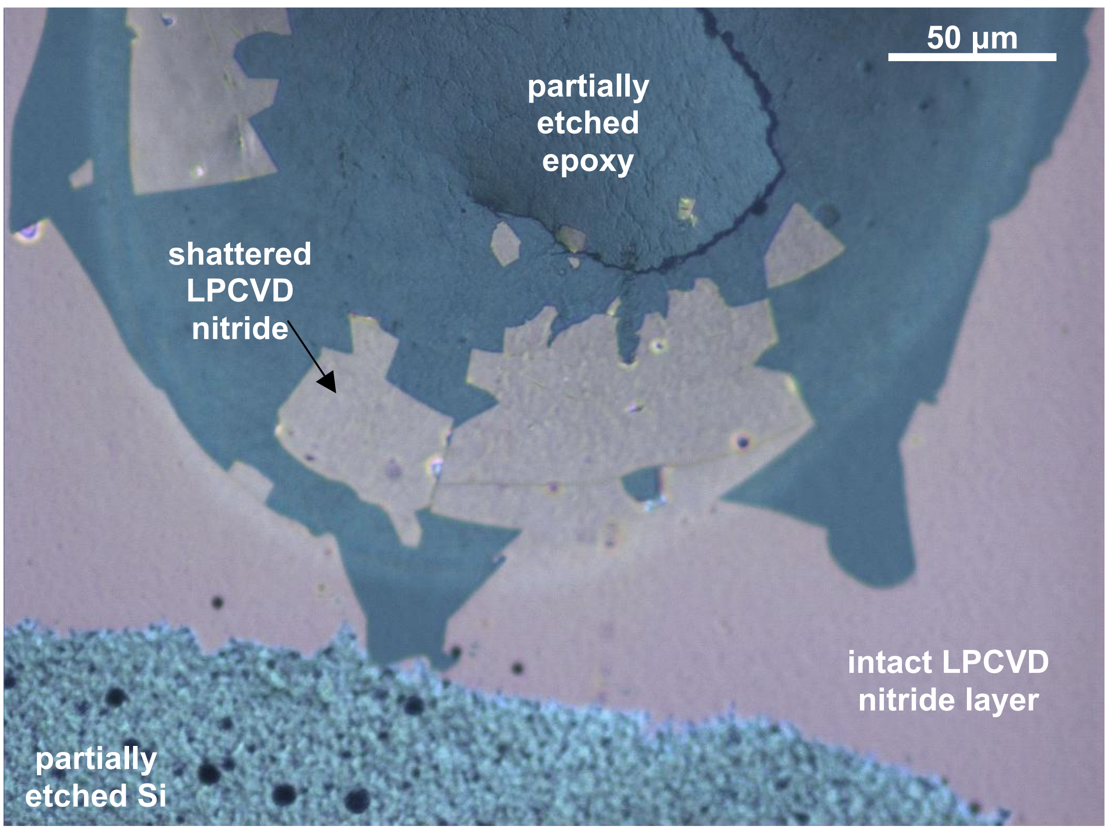

Figure 2-8. Nitride shattered during wet etch
Wet etch sample with damage to the thin LPCVD silicon nitride layer after removal of the silicon substrate, as viewed through an optical microscope. Stress from the underlying epoxy layer has shattered the nitride layer.

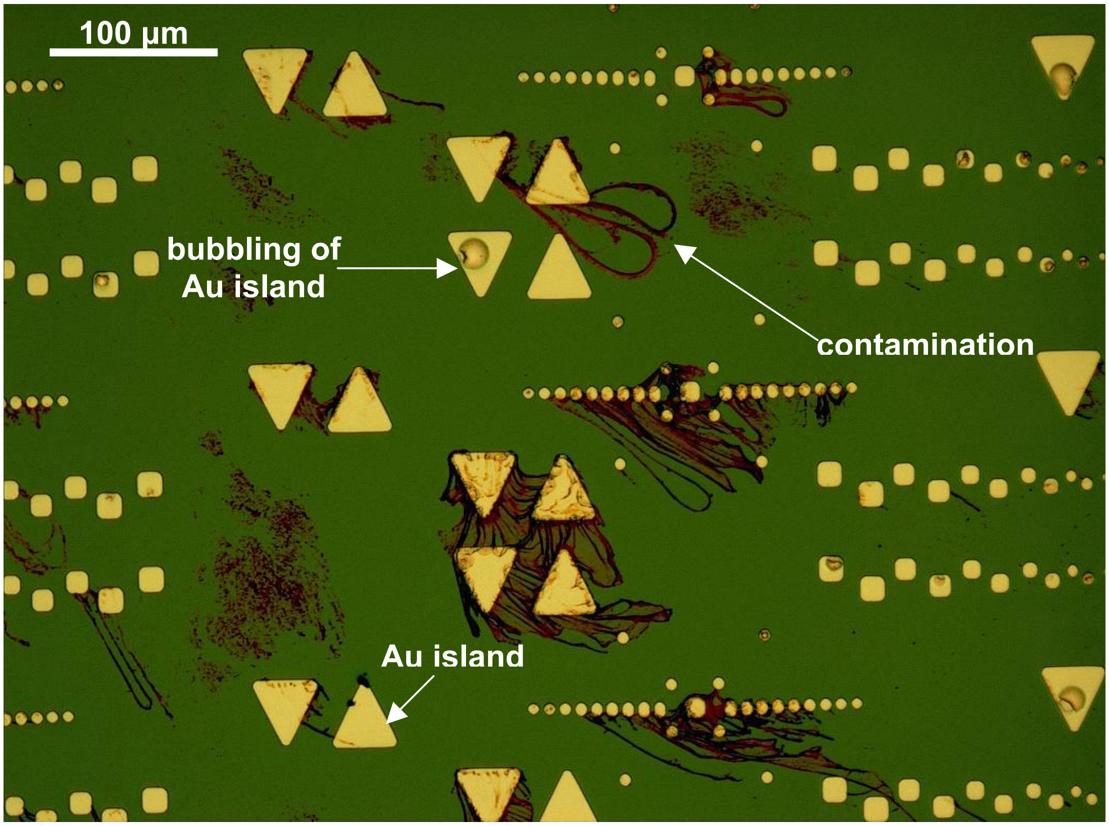

Figure 2-9. Bubbling in Au islands
Sample with bubbling in Au islands after deposition of thick PECVD silicon nitride layer to protect and support the thin LPCVD nitride layer, as viewed through an optical microscope. Stress from the deposited nitride and contamination on the sample lead to separation of Au from the nitride due to poor adhesion. Bubbling of the Au islands can be found even without the visible contamination featured in this image.

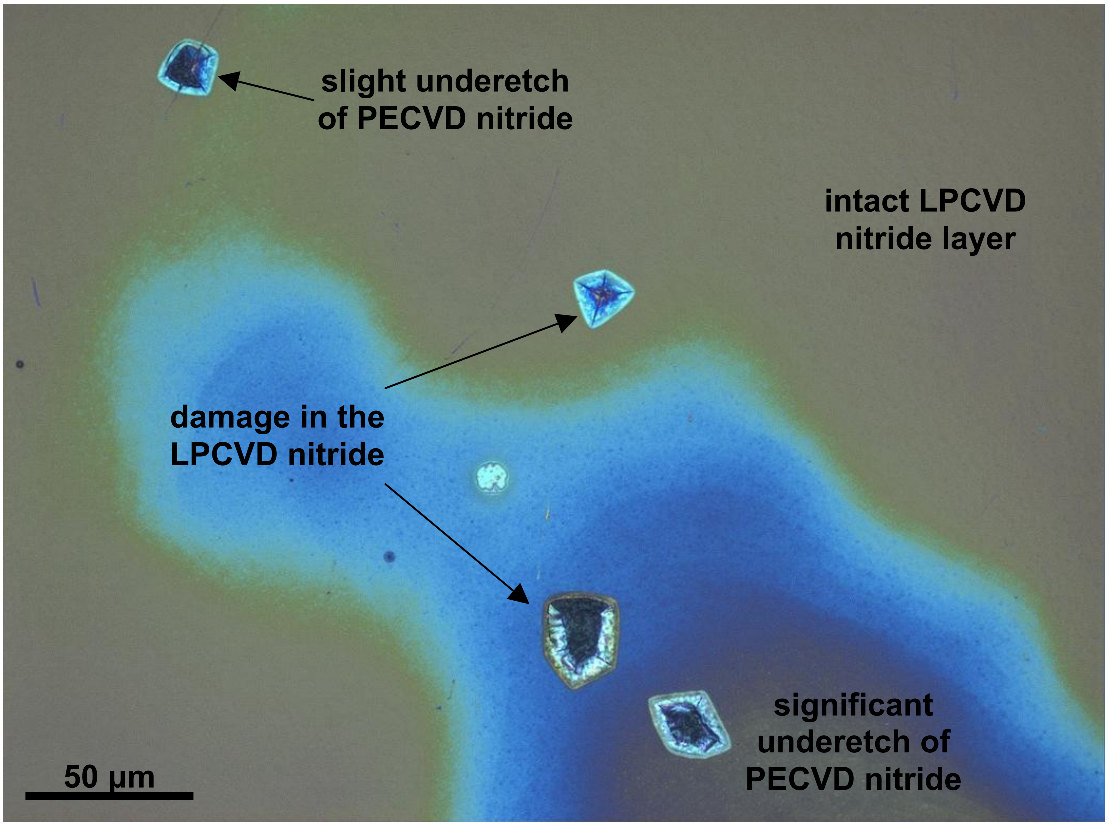

Figure 2-10. Pinholes in nitride
Wet etch sample with pinhole or damage in the thin LPCVD silicon nitride layer leading to significant damage to the underlying PECVD silicon nitride layer after silicon removal, as viewed through an optical microscope. The PECVD nitride layer is less stoichiometric and thus more susceptible to etching. Even a small area of damaged LPCVD can lead to large areas of underetching of the PECVD nitride during prolonged wet etches.

We tested four different methods of etching silicon: two wet etches and two dry etches [75, 76]. The two wet etches were the anisotropic heated potassium hydroxide (KOH) etch and the isotropic HNA etch, composed of hydrofluoric acid (HF) + nitric acid (HNO_3) + acetic acid ($HC_2H_3O_2$). The two dry etches we tested were the isotropic xenon difluoride (XeF_2) gas etch and the anisotropic deep reactive ion etching (DRIE) method.

2.5.1 Bulk silicon removal – KOH

The first method we attempted for the silicon removal was using a heated KOH solution. However, large area heated KOH wet etching of silicon was not feasible for several reason. One major reason was that any slight nonuniformity was amplified during this anisotropic etch, resulting in a random pattern of pyramidal pits. Figure 2-11 shows an example of one of the pyramidal pits that resulted from broad area etching of a silicon nitride coated silicon wafer from the backside. The wafer was patterned with silver islands on top of the silicon nitride on the topside prior to the etch, so that the islands could serve as an endpoint test. Further etching in KOH etches the silicon very slowly along the pyramidal pit faces. During this time, the thin LPCVD nitride can be etched away to expose the silver islands, as evidenced by the missing silver islands. Furthermore, most of the epoxies failed during the heated KOH etch, allowing the silicon to peel apart from the glass substrate. We could not prevent this from happening by protecting the edges with the Apiezon wax since the wax also separated during the heated KOH etch. Lastly, even with a KOH solution heated to ~80 ºC, the etching of the whole substrate still took ~5-6 hours due to the thickness of the silicon wafer.

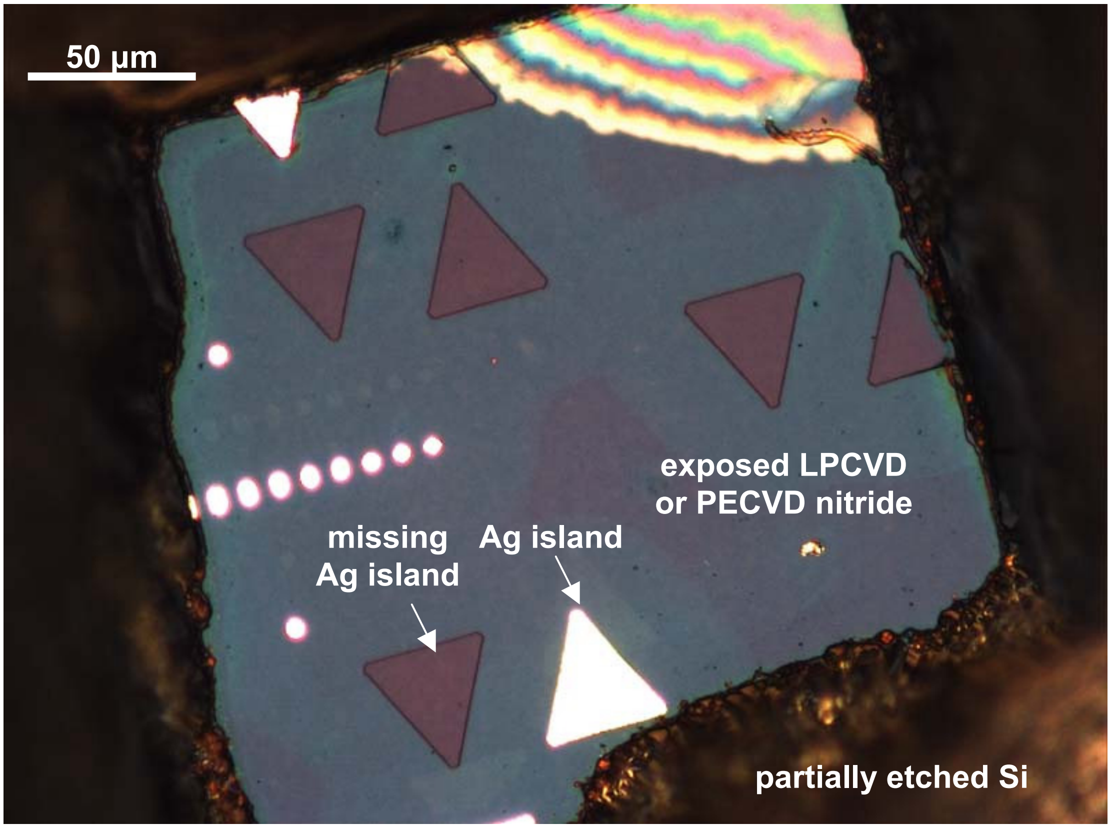

Figure 2-11. KOH etching of Si
Silicon sample etched with KOH over a broad area, as viewed through an optical microscope. Such etching results in a random assortment of pyramidal pits, where further etching of the silicon is slow and leaves the nitride layer exposed for a prolonged period of time. The <10 nm layer of LPCVD nitride can be etched away, exposing the Ag islands to be etched away as well.

2.5.2 Bulk silicon removal – HNA

In contrast to the heated KOH etchant, the isotropic HNA wet etch was a much quicker method of etching which allowed easier testing. Etch rates for this etch system can be found from the triaxial isoetch curves shown in reference [77]. The primary etching chemicals in these mixtures are the HF and the HNO_3, with acetic acid or water acting as a diluent to control the etch rate [78]. After testing various mixtures of the HNA etch, the diluent did not seem to improve the quality of the etch significantly for our bulk removal purposes, but rather only lengthened the time of etch. Even at the fastest etch rates with no diluent, the thin LPCVD silicon nitride was able to withstand the small over-etch time required to ensure removal of the majority of the silicon. Thus, in order to maintain fairly quick etches (< 1 minute per sample), we decided to dispense with the diluent and use only a mixture of HF and HNO_3.

The ratio of HF to HNO_3 was also varied to test its effect on the etching quality [79]. By varying the relative concentrations of HF and HNO_3, sometimes the silicon etched from outside inwards, and other times it etched from inside outwards. We preferred to etch from inside outwards since we wanted a broad area of exposed nitride, and we could tolerate having some silicon rim remaining, in order to minimize the nitride's time of exposure to the etchant. Having a silicon rim also helped to prevent the edges of the nitride from getting eroded. Another result of testing the concentrations was that varying the ratio away from equal parts of HF and HNO_3 also decreased the etch rate. For some concentrations, the etch process even stopped itself before the silicon was etched through to expose any of the nitride. Thus, we settled on a HNA mixture with equal parts of 49% HF and 70% HNO_3 without any diluent, using ~200 mL of the mixture to etch each 15 mm x 15 mm sample piece.

An example of the different stages of HNA etching of an un-patterned piece of silicon wafer coated with nitride, where the etching goes from the center outwards, can be seen in Figure 2-12. The sample must be etched for a sufficiently long enough time to remove a majority of the silicon rim (in this case, ~30-40 seconds), but not too long so as to avoid damage to the nitride. An additional exposure of 5-10 seconds after most of the silicon has been removed is often enough to damage the thin LPCVD nitride, after which the thick PECVD nitride is quickly etched to leave behind only the epoxy underneath, as can be seen in Figure 2-13a. Note that the samples shown in Figure 2-12 were not patterned, and thus the nitride had less damage than patterned samples. It was difficult to completely remove the silicon rim on a patterned sample because there was usually too much damage to the thin silicon nitride due to the extra processing steps. Thus it is critical to constantly monitor the etch process and remove the sample from the etchant promptly after a suitably large enough clear window has been opened up in the silicon.

Constant agitation during the etch process is also helpful to maintain uniformity of the silicon removal, since the etching also produces many bubbles. Uniform etching is necessary to prevent isolated silicon mounds from remaining behind as can be seen in Figure 2-13b, and also to minimize the etching time difference for removing most of the silicon rim. It is important to remove these silicon mounds to have a broad flat area in which to bond the second glass piece in the final step before edge-polishing. Tilting the sample was also undesirable as it could sometimes lead to etching from one side to the other. Also note the Optocast silica rim that remained after etching in the samples of Figure 2-12, which helped to limit the undercutting of the PECVD nitride and prevented separation of the sample from the glass substrate, as discussed previously.

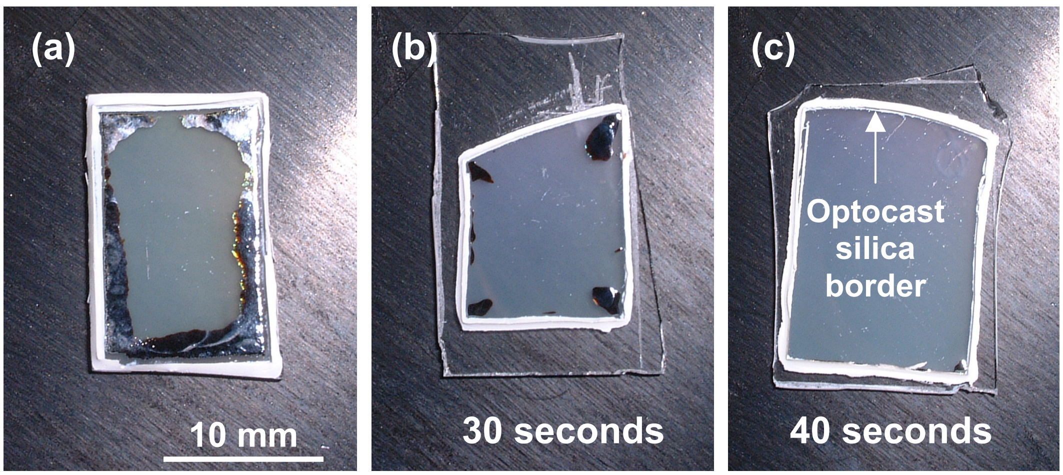

Figure 2-12. HNA etching: Si rim
Silicon sample pieces that have been bonded to glass using Optocast epoxy and etched using varying concentrations and for varying times with HNA isotropic wet etch. The photographs of these samples illustrate the typical progression of the HNA etching process. The concentrations are chosen so that the sample etches from inside outwards. a) For some HNA formulations, a silicon rim will remain for a prolonged period. b) Most of the silicon has been removed on a sample that has been etched for 30 seconds using the final HNA formulation. c) Silicon has been completely removed from a sample that has been etched for 40 seconds using the final HNA formulation. As a reference, the amount of silicon remaining in image a) would typically be after ~20-25 seconds using the same HNA formulation. Etch times also vary depending on sizes of the samples, agitation, and etching of multiple pieces in the same solution. Also note that the silica border that remains from the Optocast epoxy, which helps to protect the edges of the sample.

One final problem we encountered during HNA etching was due to the need for larger samples. For the e-beam patterning and also for the final edge-polishing step, the open area of the sample needed to have at least a 10 mm x 10 mm area.

Since the HNA etch had to be terminated on patterned samples when there was still ~2-3 mm of silicon rim remaining in order to prevent damage to the nitride, we had to switch to larger samples, ~15-20 mm on each side. However, having larger samples also led to increased heating of the etchant solution during the etching process. As can be seen from reference [80], the etch rate of silicon in HNA etch typically doubles for every 10ºC.

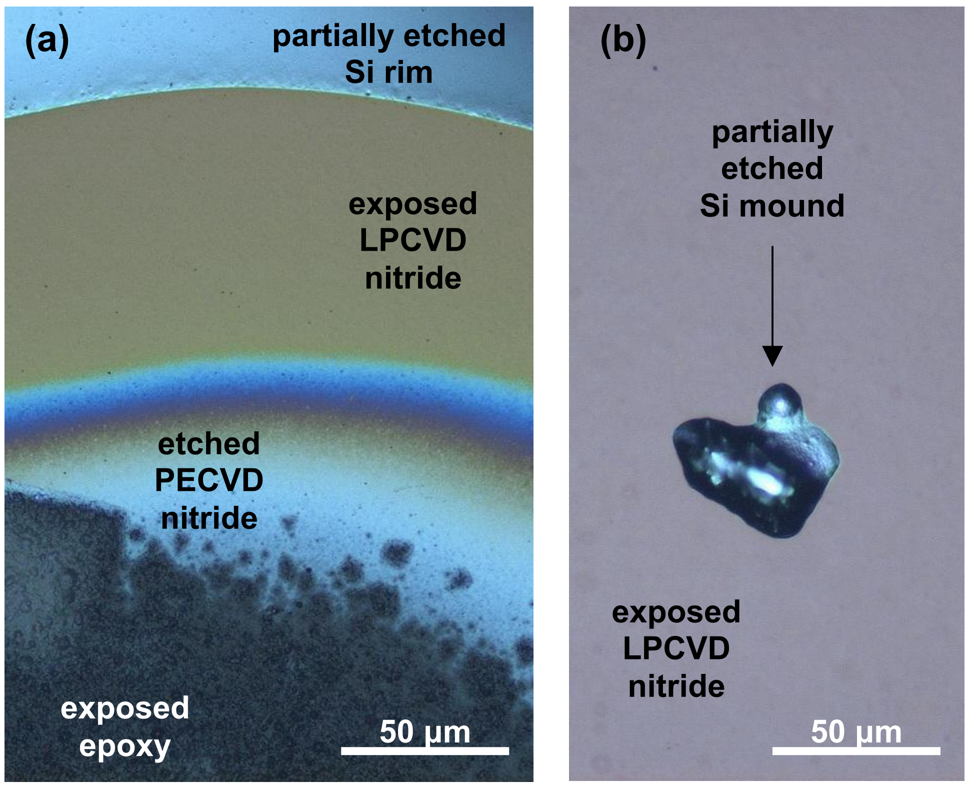

Figure 2-13. HNA etching: problems
Examples of problems encountered during HNA etching, as viewed through an optical microscope. a) Sample that has been over-etched in HNA, resulting in damage to the underlying PECVD nitride. The PECVD nitride is quickly etched to expose the epoxy layer over much of the sample, even before the silicon is completely removed. b) Non-uniform etching can result in Si mounds that must be removed to ensure that the thin nitride is completely exposed over a broad area of the sample. Prolonged etching to remove these Si mounds has the potential to damage the thin nitride.

Since the etching speed increases as the etch progresses due to increasing temperature, an even greater temperature increase for larger samples made it more difficult to accurately stop the etch process on time. Thus, we decided we would need to thin the sample's silicon substrate down before the HNA etch, to limit the temperature increase on these larger samples. To do this, we decided to use a dry etch method rather than polishing since HNA etch is an isotropic etch and is less sensitive to the roughness of the beginning surface. Since the HNA etch has the best selectivity against nitride for the methods we tried, we ended up using a two-step bulk silicon removal process, with a dry etch as the first step to thin down the substrate and the HNA etch as the second step to limit damage to the thin nitride layer. The choice of the dry etching method will be discussed in the next two sections.

2.5.3 Bulk silicon removal – XeF_2

The first dry etch method we tested was a XeF_2 vapor etching system which was custom built by the UCLA Nanolab. This method etches silicon isotropically, but it also etches nitride slightly, at around 10 nm/min [76]. This etch may have been better suited for a device with silicon dioxide as the thin dielectric instead of nitride, since it etches oxide more slowly. However, even when we tested the etching with oxide, it was difficult to ensure that there was no moisture in the chamber because of the use of epoxy. Any moisture would create HF that etches the oxide.

This isotropic dry etch also created a curved surface on the silicon substrate after etching, which ultimately etched the silicon from the outside inwards. Attempts to protect the edges of the sample with the Apiezon wax to prevent this curvature were unsuccessful, since the wax reacted with the gas and possibly also had moisture. The curvature in the silicon caused the edges of the nitride layer to be exposed to the etching vapors for an extended period of time while the remainder of the silicon in the center was being etched.

Since the etching of the bulk silicon takes ~2-3 hours in XeF_2, this etch method did not have enough selectivity to completely etch the silicon without damaging the nitride. An example of a sample etched in XeF_2 is shown in Figure 2-14. The curved silicon is visible at the center, and concentric rings of color variation in the exposed nitride indicate that the nitride has been etched as well. Since XeF_2 is a relatively slow etching method that leads to significant curvature in the sample, it is not a good method for thinning down the silicon thickness prior to switching to the HNA etch. Thus, we decided against using the XeF_2 etch in our bulk silicon removal process.

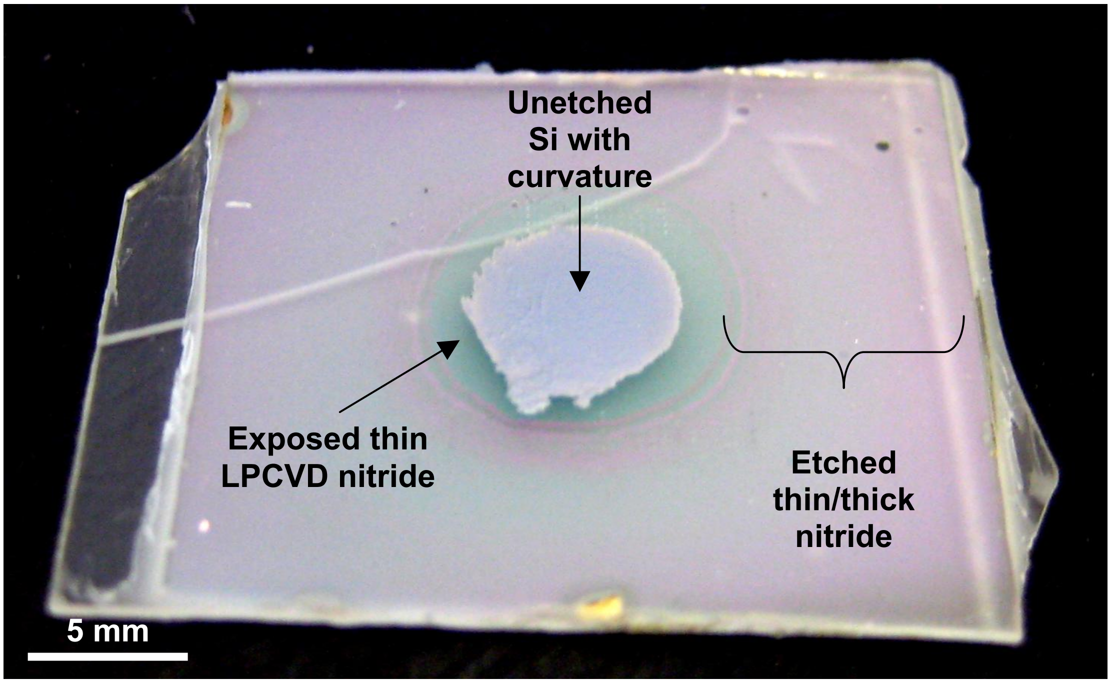

Figure 2-14. XeF_2 etching of Si
Photograph of a sample etched in XeF_2 dry etch. Sample etches from the outside inwards, with a curved silicon island remaining at the center. As the island shrinks, the exposed nitride is etched, as can be seen from the concentric rings of color variation.

2.5.4 Bulk silicon removal – DRIE

The final etch method we tested was deep reactive ion etching, which is an anisotropic dry etch. The machine used was a Unaxis Versaline Fast DRIE system. Since we were not concerned with sidewall smoothness we used the fastest etch recipe available, which etched at a nominal rate of 10 μm/min. The etch recipe consisted of flow rates of 20 sccm CF_4, 20 sccm C_4F_8, and 4 sccm O_2 at a pressure of 4 MTorr, with RIE power of 200 W and ICP (inductively coupled plasma) power of 1250 W. This method also did not have enough selectivity to completely etch the silicon substrate without damaging the thin nitride.

However, the Optocast border seemed to act as a mask during the anisotropic etch to protect the edge of the silicon sample. Thus, the DRIE was able to uniformly thin down the silicon substrate (as compared to the curved XeF_2 etching), and it was able do so without too much roughness (as compared to the pyramidal pits of KOH etching). Furthermore, we could quickly remove most of the substrate in ~30 min. So, we decided to choose DRIE as our method for thinning down the silicon substrate prior to using the final HNA etch. After the DRIE etch, the sample also remains coated by a polymer residue, but this residue was easily removed by the subsequent HNA etch.

2.6 Measurement and analysis

Unfortunately, the experimental efficiency of the plasmonic dimple lens device is difficult to measure in the far-field, since this device, like the NSOM, is a small structure that radiates poorly into the far-field [24], as will be discussed further in Chapter 3. Furthermore, the dimple lens is not a darkfield device; much of the input light is scattered to the output and would be collected in the far-field as well. Thus, we chose to use a near-field measurement method for the plasmonic dimple lens. Additionally, due to sample variability and the difficulty of comparing the power measured in the near-field with the power input to the grating coupler, we chose to measure the spot size of the dimple lens device compared to the spot size of a control sample with just a grating coupler and no dimple lens.

The fabricated plasmonic dimple lens was characterized using a modified Veeco Aurora-3 NSOM system. The characterization setup and measurement results are also described in [56, 57]. A schematic of this NSOM measurement setup is shown in Figure 2-15. The sample was mounted vertically on the NSOM stage so that the polished out-coupling facet of the device points upwards. 633 nm wavelength laser light from a HeNe laser was focused from the side onto the grating region of the device using a microscope objective (0.45 NA, 50x). The out-coupled light from the device was collected with a photo-multiplier tube (PMT) through a commercially available pulled-fiber NSOM probe. The grating coupler was estimated to have an in-coupling efficiency of approximately 7-10%.

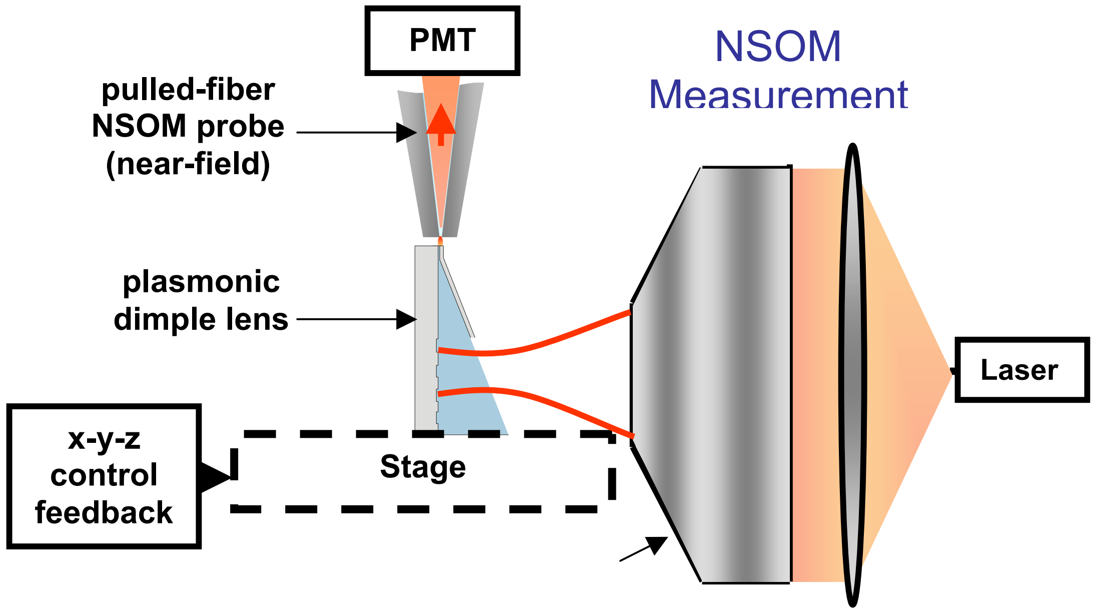

Figure 2-15. NSOM characterization setup
Schematic of the experimental setup to characterize the plasmonic dimple lens using the NSOM technique.

The sample was scanned using the NSOM tip to acquire both the topographic and optical images simultaneously, as shown in Figure 2-16. Figure 2-16a,b show good correlation between the region of high intensity light in the optical image and the dimple region of the device in the topographic scan. Furthermore, the spot size of the optical image for the dimple structure in Figure 2-16b is approximately 180 nm x 225 nm, which is believed to be limited by the size of the pulled-fiber probe aperture (~150 nm aperture size) used in the NSOM measurement system. This can be compared to the larger spot (approximately 240 nm x 465 nm) that we obtained for a device with just the circular grating alone (i.e. without a dimple lens), as shown in Figure 2-16d. The spot size in the vertical direction for the grating alone case matches the diffraction limited spot size for 633 nm wavelength light in a medium with refractive index 1.5, which is about 210 nm. Also, notice that even for the dimple lens sample, the spot is slightly larger in the horizontal direction than the vertical direction (perpendicular to the stack of layers). This reflects the fact that there is less metal blocking the light in those regions, so extra light can leak out.

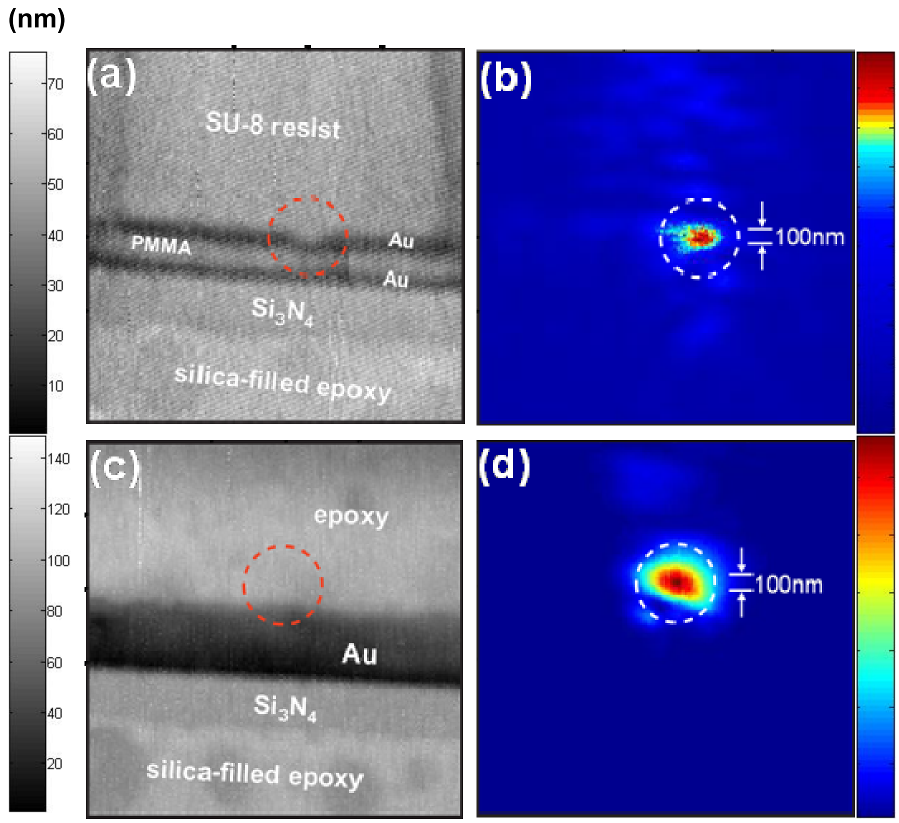

Figure 2-16. NSOM scan of dimple lens output
(a) Topographic and (b) optical images of the out-coupling facet of the plasmonic dimple lens obtained using the NSOM technique. (c) Topographic and (d) optical images of the polishing facet of the circular grating coupler only (without a plasmonic dimple lens). All the scans are 2.5 µm x 2.5 µm.

However, the optical image of the dimple structure presented in Figure 2-16b is actually an average result of four different NSOM scans of the same device. The average was taken in order to suppress the background light away from the dimple region of the device. This background light is due to interference patterns in the upper transparent SU-8 layer, as well as from other sources of scattered light that are able to escape out the polished facet through the various transparent dielectric layers. Since these patterns vary with the position of the input laser light, averaging helped to reduce the level of this background noise.

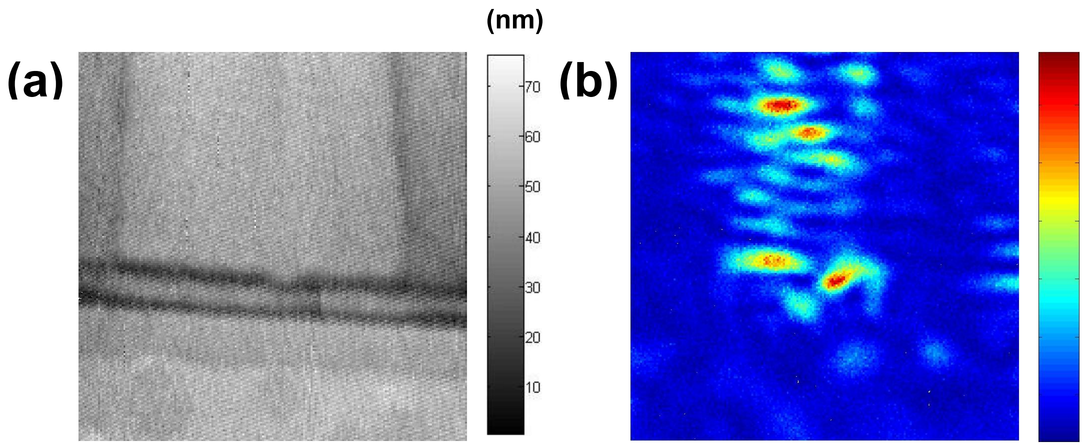

Figure 2-17. NSOM scan of dimple lens output (single scan)

(a) Topographic and (b) optical images of the out-coupling facet of the plasmonic dimple lens obtained using the NSOM technique for a single scan (no averaging). Both images are 3.0 μm x 3.0 μm.

Furthermore, the color bar in Figure 2-16b was shifted relative to the standard color bar shown in Figure 2-16d in order to simulate the effect of having a threshold dependent measuring scheme, which further suppresses the background noise. As a comparison, an example of the unmodified optical data from a single scan can be seen in Figure 2-17b, where the background level can be as high as that of the focal point. However, since the NSOM aperture effectively sums the output light over a ~150 nm diameter area, it is still possible that the focused light from the dimple lens could actually have a much higher intensity over a smaller area than any of the background light. Nevertheless, the presence of the background light in these images helps to underscore the need for a darkfield device in more sensitive applications, which is the topic of Chapter 3.

2.7 Conclusion

Since we only have measurements of the spot sizes for a couple of dimple lens devices, and these measured sizes are strongly dependent on the size and quality of the NSOM probe used, we cannot be absolutely certain that these results are statistically significant. However, these results were fairly reproducible over several scans of the same device. Furthermore, since the dimple lens output spot size seems to match that expected from the size of the NSOM probes, and the grating alone sample result matches the expected diffraction limited size, we are fairly confident these results are not merely a function of differing NSOM probes used.

Although these results support our expectation that the dimple lens will be able to focus to a spot size smaller than the diffraction limit, our measurement was limited by the aperture size of the pulled-fiber NSOM probe that was used, which effectively sums the light over an area equal to the size of the probe's aperture. Thus, a higher resolution method for imaging the out-coupling facet of our device would be necessary to determine the true spot size of the dimple lens. For example, a measurement using apertureless NSOM would have resolution that is limited by the size of the very end of the AFM tip, which has been shown to provide resolution down to 10 nm [81, 82, 83].

Another method would be to place photoresist or some of other light sensitive material at the output of the dimple lens to try to expose the resist and measure the size of the exposed resist. However, this method has potential difficulties due to material incompatibility, such as the resist solvents interacting with the polymer layers, as well as the uncertainty that the device topography may not have changed due to other reasons (e.g. liquid absorption, thermal swelling, mechanical/chemical damage). Similarly, using the dimple lens to expose resist on a substrate could also be difficult, since it would be difficult to avoid contacting the substrate, unless it can be integrated with an NSOM system with feedback, or by using hard drive flying head technology like that discussed in reference [16].

Thus, although it could be possible to more accurately measure the optical spot size at the output of our device with one of these alternative measurement methods, we felt that the above measurements were sufficient for showing that the device at least focuses beyond a diffraction limited spot size. Since this device has significant levels of background noise, as can be observed from the NSOM scan in Figure 2-17b, the plasmonic dimple lens has limited applications. For applications that have a threshold mechanism, the spot size can be adjusted by varying the power level. Thus, we did not pursue further attempts to characterize the ultimate resolution of this device, and instead turned to making a darkfield version of this device.

Chapter 3 – Darkfield Plasmonic Lens

3.1 Motivation

The NSOM measurement results described in Section 2.6 reinforce our expectation that the plasmonic dimple lens is not a darkfield device. The presence of background light at the out-coupling facet can be seen in Figure 2-16b,d. Although the light at the focus of our device is more confined in the vertical direction (perpendicular to the stack of layers) than is possible in free space, the horizontal size of the spot of light in Figure 2-16b is still fairly large. We believe this is due to stray light, for example light from the grating that doesn't intersect the 100 nm wide dimple region.

Also, there is additional scattered background light outside of the gold–dielectric–gold area, which is represented by the faint blue spots located several hundred nanometers away from the main red spot of each image. We believe that some of this light is scattered background light and some are standing wave patterns due to reflections from the metal and at the boundaries between transparent layers. This light is coupled out of the end facet and collected by the NSOM measurement system due to the proximity of the input light beam and the presence of transparent dielectric layers in the device. This background light is also more clearly visible in the single scan image of Figure 2-17b.

Applications such as HAMR, which have a threshold for change due to optical energy, may have an inherent tolerance to this background light. However, other applications such as NSOM are more sensitive to background levels of light. In order to do a sensitive near-field optical measurement for NSOM, it is necessary to eliminate any stray light outside the area of interest. Similar ideas regarding a darkfield measurement method for NSOM are presented in reference [84]. Thus, a new goal of this work has been to create a darkfield version of the plasmonic dimple lens with a potential application as an NSOM probe.

3.2 Background

The standard probe used in NSOM systems is a metalized pulled-fiber probe, which can have very low throughputs [65]. These fibers are coated in metal, which is a key factor for confining light due to the low penetration of light into metal as discussed in Chapter 1. This confinement allows these probes to obtain a small spot size and to have a darkfield measurement method. However, the metal coating also is an important factor to the low throughput of these fibers. These fibers typically have a small taper angle, as small as 1-2º in reference [65], which leads to significant propagation losses down the metalized taper. Since these fibers are coated in metal, they have a wavelength-dependent cutoff size after which the power decays exponentially in the length of the fiber [49]. This limits the size of the aperture you can make for pulled-fiber probes to ~100 nm due to these losses.

As was discussed in the previous chapter for the dimple lens, one can optimize the taper angle to trade off between the propagation and reflection losses, where the optimal taper angle for planar structures was found to be ~30º [55]. For cylindrically symmetric tapered structures, the optimal taper angle also seems to be in this range of ~30º, based on the results typically found for more advanced NSOM probes. Some examples of these more advanced types of NSOM probes from the literature include etched fiber probes [85, 86, 87], pyramidal apertures [88], and cantilever-based probes [89, 90]. All of these probe types have larger taper angles to limit the propagation losses by tapering quickly to the final output aperture size. The optimal angle range is also reinforced by the theoretical results in reference [91], and by the design of the darkfield plasmonic lens as will be discussed in Section 3.3.

In addition to trading off between the reflection and propagation losses in the taper, the taper angle also affects the spot size at the output of the aperture [91]. One way to understand this is to take the simple example of a plane wave incident on a planar metal film with a tapered pinhole and consider only the evanescent field that penetrates through the metal, with no losses in the tapered region or through the metal film. As a point of reference, for a metal with a skin depth of 25 nm, about 1.8% of the E field will penetrating through a 100 nm film, which corresponds to –35 dB of the input light intensity. This is why for you need to have a fairly thick metal film to block most of the light for sensitive optical measurement. Some examples of the evanescent penetration through various tapered structures in a metal film with a skin depth of 25 nm are shown in Figure 3-1. As you can see from these figures, the angle and shape of the taper greatly affects the output spot size just due to the evanescent penetration of the light through the metal.

However, in a real device, the power that makes it through the hole is further modified by the propagation losses due to material resistance and if the hole becomes smaller than the cutoff diameter of the allowed mode. If we consider the light through the hole to be the desired signal and the background evanescent light to be noise, losses through the hole decrease the signal-to-noise ratio (SNR). Since the throughput through the hole must be able to compete with the light that penetrates through any thin metal areas evanescently (i.e. have a reasonable SNR), this underscores the importance of having a thick metal film with no thin regions outside the focal area, and also a taper angle in the focal area that is not too large.

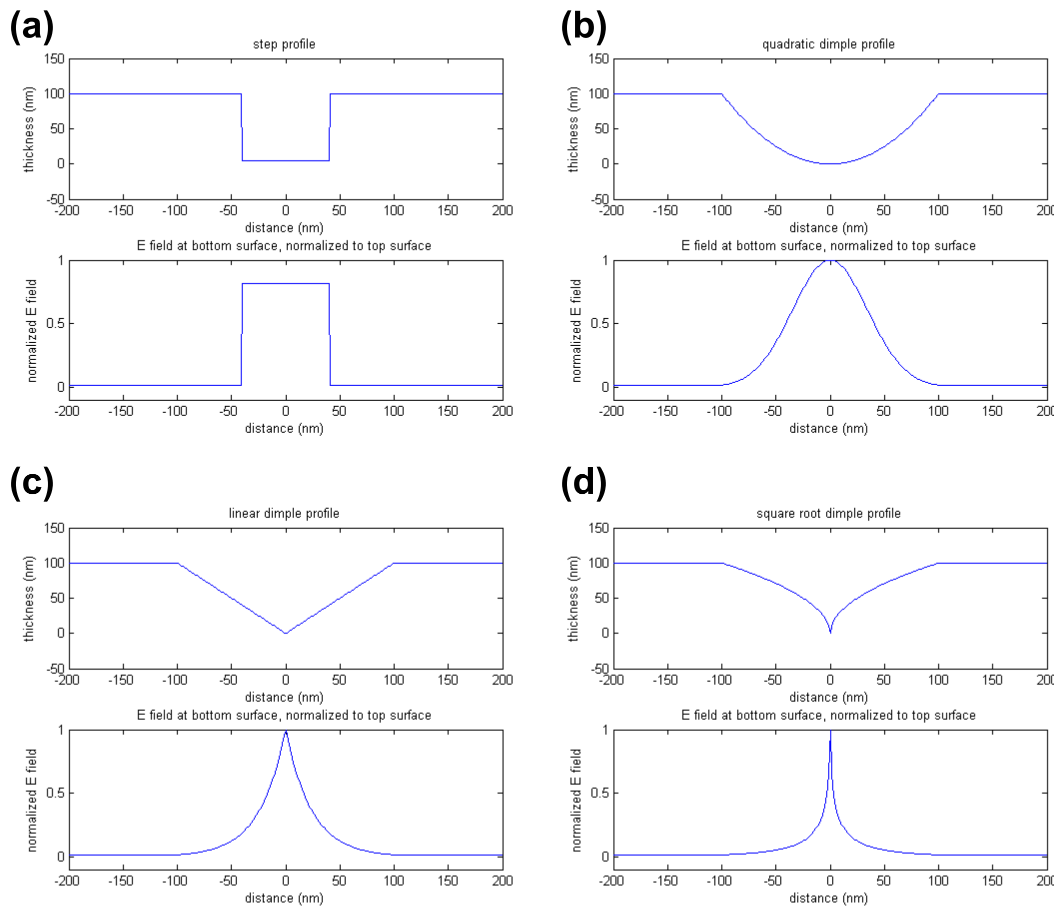

Figure 3-1. Evanescent penetration of light
Plots of the evanescent penetration of light through a 100 nm metal film with various taper shapes for the aperture: (a) a straight pinhole, (b) a quadratic taper, (c) a linear taper, and (d) a square root taper. The light is assumed to have a 25 nm penetration depth into the metal.

The resolution or spot size of a NSOM probe can also be considered to be approximately equal to the size of the aperture plus the penetration of the field into the metal surrounding the aperture, or skin depth [49]. The skin depths in Al, Ag, and Au at optical frequencies (2-3 eV energy) can vary from around 15 nm for Al to 20-30 nm for Ag to 30-50 nm for Au, based on the optical dielectric constants found in references [61, 63]. As was seen in reference [55] for the planar MIM case, the skin depth also decreases for smaller apertures in the cylindrical case, as will be discussed in Section 3.3. Thus, for a given choice of metal, the resolution of these devices is still primarily limited by the size of the aperture, making it desirable to make the final aperture size as small as possible.

Although the throughput and spot sizes of tapered structures for various angles has previously been considered analytically in reference [91], this work seeks to further the understanding for optimizing tapered structures via various methods. Analytic methods and finite element method simulations are used to compare the throughput of various structures, as will be discussed in Section 3.3. The throughput of these devices is also analyzed using circuit and antenna theory in order to understand the theoretical maximum throughput one of these devices could have, which is presented in Sections 3.5 and 3.6. In addition to the throughput, alternate figures of merit based on the ideas in reference [55] are also used to compare different types of NSOM probes in Section 3.7.

There have been several other recent examples in the literature that are also darkfield devices. For example, the C-aperture structure [36, 37] and the bullseye structure [39, 42, 43, 48] are both basically sub-wavelength holes in metal films. Similar to the other advanced NSOM probes listed above, the key feature that allows these structures to be darkfield is that they provide a clear separation between the input light and the output light via an opaque metal film, with only a sub-wavelength aperture to allow light through. This separation allows for the elimination of the background due to scattered light; however, as discussed above, light can still penetrate through evanescently in areas where the metal is thin. Thus it is necessary to have a uniform, thick metal film to block out the light.

In addition, the spot size of these aperture devices may by large since the apertures used can be as big as 250 nm, such as for the bullseye structures in reference [43]. Although the critical separation for C-aperture structures can be made smaller than 100 nm, light can still leak through the remainder of the C opening, leading to a larger area of background light in these devices as well [37]. Thus, one of the goals of this work is to improve upon these devices by having a smaller aperture, while still keeping the device darkfield.

Since the direct modification of the dimple lens into a darkfield device would present some fabrication challenges, as will be discussed in the Section 3.3.1, we have opted to instead approach this problem from the more typical starting point of the hole in metal film. The darkfield plasmonic device presented in this work can be thought of as a modification of the bullseye structure, where a taper has been incorporated into the pinhole to decrease the final output aperture size, while still limiting the additional losses. The darkfield plasmonic device is also similar in some ways to the simulated structure presented in reference [92], except thicker metal was used in this work to reduce light penetration.

One potential alternative method for darkfield focusing which does not involve the use of an aperture could be based on metamaterials. Metamaterials can have interesting properties, including a high effective refractive index, as was discussed in Chapter 2. Background information on the use of metamaterials as a lens can be found in references [93, 94], and experimental demonstrations of such lenses can be found in reference [95]. These metamaterials lenses allow for conversion of near-field light to far-field light, which is an improvement over the simpler lens ideas proposed by Pendry [96, 97]. However, since the use of metamaterials for focusing is outside the main topic of this dissertation, please refer to Appendix B for more information regarding this subject.

3.3 Darkfield plasmonic lens design

In order to create a darkfield plasmonic lens, we first sought a way to create a darkfield device based on the plasmonic dimple lens. However, since we also wanted a device that could be relatively easily fabricated, we ended up choosing to work with a tapered pinhole structure. These various ideas about ways to create a darkfield plasmonic lens will be discussed in Section 3.3.1.

In order to optimize the shape of our chosen design, we used several methods to analyze how differences in the shape and composition of the darkfield focusing structure would affect its performance. For example, to gain a better understanding of the propagation characteristics of a tapered pinhole for various hole sizes and materials, we first looked at the analytical solutions for cylindrical plasmonic modes, as presented in Section 3.3.2. Secondly, if you think of our desired tapered structure as a 'funnel', we considered the behavior of the device to be a two-step process of coupling light into the funnel and then propagating the light down the funnel. By using FEM simulations, we were able to look at the effects of taper shape on device performance, which is discussed in Section 3.3.3.

The throughput and loss characteristics of the darkfield plasmonic device were also further analyzed via circuit and antenna theory after the device was fabricated and measured. Since they did not directly relate to our choice of shape for the darkfield plasmonic lens structure, these analyses are discussed later in this chapter, in Sections 3.5 and 3.6. Other performance metrics besides throughput are also considered in Section 3.7.

3.3.1 Design – Fabrication considerations

Since our original intent was to modify the plasmonic dimple lens to make it darkfield, we had several ideas based on the dimple lens for creating a darkfield structure. The first of these methods was to alter the edge-polished dimple structure presented in Chapter 2 by adding more metal near the center of the dimple region so that, after polishing, most of the output facet would be obscured by metal. The addition of the metal bars shown in Figure 3-2a would result in an aperture resembling a C-aperture after polishing, as depicted in Figure 3-2b. This C-aperture would differ from the standard C-aperture in that it would be fed by a tapered MIM waveguide. However, the additional metal needed for this modified structure would be difficult to incorporate and align with the tapered e-beam resist of the dimple region. Furthermore, this method does not eliminate the background light due to the proximity of the input light source and the clear SU-8 and epoxy layers above the top metal of the dimple lens.

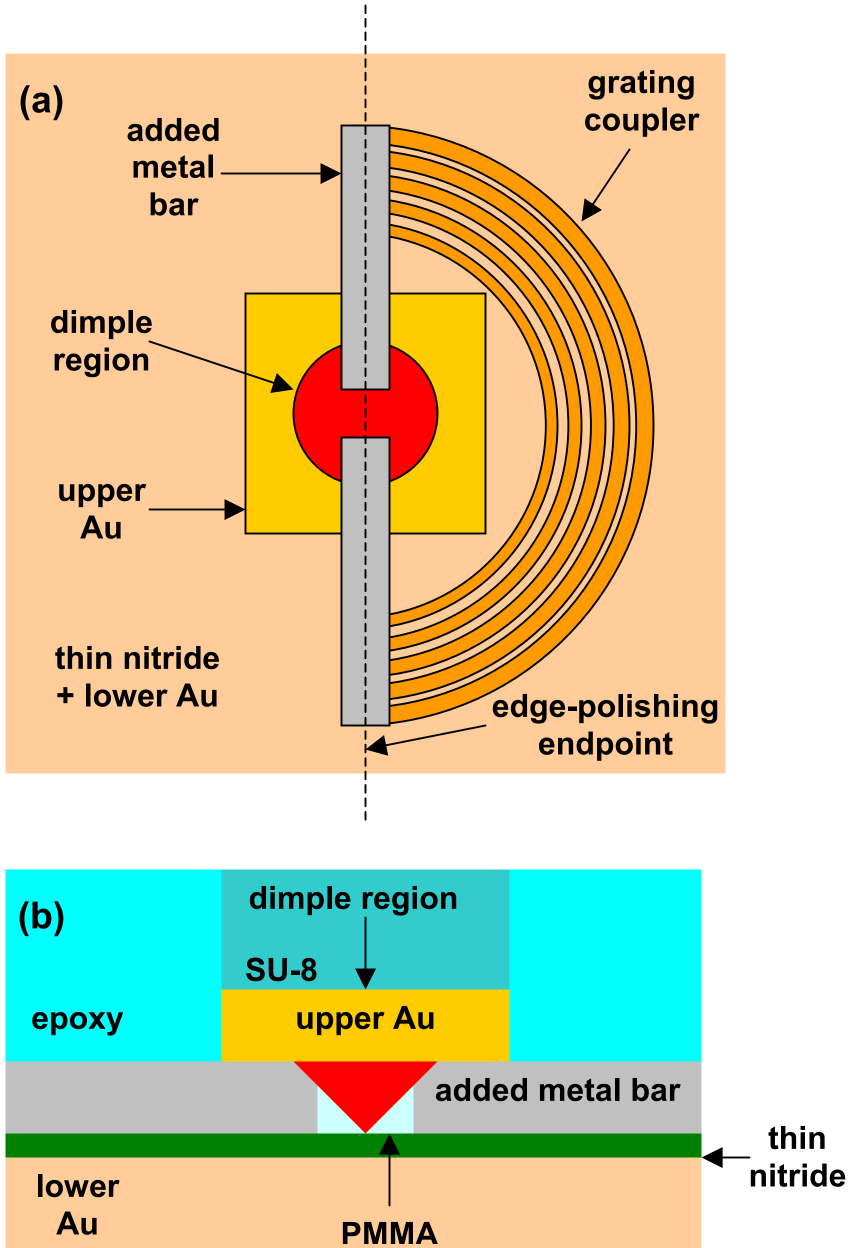

Figure 3-2. Darkfield dimple lens with metal bars
(a) Overhead view of proposed darkfield dimple lens structure prior to edge-polishing. Metal bars are added to regular dimple lens to help obscure light. (b) Cross-section view of what out-coupling facet would look like after edge-polishing. In the regular plasmonic dimple lens, the added metal bar areas would be transparent PMMA.

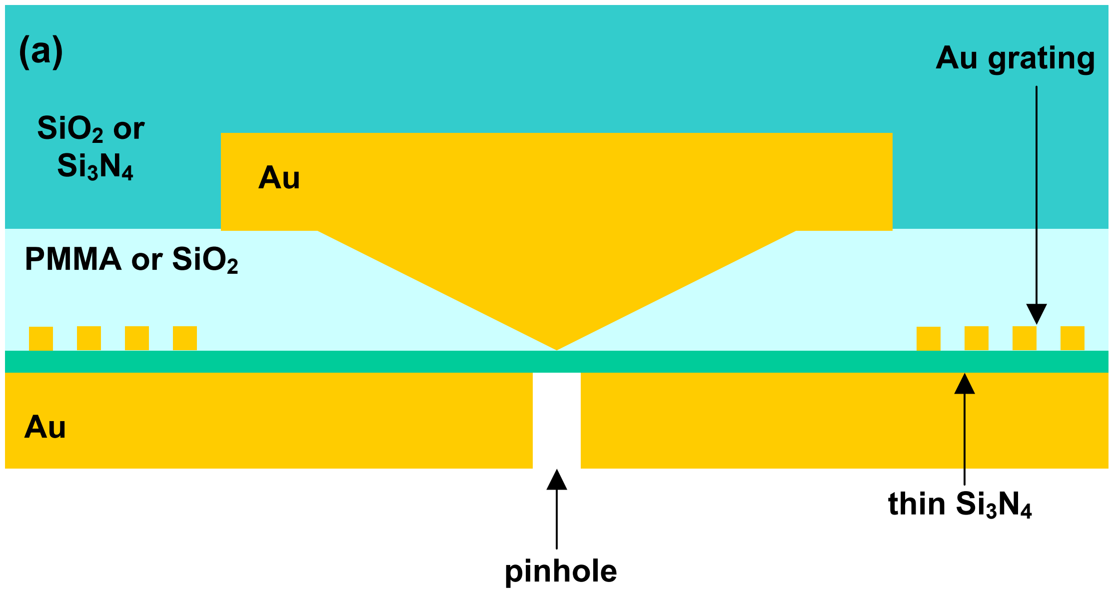

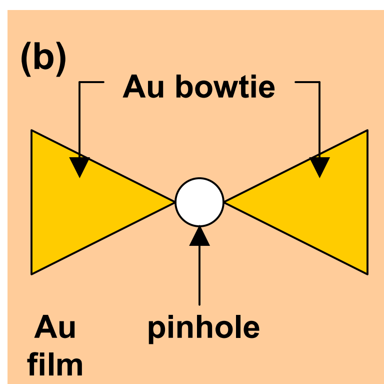

Figure 3-3. Alternative pinhole structures
(a) Schematic of one initial darkfield dimple lens concept, which incorporated a dimple lens structure with a traditional bullseye pinhole structure. The dimple structure couples to high k-vector double-sided surface plasmon modes, which would allow for more efficient coupling to a smaller pinhole. (b) Schematic of another darkfield lens concept, which uses a bowtie structure to couple to a pinhole.

Another method based on the plasmonic dimple lens that we considered is presented in Figure 3-3a. For this version of the device, we sought to incorporate our dimple lens onto a typical bullseye structure. By situating the dimple lens directly over the pinhole, one could potentially couple more efficiently to a smaller pinhole, similar to the concept of tailoring free space modes to match the desired optical mode in a fiber. A similar idea for improving coupling to a small pinhole would be to have a bowtie situated around a pinhole, as shown in Figure 3-3b. However, both of these structures would be difficult to align and fabricate, and we would also need to determine how they might be used to improve the coupling of light to the pinholes. However, if we could fabricate a pinhole-based device such as these, it could potentially be used to enhance the fluorescence of a molecule near or inside the pinhole, such as was shown in references [98, 99].

In order to better understand the coupling of light to the pinhole, such as for the pinhole with dimple device, we analyzed the modes of a cylindrical waveguide, which will be presented in Section 3.3.2. One result of this analysis was that the real part of the propagation constant for the lowest propagating mode in the hole becomes negligible, for a fixed frequency of light, when the hole is below a certain size. In order to have a propagating mode for smaller and smaller holes, one would need to work at a frequency closer and closer to the single-sided surface plasmon resonance frequency. Conversely, in order to use a frequency of light that is lower than the resonance frequency to have lower losses, there will be a limit to the size of the smallest uniform pinhole that can have light propagating through a thick metal film.

Furthermore, if the decay length of the mode is shorter than the penetration depth into the metal film, the background through the film will always be higher than the signal through the pinhole for any film thickness. Even if the wavelength of light and the size of the hole were chosen such that the decay length of the evanescent mode is larger than the penetration depth, the aforementioned pinhole with dimple lens geometry could still have improved losses if the pinhole were tapered, for the reasons discussed previously in Section 3.2. A tapered pinhole with dimple lens structure would also be similar to having a tapered version of the coaxial structure presented in references [100, 101], where the top metal layer of the dimple lens serves as the inner conductor.

However, since such a structure with two tapers would be very difficult to fabricate, we decided to analyze and fabricate the simpler tapered pinhole structure. As an intermediate step to the tapered pinhole structure that has cylindrical symmetry, we also fabricated tapered channel structures that have mirror symmetry, similar to the structure presented in reference [102]. The fabrication method for these tapered structures is discussed in more detail in Section 0.

3.3.2 Design – Cylindrical modes

In order to determine if there is any benefit to using a dimple lens to couple to a smaller pinhole, we analyzed the modes that would propagate down a small cylindrical waveguide (the pinhole case), with the geometry shown in Figure 3-4. Please refer to Appendix C for more details regarding this analysis. Using the electromagnetic boundary conditions corresponding to a pinhole, one can derive the existence of optical frequency modes that would propagate (i.e. have a non-trivial real portion for its propagation constant) down a narrow cylindrical waveguide and are analogous to the plasmonic modes of MIM structures [103, 55]. Similar modes have also been derived previously in the literature [100, 104, 105, 106].

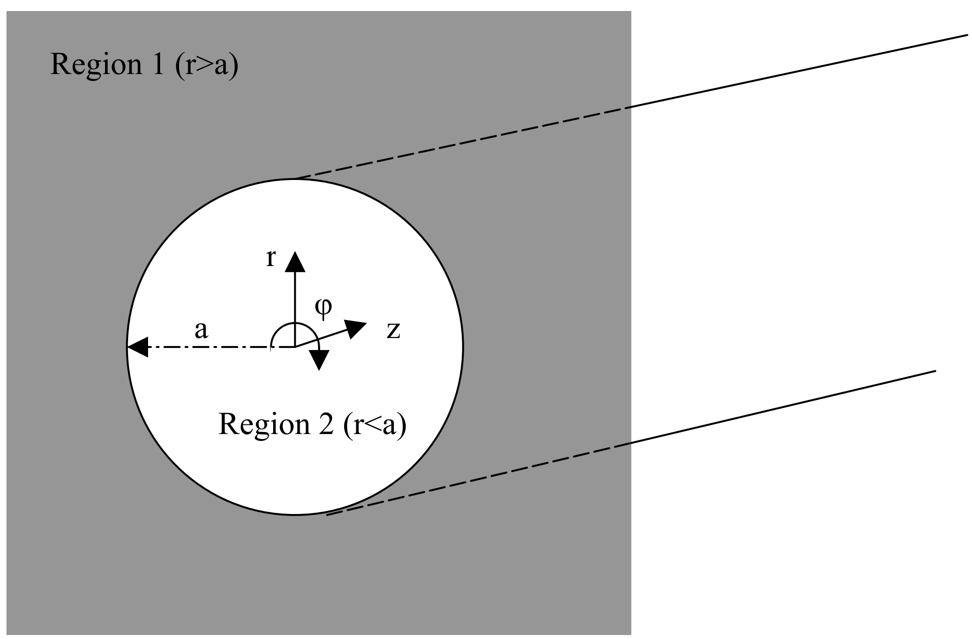

Figure 3-4. Cylindrical plasmonic waveguide
Geometry and coordinate system of the cylindrical plasmonic waveguide.

The nth order hybrid plasmonic modes of a cylindrical waveguide for propagation in the z-direction with propagation constant k_z at a frequency of operation ω can be described by the following equations:

$$E_{z1}(r,\varphi,z,t) = BK_n(\tau_m r)\cos(n\varphi)e^{j(\omega t - k_z z)} \quad H_{z1}(r,\varphi,z,t) = DK_n(\tau_m r)\sin(n\varphi)e^{j(\omega t - k_z z)}$$

$$E_{z2}(r,\varphi,z,t) = AI_n(\tau_d r)\cos(n\varphi)e^{j(\omega t - k_z z)} \quad H_{z2}(r,\varphi,z,t) = CI_n(\tau_d r)\sin(n\varphi)e^{j(\omega t - k_z z)}$$

$$E_{\varphi 1}(r,\varphi,z,t) = -\frac{j}{\tau_m^2}[\frac{k_z}{r}BK_n(\tau_m r)n\sin(n\varphi) + \omega\mu\tau_m DK_n'(\tau_m r)\sin(n\varphi)]e^{j(\omega t - k_z z)}$$

$$E_{\varphi 2}(r,\varphi,z,t) = -\frac{j}{\tau_d^2}[\frac{k_z}{r}AI_n(\tau_d r)n\sin(n\varphi) + \omega\mu\tau_d CI_n'(\tau_d r)\sin(n\varphi)]e^{j(\omega t - k_z z)}$$

$$H_{\varphi 1}(r,\varphi,z,t) = \frac{j}{\tau_m^2}[\omega\varepsilon_m\tau_m BK_n'(\tau_m r)\cos(n\varphi) + \frac{k_z}{r}DK_n(\tau_m r)n\cos(n\varphi)]e^{j(\omega t - k_z z)}$$

$$H_{\varphi 2}(r,\varphi,z,t) = \frac{j}{\tau_d^2}[\omega\varepsilon_d\tau_d AI_n'(\tau_d r)\cos(n\varphi) + \frac{k_z}{r}CI_n(\tau_d r)n\cos(n\varphi)]e^{j(\omega t - k_z z)}$$

where A, B, C, and D are scaling factors, and

$$\tau_{d,m}^2 = k_z^2 - \frac{\varepsilon_{d,m}\omega^2}{c^2} = k_z^2 - \varepsilon_{d,m}k_0^2$$

I_n and K_n are the nth order modified Bessel functions of the first and second kinds, respectively. Modified Bessel functions are essentially exponentials in a cylindrical coordinate system, without any nodes or peaks like those found in regular Bessel functions. So these modes are bound to the cylindrical metal-dielectric interface, decaying exponentially into both materials.

Some examples of the field and charge distributions of the n = 0 TM and n = 1 hybrid modes are shown in Figure 3-5. Since the n = 1 mode is the anti-symmetric charge case, it is analogous to the double-sided surface plasmon in the MIM slab case. Thus, this is the mode that we will focus on for the remainder of this section.

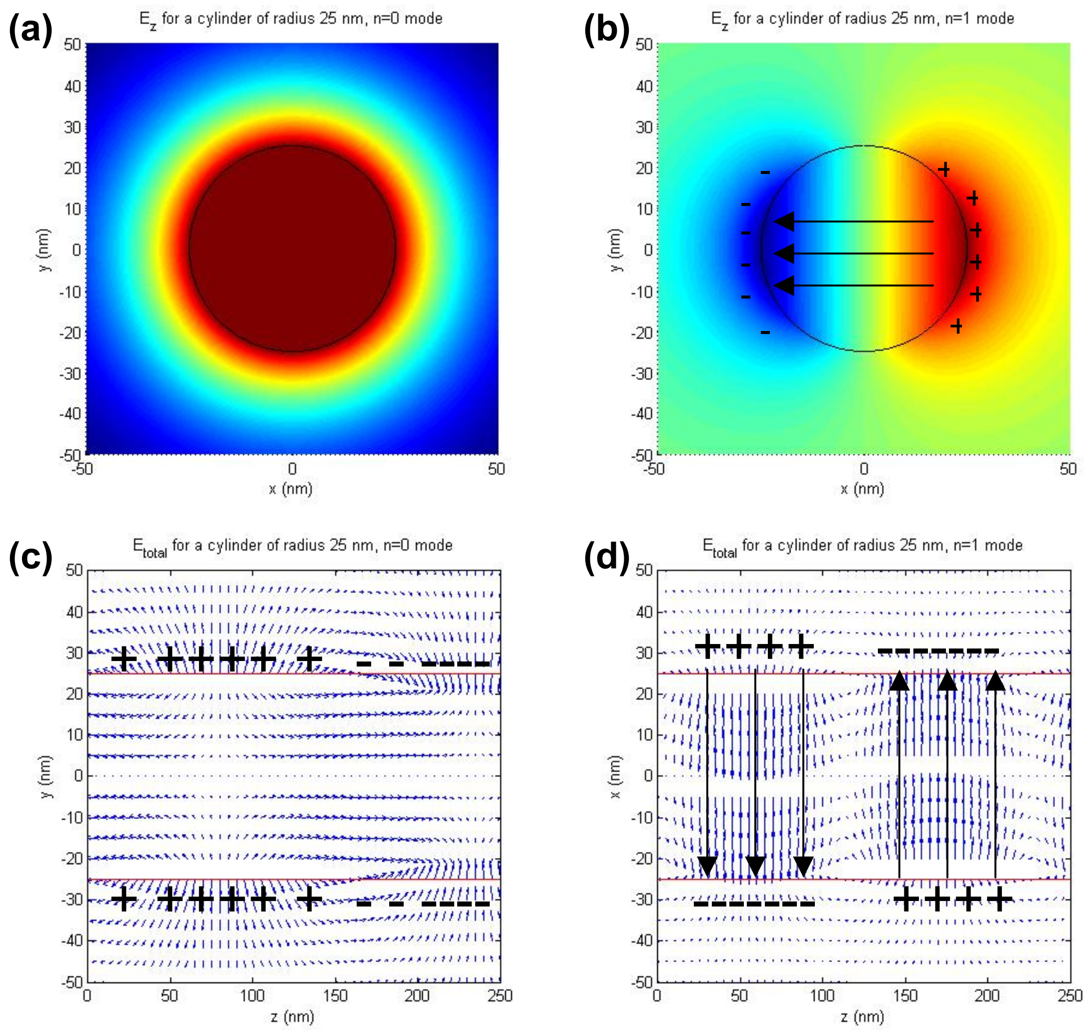

Figure 3-5. Plasmonic mode field distributions
Graphical representation of the analytically calculated fields for the plasmonic modes in a cylindrical waveguide. The top two plots show the z-component of the E-field for a cross-section transverse to the propagation direction for (a) the n=0 and (b) the n=1 TM plasmonic modes. The bottom two plots show the total E-field and charge distribution for a cross-section along the length of the waveguide for (c) the n=0 and (d) the n=1 TM plasmonic modes.

In order to satisfy the boundary conditions for a waveguide of radius a for the above hybrid plasmonic modes, one can equate the appropriate fields at the r = a boundary to give the following dispersion relation equation:

$$[\frac{\varepsilon_d}{\tau_d}\frac{I_n'(\tau_d a)}{I_n(\tau_d a)}-\frac{\varepsilon_m}{\tau_m}\frac{K_n'(\tau_m a)}{K_n(\tau_m a)}][\frac{1}{\tau_d}\frac{I_n'(\tau_d a)}{I_n(\tau_d a)}-\frac{1}{\tau_m}\frac{K_n'(\tau_m a)}{K_n(\tau_m a)}]=\frac{n^2k_z^2}{a^2k_0^2}[\frac{1}{\tau_d^2}-\frac{1}{\tau_m^2}]^2$$

This implicit equation for the n = 1 dispersion relation was solved numerically in Matlab with the dielectric constants for the Au-SiO_2 material system using the real parts of the dielectric constants found in reference [61]. The results are plotted in Figure 3-6, which shows the existence of a band of allowed modes for any given hole size. As one scales down the dimension of the pinhole, modes only exist for a narrow band of frequencies, with the lowest frequency getting closer and closer to the surface plasmon frequency. For light near the surface plasmon resonance frequency, having a high k-vector k_z means that τ_m is also large. Since $1/\tau_m$ represents the decay length into the metal, these modes would have a small spot size due to the confinement based on the field penetration into the metal, as was discussed in Section 3.2.

However, since the metal losses grow worse as the light approaches the surface plasmon resonance frequency, we may not be able to use these propagating high k-vector modes to efficiently transfer energy to a small spot due to the material losses. The losses would severely limit the thickness of the lower metal layer for pinhole diameters less than 100 nm, similar to the results found in references [104, 105]. This limitation engenders a quandary, since the thickness of the lower metal layer cannot be made too thin, due to the evanescent penetration of the single-sided surface plasmon on the top surface, in addition to the direct penetration of the input light discussed in Section 3.2.

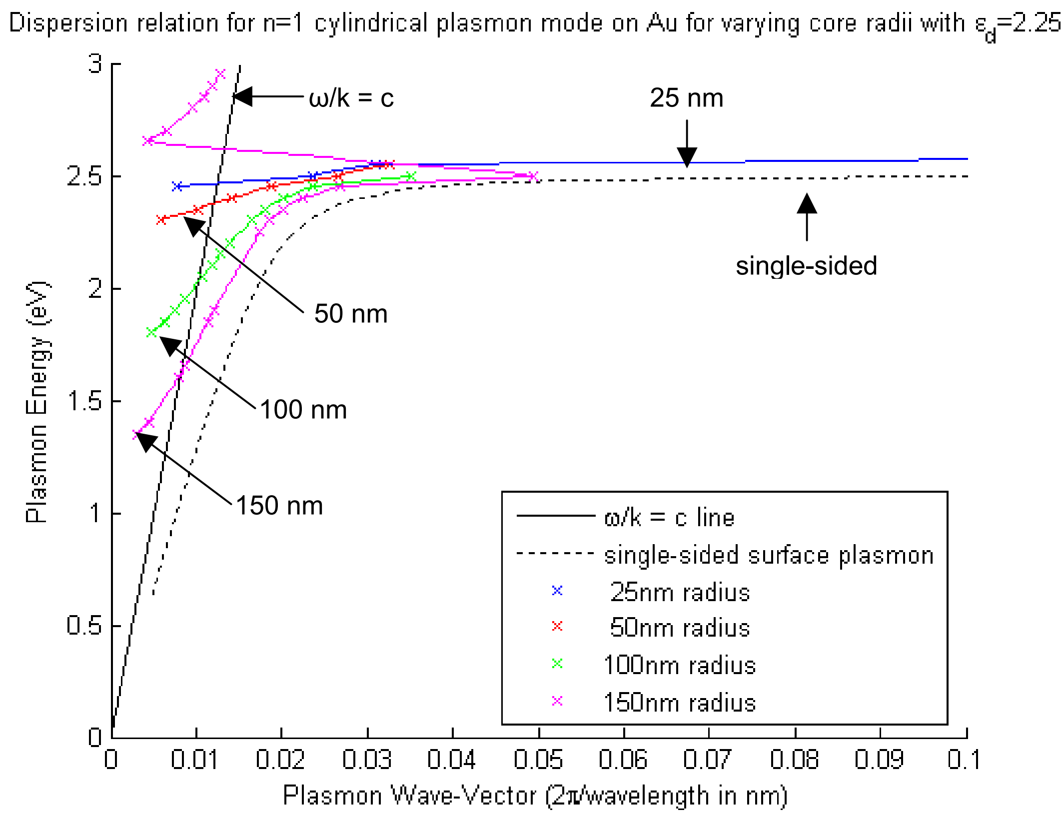

Figure 3-6. Au dispersion relations: n = 1 hybrid plasmonic mode
Dispersion relations for the n = 1 hybrid plasmon modes in a cylindrical waveguide for varying radii for the Au/SiO_2 system. These relations were obtained from a numerical solution of the implicit dispersion relation in Matlab.

Also, it should be noted that the results of reference [105] for the Al-glass material system show that there is a non-zero real propagation constant for all wavelengths. Although this may also be the case in the Au-SiO_2 material system with complex dielectric constants, it is important to consider the relative and absolute size of the imaginary part of the propagation constant, since this tells us how quickly the mode decays. Even if the real part of k_z is large, the mode may decay too rapidly if the imaginary part is also large. Conversely, even if the real part of k_z is not very large, there may still be low losses if the imaginary part is not too large either. In the latter case, one would still be able to limit the losses in the lossy region if you can taper quickly enough.

Thus, relying on our previous experience with the tapered structures in Chapter 2, we decided to consider a tapered pinhole structure, as shown in Figure 3-7. This tapered structure allows for focusing of light to a smaller final opening, while still retaining a large opening on the top surface to limit losses. Since we would also be using a circular grating to couple from free-space light to single-sided surface plasmons, this structure can be viewed as a modification of existing bullseye structures by replacing the standard pinhole with a tapered one.

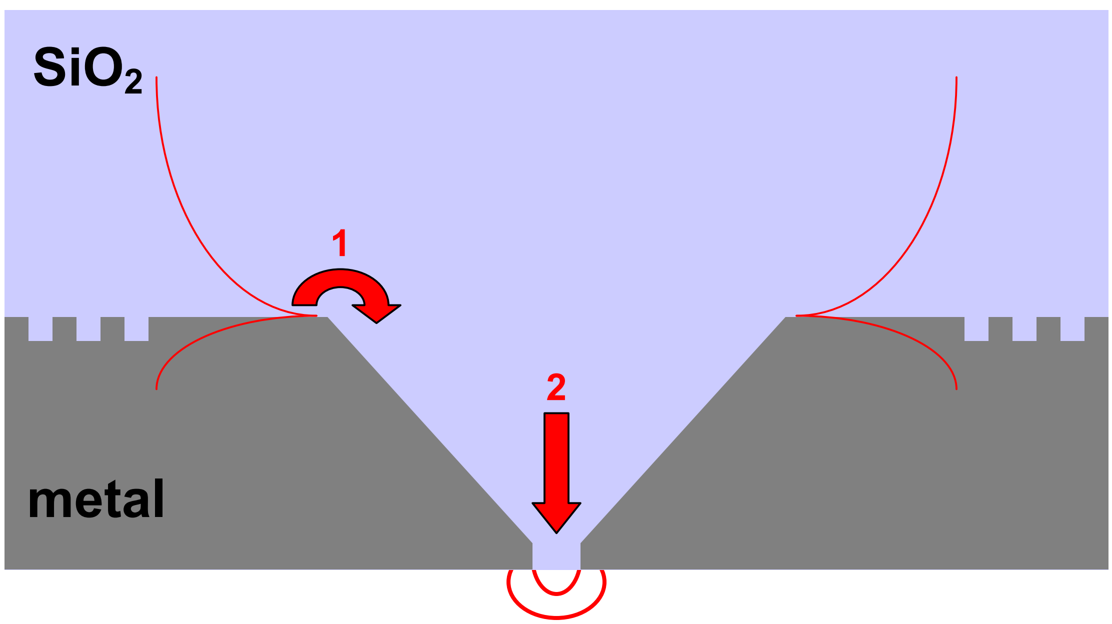

Figure 3-7. Darkfield funnel structure
The darkfield "funnel" structure is a modification of established bullseye with pinhole structures. The pinhole is tapered to provide a small final opening while still having a large opening on the top surface to limit losses. Surface plasmons on the top surface propagate towards the tapered pinhole to be focused when coming out the smaller bottom aperture. Red arrows indicate the two-step interpretation of the focusing process: first coupling into the funnel then propagating down the funnel.

In theory, one could use the above dispersion relation equation with complex dielectric constants to calculate the complex propagation constants for holes of varying sizes and wavelengths. The propagation losses could then be calculated from the imaginary part of the complex propagation constant, and one could integrate to find the total losses in a tapered structure. However, we were unable to converge on meaningful results for the complex propagation constant using the numerical calculation method with complex dielectric constants. Thus, in order to estimate the losses in a tapered pinhole structure, we turned to alternative methods of estimating the losses, as will be discussed in Section 3.6.

3.3.3 Design – Tapered funnel

To analyze the performance of a tapered "funnel" structure, we first consider the channel case (1D tapering) in lieu of the pinhole (2D tapering). One way to analyze this device is to consider the funnel structure as acting via a two-step process, as indicated by the red arrows in Figure 3-7. The first step is to couple light from the top surface into the funnel region. The second step then focuses and propagates this light to the output aperture at the bottom.

The lower portion (step 2) of the funnel structure in Figure 3-7 is the same as the tapered geometry shown in Figure 2-2a for coupling double-sided surface plasmons from a wide channel to a narrow channel. This tapered region has been optimized previously to have an approximately 30° taper angle for the dimple lens [55]. Thus, we only need to be concerned with the optimization of the upper portion (step 1) of the funnel structure. This first step must couple from two horizontally propagating single-sided surface plasmons on the top surface into one double-sided surface plasmon in the pinhole.

To optimize the upper portion of the funnel structure, we used the commercially available Finite-Element Method (FEM) electromagnetic simulation software called COMSOL. The two types of coupling structures considered were a linear profile and a curved profile, as shown in Figure 3-8a and Figure 3-9a. We varied the angle for the linear profile and the radius of curvature of the curved profile, which yield optimization curves shown in Figure 3-8b and Figure 3-9b.

(a)

(b)

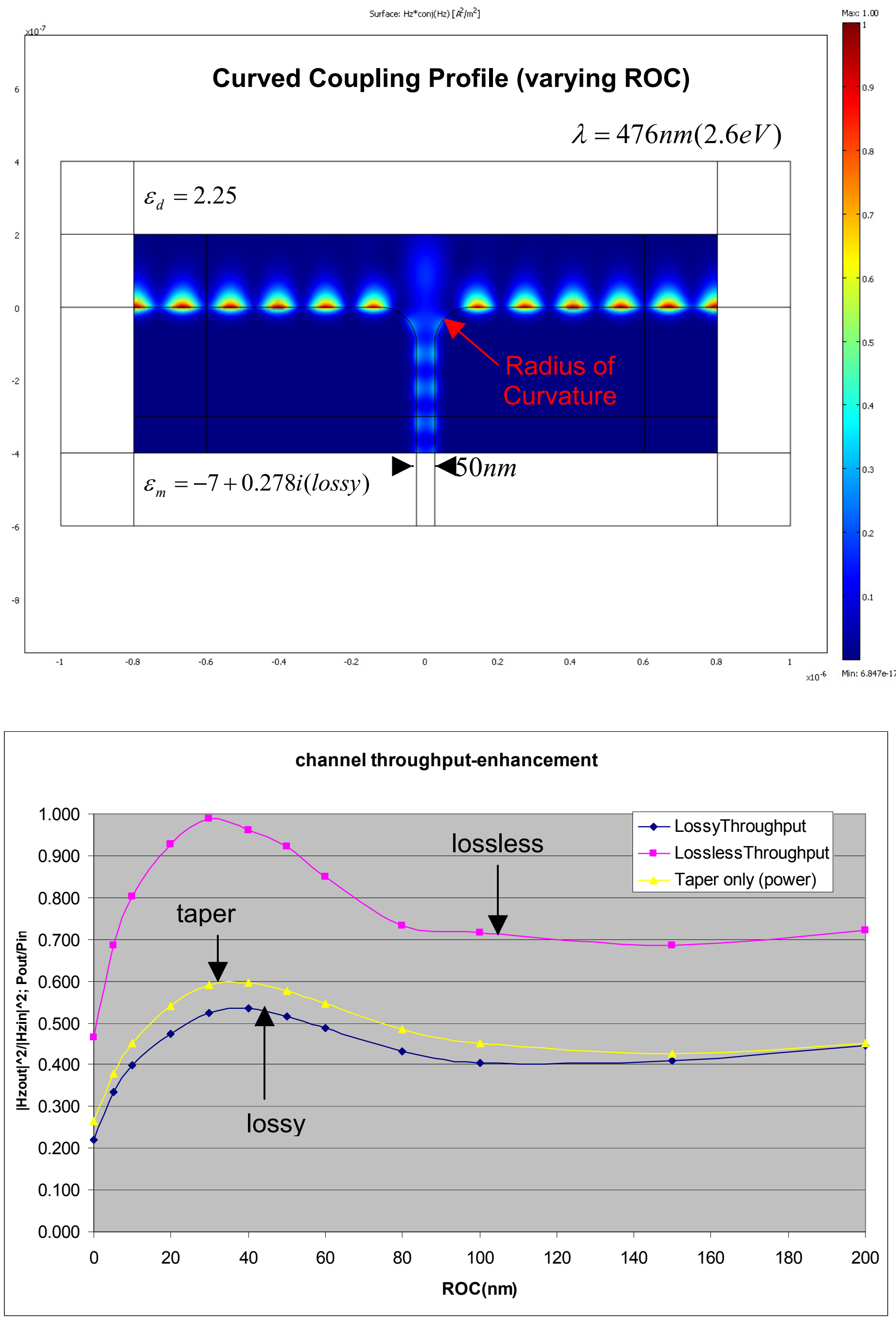

Figure 3-8. Curved coupling profile optimization
(a) Optimization structure for a curved coupling profile in a SiO_2-Ag structure at a 476 nm wavelength of operation to a final pinhole width of 50 nm. (b) Results of varying the radius of curvature for this structure. An optimal radius of curvature was found to be around 30-40 nm.

(a)

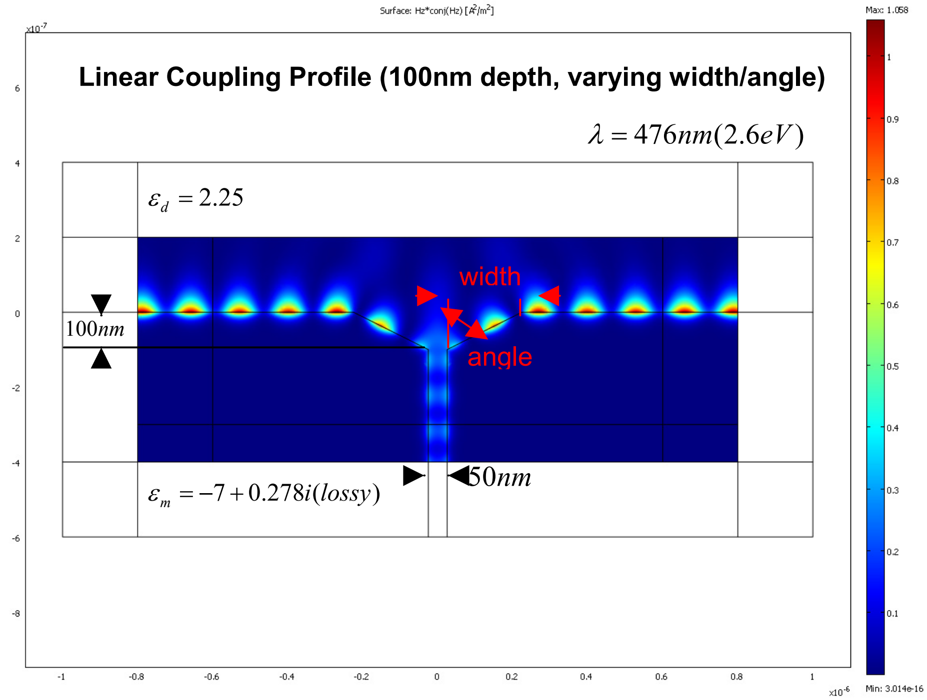

(b)

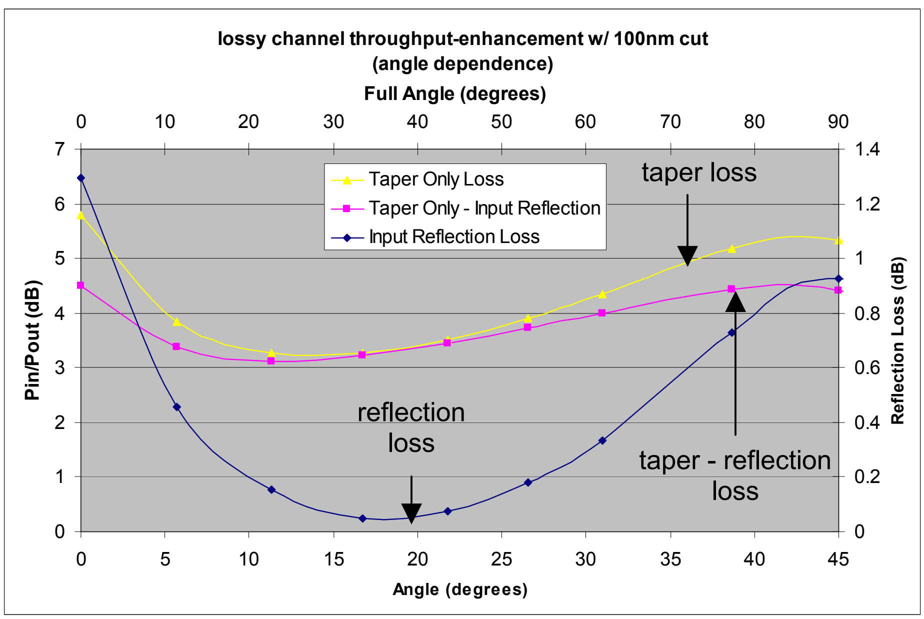

Figure 3-9. Linear coupling profile optimization
(a) Optimization structure for a linear coupling profile in a SiO_2-Ag structure at a 476 nm wavelength of operation to a final pinhole width of 50 nm. (b) Results of varying the angle of the taper for this structure. An optimal taper angle was found to be around 30°.

The curved profile has an optimum radius of curvature around 30-40 nm for a 50 nm diameter hole, and the linear profile has an optimal angle of about 15° for one side, or 30° for the whole opening. Thus, the optimal angle for the upper coupling region using a linear profile appears to match the optimal taper angle for the lower focusing region. Therefore, it would not be necessary to connect the angles between these two steps by incorporating a curved region between the two linear regions.

The curved coupling profile was also found to have ~20% more throughput than the linear coupling profile, based on these analyses. However, such a curved profile may be more difficult to fabricate. We also did a fabrication sensitivity analysis by varying the radius of curvature for a fixed 45° taper angle, as shown in Figure 3-10a. The results in Figure 3-10b show that the radius of curvature does not have a significant effect on the throughput of the tapered structure until the curvature is ~50-100 nm, which is on the same order as the taper size.

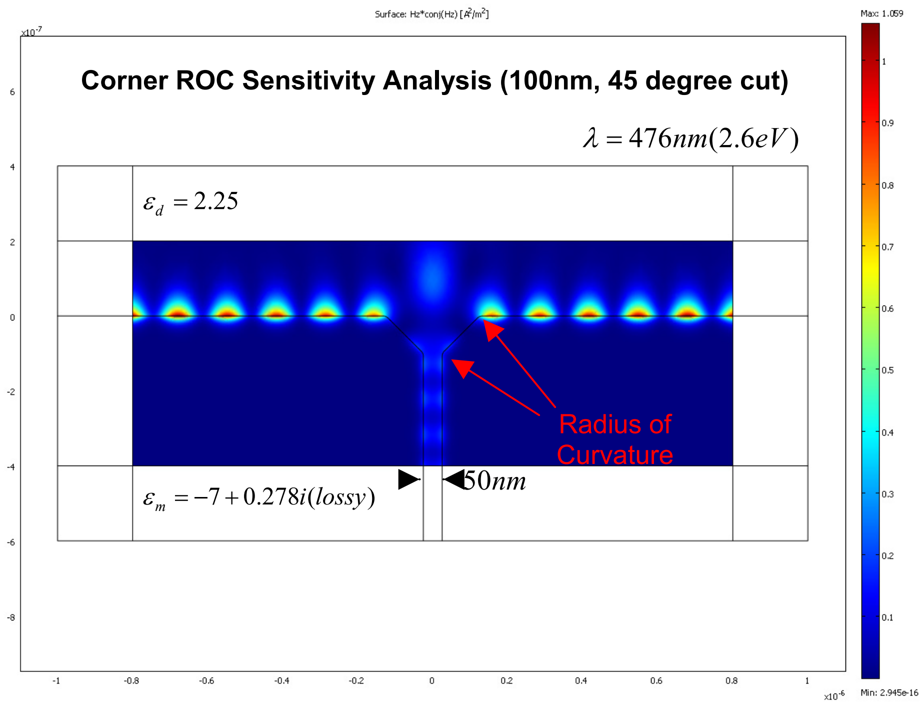

(b)

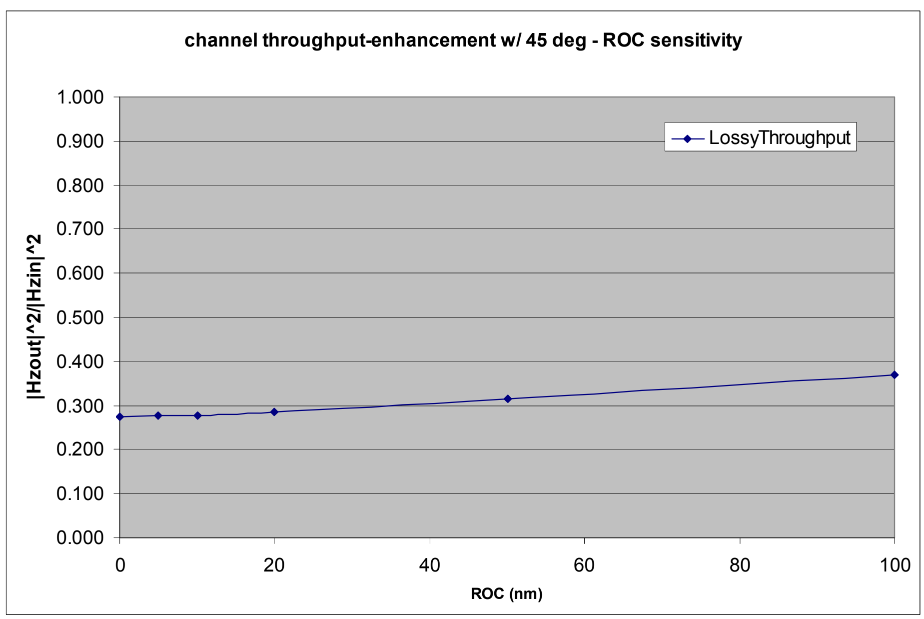

Figure 3-10. Corner curvature sensitivity test
(a) Optimization structure for testing sensitivity to radius of curvature for a SiO_2-Ag structure at a 476 nm wavelength of operation in a 45° structure. (b) Results of varying the radius of curvatures for this structure. The throughput was not greatly affected for small radii of curvature.

Fabrication

For the fabrication of the device proposed in Figure 3-7, we would like to be as close as possible to the optimized parameters found in the Section 3.3.3. Specifically, the device should have a fairly narrow tapering angle; having a wide area of thin metal at the center of the device would allow too much evanescent light to leak through, as discussed in Section 3.2. This requirement restricts us from using certain fabrication methods. For example, we cannot take the curved dimple profile in PMMA and simply etch transfer it into a metal layer.

There are two basic approaches to fabricating such a tapered structure in metal and dielectric, as depicted in Figure 3-11. The first approach is to make the desired shape in a dielectric, which allows for sharp corners, and then backfill with metal. Although this approach would require some method to remove the metal covering the very tip of the dielectric, it also allows near-field access to the optical output of the structure. The second approach to fabricating the tapered structure is to etch the desired profile into a metal layer, and then backfill it with dielectric. In order to have near-field optical access for this second method, it would be necessary to remove the substrate without damaging the metal or dielectric film.

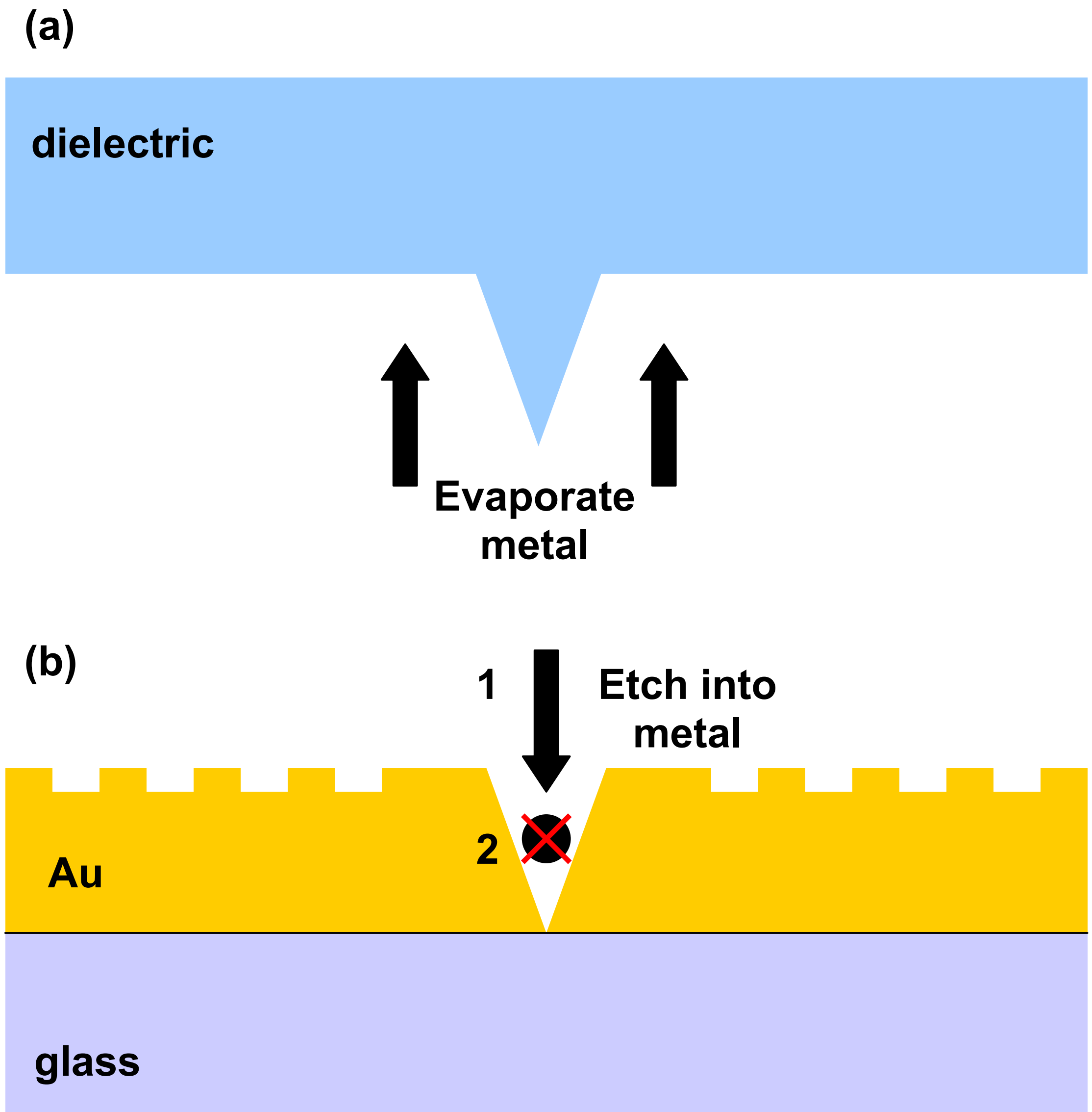

Figure 3-11. Tapered profile fabrication methods
Two basic methods of fabricating the desired tapered darkfield profile. (a) Fabricating a sharp taper in a dielectric and then backfilling with metal. (b) Etching into a metal film on a substrate, such as with FIB milling normal to the surface (indicated by arrow labeled 1), or parallel to the surface (arrow labeled 2).

An alternative to backfilling with dielectric would be to leave the tapered region empty, using air as the dielectric. Again, this does not allow for access to the near-field optical output unless the substrate is removed to create a free hanging membrane. However, the far-field throughput of such a device could still be measured if the metal layer is supported by a transparent substrate such as glass. Since fabricating a metal-air taper on a glass substrate was the simplest way to test our structure, this is the type of device we fabricated. If a near-field measurement is desired, some examples of possible fabrication schemes for near-field measurements, based on releasing the films from their substrates via KOH etching, are also shown in Figure 3-12.

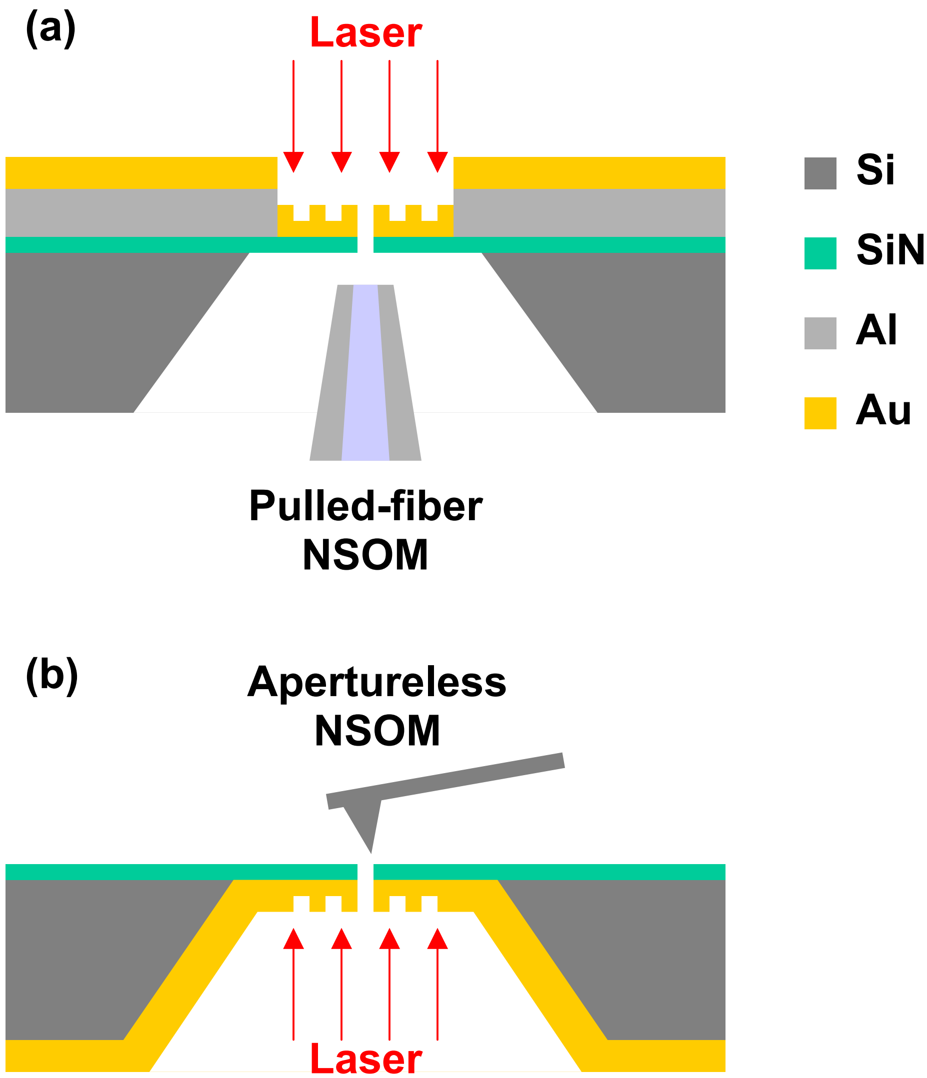

Figure 3-12. KOH based near-field accessible fabrication methods
Two methods of fabricating a tapered darkfield profile which are compatible with near-field measurement systems, based on KOH etching: (a) scanning the output from the bottom using a pulled-fiber NSOM probe, and (b) scanning the output from the top using apertureless NSOM.

There were several methods that were considered for fabricating the desired tapered structure. One method was to use a resist reflow method to create the desired curved profile in a resist such as PMMA, as shown in Figure 3-13a [107, 108]. This curved profile could then be pattern transferred into the underlying metal layer using a dry etch. One drawback of this pattern transfer approach is that it would roughen the final surface. Another approach could be to fabricate two adjacent circles to create a cusp, such as by evaporation or etching with nanospheres as a mask [109]. This method would be limited to a taper in only 1D, as shown in Figure 3-13b. A taper in 2D could be obtained by using an undercut method, such as in the fabrication of high-aspect-ratio (HAR) tips for AFM [110].

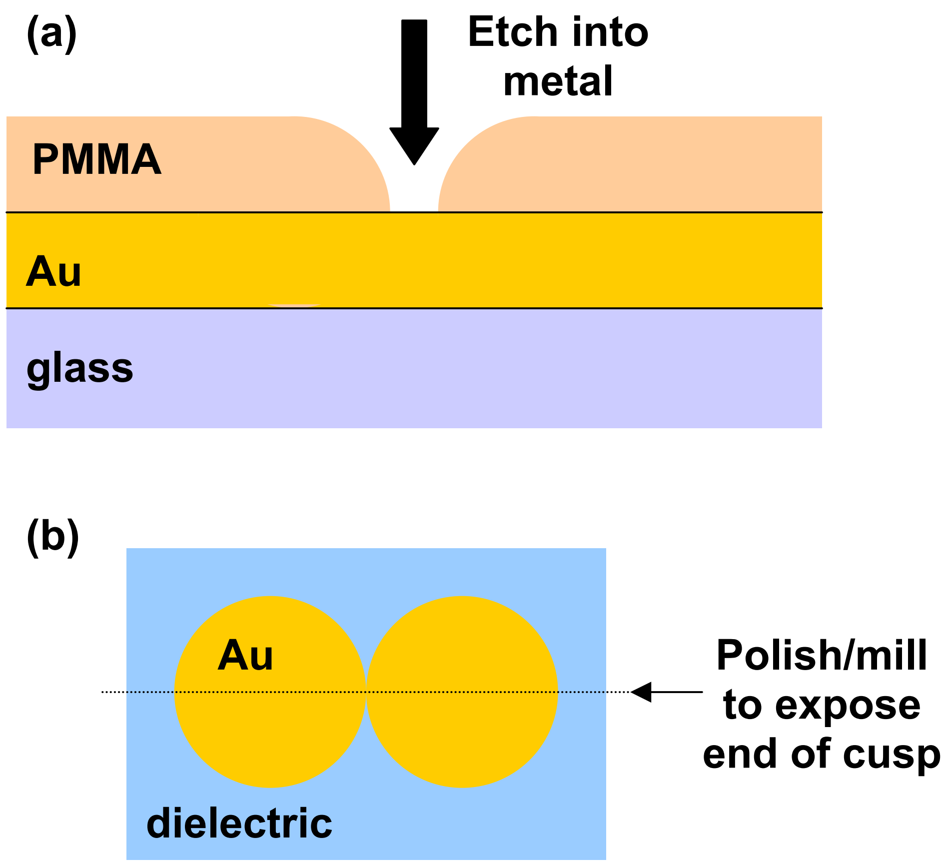

Figure 3-13. Sharp taper fabrication methods
Examples of fabrication schemes that can produce a sharp taper: (a) using a resist reflow method to create a mask to etch into metal and (b) creating a cusp from etching or evaporating adjacent circles.

Although Focused Ion Beam (FIB) can also be used to create dielectric tips [111], it is simpler for our purposes to use the FIB milling to directly fabricate the tapered pinhole in a metal film, as shown in Figure 3-11b. Although FIB milling can make smooth sidewalls (parallel to the beam), it has a tendency to leave a very rough surface at the end of the beam (normal to the beam) [112]. However, although FIB milling from the side allows for greater control of the shape and smoothness, it limits the structure to being an extrusion of the 2D milled geometry (i.e. a wedge instead of a funnel). Since working with a substrate for sideways milling is also more difficult, we instead chose to use FIB milling only normal to the surface.

To fabricate the samples for our tapered darkfield devices, we began with a glass substrate onto which a 300 nm film of Al was evaporated using a Sloan e-beam evaporator. This Al film was patterned with photolithography to have 15 μm square holes for alignment purposes. The Al film helps to block out any stray or scattered light for most of the sample. Next, a blanket 300 nm layer of Au was deposited using the Sloan evaporator. A thick layer of Au is necessary to prevent evanescent penetration of light directly through the film. Since Au has a skin depth of ~30 nm at 633 nm, this gives us a background power level of about –80 dB. The darkfield devices were fabricated within the 15 μm squares where there was only the Au film on top of the glass substrate.

A FEI Nova 600 NanoLab was then used to FIB mill our structure in the Au film. This machine has a DualBeam system that provides SEM imaging for positioning prior to fabrication and for inspection of devices after fabrication with the FIB. Both the SEM and the FIB could also be used in the deposition of metals such as platinum (Pt) and tungsten (W) from organometallic precursor gases. In our initial tests, we used SEM-assisted Pt deposition to protect the device shape prior to FIB milling it to obtain a device cross-section for inspecting the taper shape.

The device was fabricated using method 1 of Figure 3-11b, where the grating grooves and the tapered hole were both milled normal to the surface, in two separate but aligned steps. Using FIB, we fabricated both pinhole devices (circular grating with pinhole) and channel devices (linear grating with channel), with varying hole and channel sizes. These different devices were chosen to test the effect of varying aperture size on the throughput, as well as to compare the effect of having a taper in 1D versus a taper in 2D.

The hole and channel sizes were nominally 400 nm, 200 nm, 100 nm, 50 nm, and 5 nm (singe pixel) wide at the top. Cross-sections with Pt deposition were used to ascertain the stopping point for when the hole was etched through the film, as well as to examine the size and shape of the tapers. An example of the cross section of one of these tapered holes is shown in Figure 3-14, which has a 40 nm final aperture size and a taper angle within the optimal range.

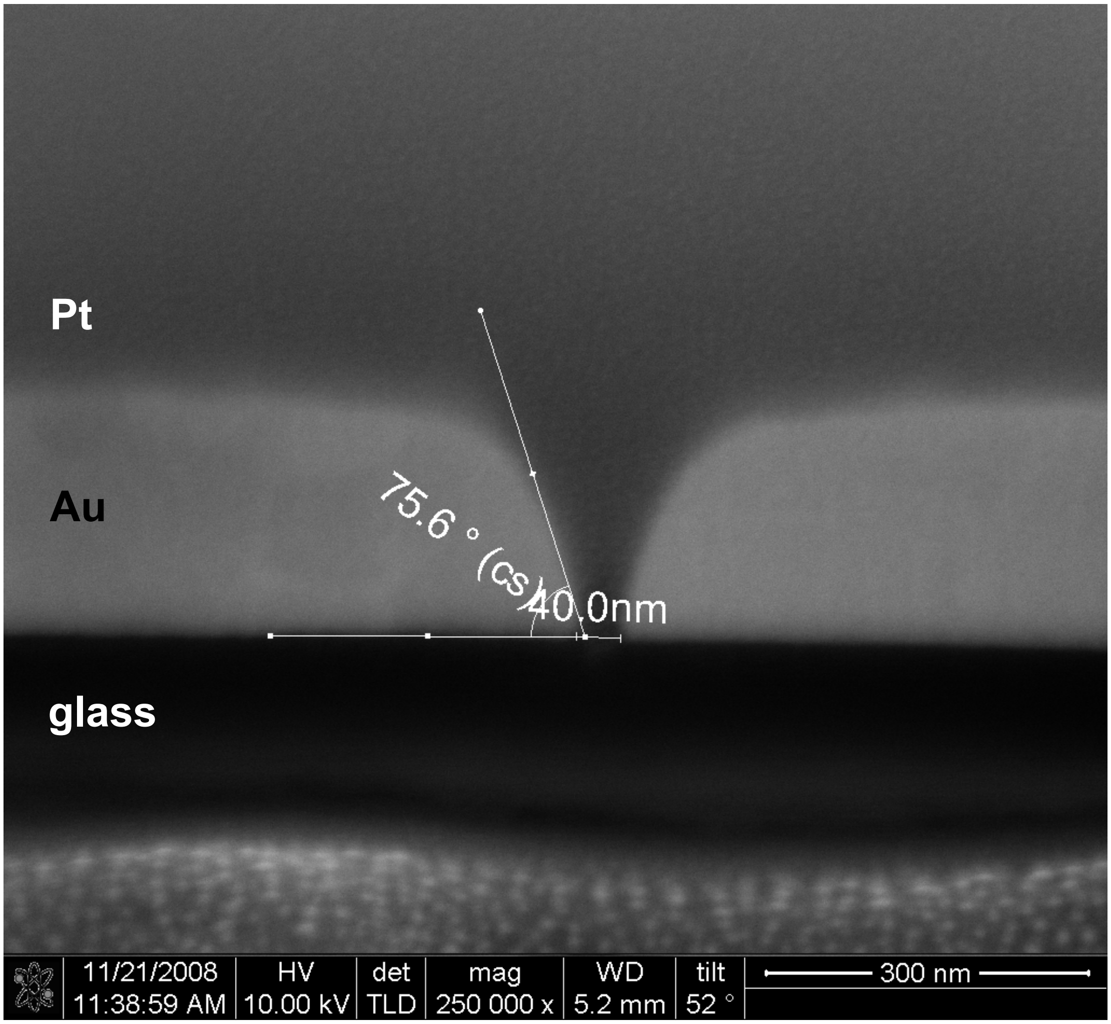

Figure 3-14. Fabricated tapered pinhole cross-section
SEM image of the cross-section of a tapered funnel region of the channel darkfield focusing device which was fabricated using FIB. A tapered pinhole was fabricated in a 300 nm Au film on a glass substrate. Pt was used to protect the device shape for the cross-section image.

The gratings for all of these devices consisted of four grooves on each side of the holes. These grooves were 200 nm wide and had a 600 nm period, for a total area of about 5 μm x 5 μm. The period was chosen from the theoretical single-sided surface plasmon wavelength for a gold–air interface. The FIB milling conditions were selected so that the grating grooves were about 20-30 nm deep as measured from the cross-sections and AFM scans. This groove depth was chosen based on the gratings heights that were used for the dimple lens in Chapter 2. The remaining grating parameters were not optimized. Examples of these gratings can be seen in the angled overhead view of a circular grating and the cross-section view of a linear grating, which are shown in Figure 3-15 and Figure 3-16, respectively.

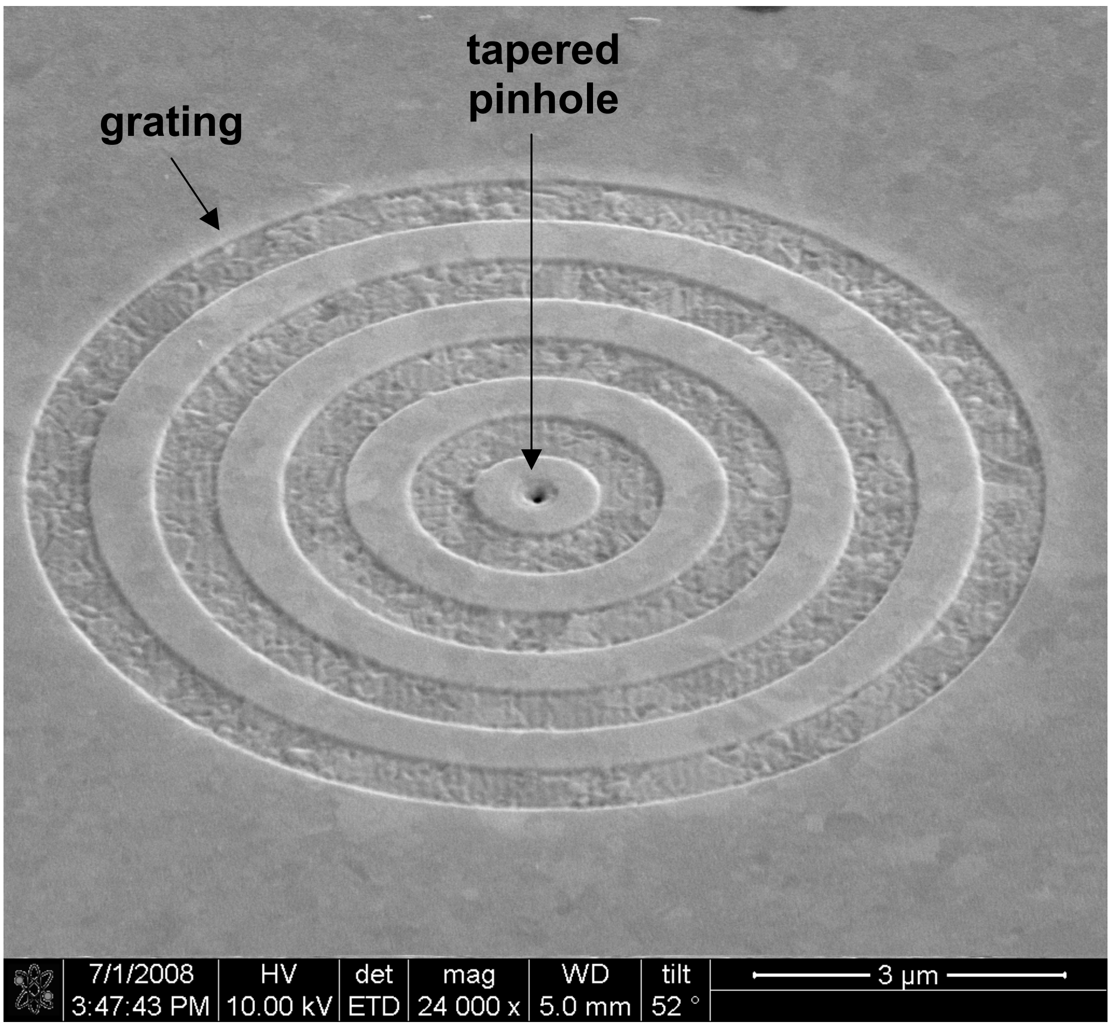

Figure 3-15. Pinhole device with circular grating
SEM image of a pinhole darkfield focusing structure, as viewed from an angle from above. The device consists of a circular grating coupler surrounding a tapered pinhole. FIB was used to fabricate the grating and pinhole in a Au film on a glass substrate.

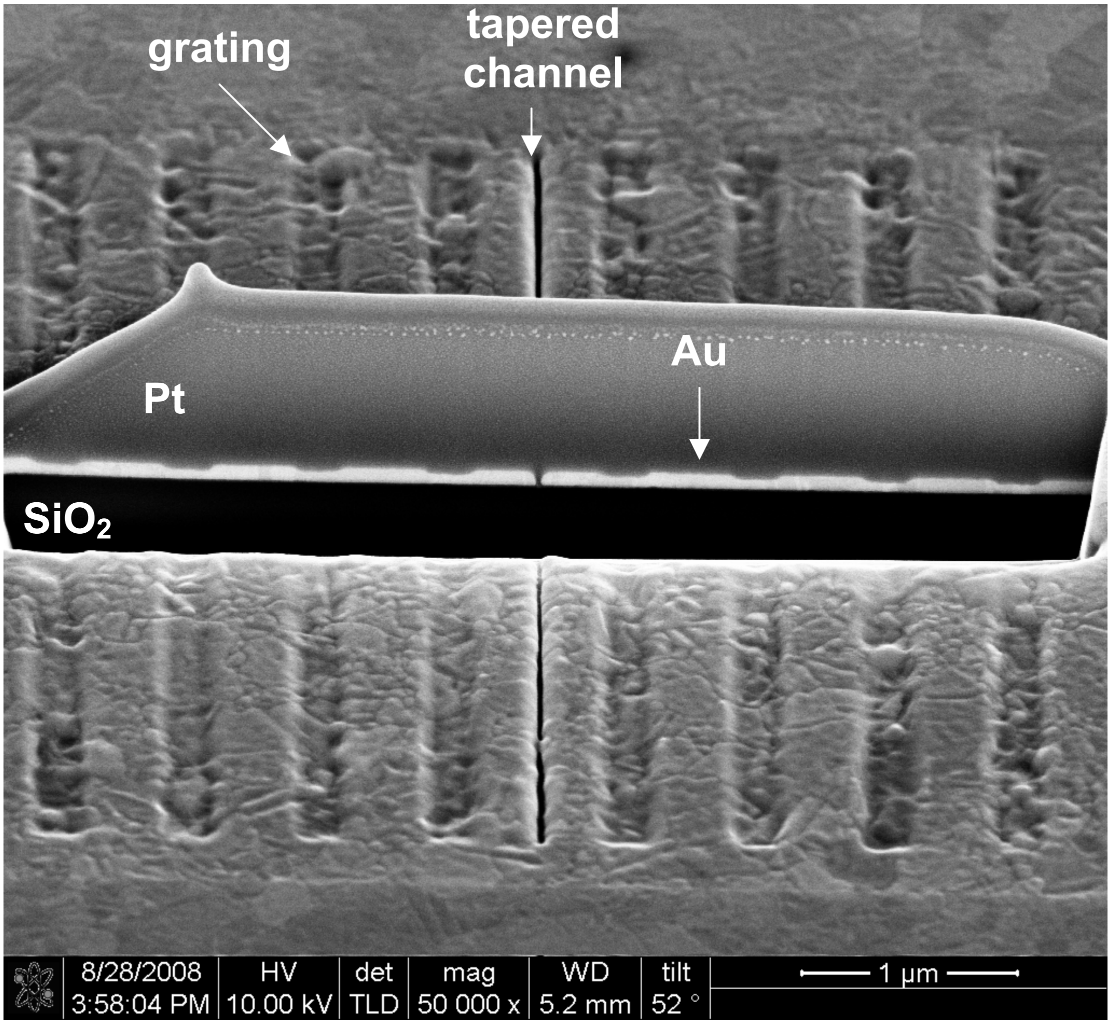

Figure 3-16. Channel device with linear grating
SEM image of a channel darkfield focusing structure, as viewed from an angle from above. The device consists of a linear grating coupler surrounding a tapered channel. FIB was used to fabricate the grating and channel in a Au film on a glass substrate. Part of the device has been milled away using FIB to expose a cross-section of the device. Pt was deposited on top of the milled area prior to cross-section to protect the device shape.

3.4 Measurement

For our test structures, we fabricated the darkfield plasmonic focusing device on a glass substrate since it greatly simplified the fabrication process, as described in the previous section. However, since we did not remove the glass substrate, we could not to do a near-field measurement on the output of the device to determine the spot size. In order to determine the optical resolution at the output of the device, one would need physical access to the output aperture. This would be possible if the device consisted of metal evaporated onto a tapered dielectric structure or if the substrate were removed from the device, such as for the structures shown in Figure 3-11a and Figure 3-14.

In order to test our devices, we instead used a far-field throughput measurement, as shown in Figure 3-17, to investigate the effect of varying the device's final aperture size on the throughput. This measurement method also allowed us to examine the differences in throughput for a channel device as compared to a pinhole device. Unfortunately, we did not have enough control in our FIB fabrication to precisely measure the effect of varying the angle of the taper on the throughput. However, based on the simulation results from Section 3.3.3, there is a fairly broad range of tolerable taper angles and curvatures. In contrast, the size of the final aperture is expected to have a much greater effect on the throughput, based on the theory of the throughput of small holes [67, 68], and the radiation from small antennas [24], as will be discussed further in Section 3.5. Thus, we neglect the effect of the exact taper shape in our analyses, since we can assume that, within the tolerances of the fabrication method, the taper shape has a much smaller effect on throughput than the size and shape (i.e. pinhole versus channel) of the final aperture.

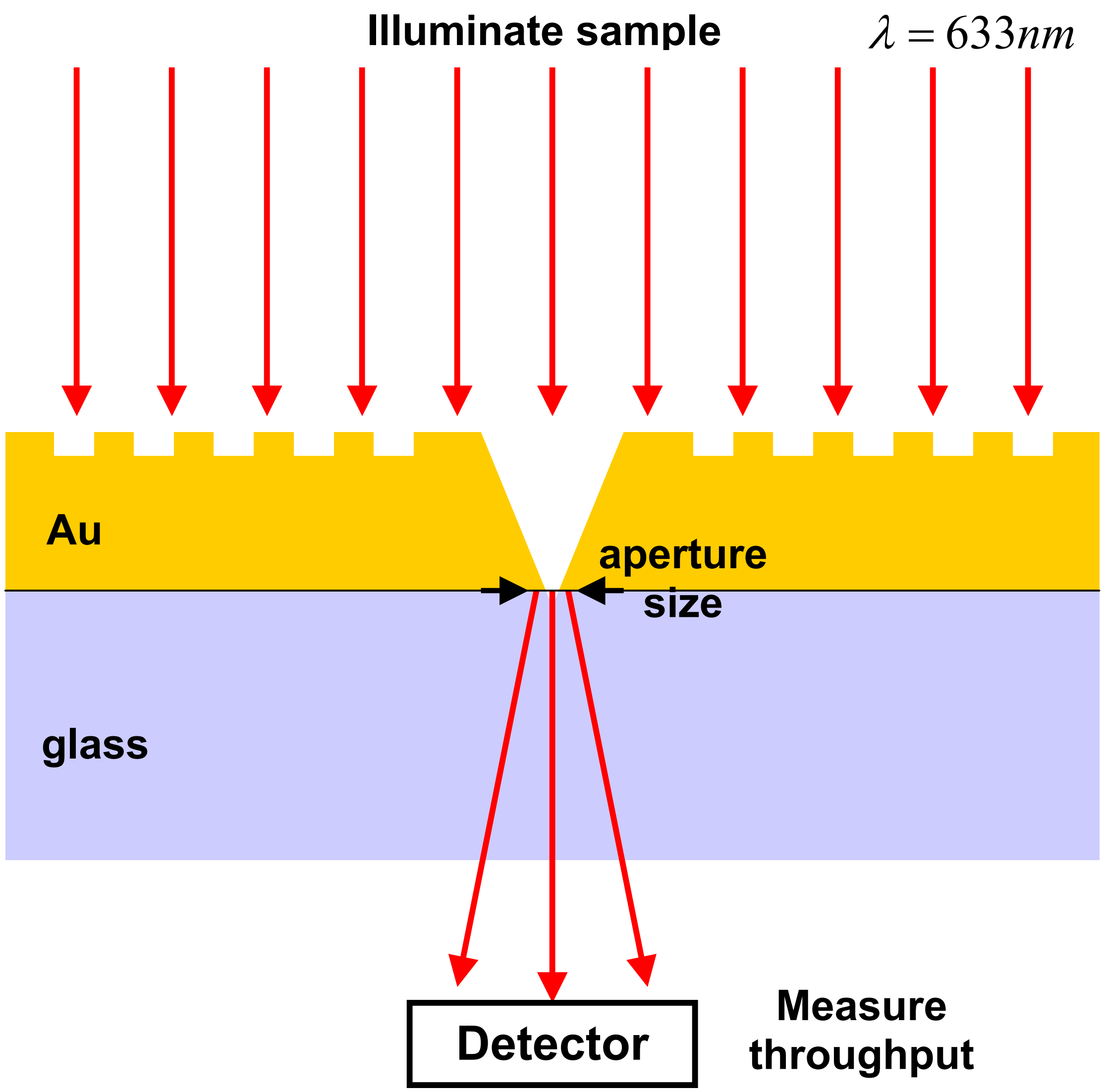

Figure 3-17. Far-field throughput measurement schematic
Schematic of the concept for the far-field throughput measurement for the darkfield plasmonic focusing device. 633 nm wavelength light is incident from the top on the tapered pinhole and grating. The throughput is measured through the glass substrate with a detector in the far-field at the bottom.

The throughput through the darkfield device was measured using an optical setup as shown in Figure 3-18. 633 nm light from a JDS Uniphase 10 mW HeNe laser was first modulated at ~150 Hz using a Stanford Research Systems SR540

Chopper before being coupled into a Thorlabs P1-460A-FC-2 single mode fiber. The chopper was used to modulate the laser light for the lock-in amplifier, which limits the effect of 1/f and 60 Hz electrical noises in our measurement. Neutral density (ND) filters were also used to attenuate the light entering the fiber by up to 70 dB, depending on the necessary signal levels (e.g. lower power for aligning, higher power for measurements). The output of this fiber was connected to a collimator that produced a beam ~5 mm in diameter. This beam was then polarized and passed through a half-wave plate that could be used to rotate the polarization.

Next, the laser light was split using a beam splitter, with one beam as a reference and the other continuing on to a microscope objective (0.45 NA, 50x) to be focused on the sample. The reference beam, which was essentially equivalent to the input power, was measured using a Thorlabs DET110 High-Speed Silicon Detector. The signal from this reference arm was fed into a Stanford Research Systems SR570 Low Noise Current Preamplifier before being input to a Stanford Research Systems SR830 DSP Lock-in Amplifier as an Aux Input. This reference was used to account for variations in the input laser power, which drifted over time and also varied with polarization.

The other beam was focused on the sample, and the signal light that passed through the darkfield device was measured in the far-field (~5 mm behind the sample) using a Newport 818-SL Silicon Low Power Detector. This signal was used as the main measured signal for the SR830 Lock-in; it represents the output power of the darkfield device. This output power signal was first normalized by the input power from the reference arm, which was read from the Aux Input, to account for laser power fluctuations. This result would give us the far-field throughput for the device if the reference arm were equal in power to that incident on the device.

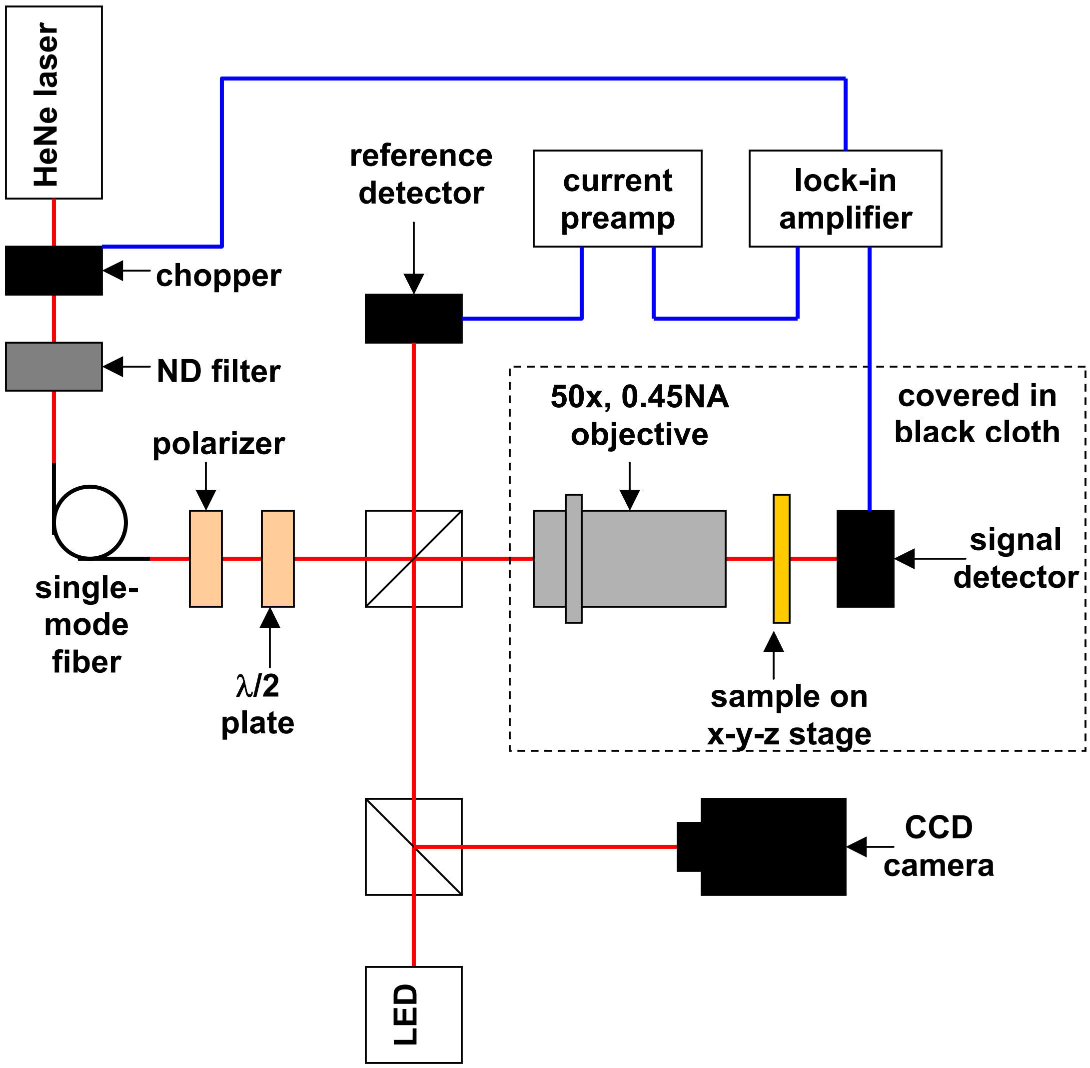

Figure 3-18. Darkfield throughput experimental setup schematic
Schematic of the actual experimental setup used for the far-field throughput measurement for the darkfield plasmonic focusing device.

However, the power in the reference beam and the power reaching the sample differed slightly due to the effects of the beam size, the light's polarization, and the microscope objective. Thus, the above throughput result was further normalized by a similar throughput measurement made on a sample with only a 15 μm square hole in an Al film on a glass substrate, without any Au. A 30 second integration time was used on the lock-in for these measurements to improve the SNR by decreasing the bandwidth for thermal and shot noise. For the maximum power used, these measurement settings gives a minimum noise level comparable to the background expected through the 300 nm thick Au from evanescent penetration.

The samples were positioned using a manually controlled x-y-z translation stage. A red LED was also used to help illuminate the sample during positioning; the sample was imaged on a QN-902 B/W CCD camera. This LED was turned off during the throughput measurements. The microscope objective, the sample, and the Newport detector were also covered with black cloth (except at the input of the objective) to minimize any stray background light.

For these measurements, we also compared devices with and without gratings. The presence of the gratings did not seem to have a significant effect on our throughput results (possibly because the grating was poorly designed, or because the laser spot was mostly on the hole rather than the grating). However, the gratings were still useful in locating the holes for laser alignment, especially for the smaller holes. As a result, the above throughput measurements were further normalized to the area of the holes, given that the focused laser spot was ~3 μm in diameter, as measured from the CCD camera. The background noise level from a blank Au film with no device (i.e. the evanescent penetration) was also subtracted from the measurements. This only significantly affected the results for the devices with the smallest aperture size, which were closest to this noise level.

The effect of the polarization of the laser light was also tested; there was no effect, except on the channel devices, as one would expect. We will present the results from the measurements of only one polarization for both pinhole and channel devices. For channel devices, this polarization is orthogonal to the long axis of the channel. The results of the throughput measurements for channel and pinhole darkfield devices of various aperture sizes will be presented and analyzed in the remaining sections of this chapter.

3.5 Analysis – Throughput: antenna and circuit theory

In order to understand how an NSOM probe works, we will be analyzing its throughput from the perspective of antenna and circuit theory. For example, let us consider the darkfield device shown schematically in Figure 3-7. We can think of the grating to acting as an antenna that captures free-space light and converts it into surface plasmons. The tapered funnel region then acts as a tapered transmission line to transmit the power to the tiny aperture [55], which in turn acts as a tiny antenna radiator. This sub-wavelength electric dipole radiates poorly to the far-field, as one would expect for small antennas [24]. Such antenna concepts can also be found in the literature. For example, even apertureless NSOM can be viewed as a monopole antenna with mirror charges in the substrate [83]. As a result, there are also examples in the literature that combine this with aperture NSOM, by adding a monopole antenna to the end of aperture NSOM probes [113, 114].

Since we did not optimize the grating coupler, and it had a negligible effect on our measurements, we will be focusing on just the last two steps of the above process. Thus, the throughput of the portion of an NSOM probe under consideration consists of the throughput of the tapered region compounded with the radiation efficiency of the small antenna radiator. Since we were unable to numerically calculate the propagation losses in the taper using the mode analysis of Section 3.3.2, and did not attempt to simulate the losses in 3D with COMSOL, we instead estimated the throughput of the taper from the losses predicted by circuit theory, as will be discussed in Section 3.6. Circuit theory is applicable to these devices because they are smaller than the optical wavelength. In order to use circuit theory, we will first introduce the concept of radiation resistance in Section 3.5.1. Since the poor radiation efficiency of the tiny aperture dominates the overall throughput of aperture-based NSOM devices, the remainder of this section will be devoted to analyzing the throughput of the device based on antenna radiation theory.

3.5.1 Analysis – Throughput: dipole radiated power & radiation resistance

We will begin by looking at the power radiated by a Hertzian dipole [115, 116, 117], and then relate it to the concept of radiation resistance. For this analysis, we will consider the aperture at the output of the device as a radiating electric dipole, as shown in Figure 3-19a. If you integrate the Poynting vector produced by an electric dipole with current I, you can obtain an expression for the total power radiated by the electric dipole [115]:

$$P_{rad}(\theta,\varphi) = \frac{\omega^2 a^2 I^2}{32\pi^2 \varepsilon_0 c^3} \int d\varphi \int \sin^3 \theta d\theta$$

$$P_{rad,total} = \frac{\omega^2 a^2 I^2}{32\pi^2 \varepsilon_0 c^3} 2\pi \frac{4}{3} = \frac{\omega^2 a^2}{12\pi \varepsilon_0 c^3} I^2 = \frac{1}{2} R_{rad} I^2$$

$$\Rightarrow R_{rad} = 789 \left(\frac{a}{\lambda} \right)^2 \text{Ohms}$$

where the radiated power has been related to a resistance term using the standard formula from circuit theory for the power dissipated in a resistor. This concept of radiation resistance can then be compared to the ohmic resistance due to material losses, which provides an estimate of the lossy throughput of the structure via circuit theory, as will be discussed in Section 3.6.

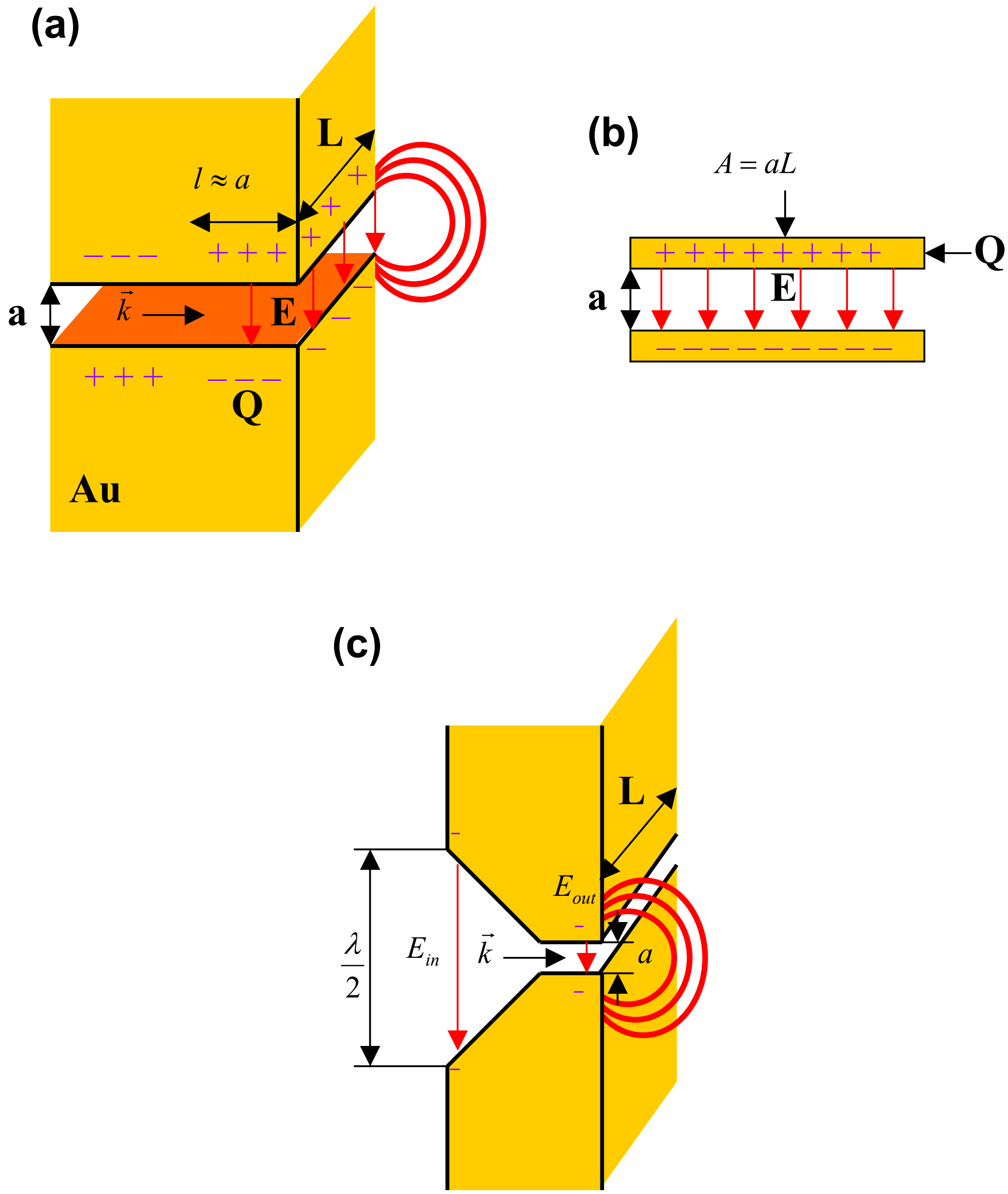

Figure 3-19. Radiating electric dipole models
(a) Model for the electric dipole radiator at the output of an aperture device for modeling the radiated power. (b) Parallel plate capacitor which is equivalent to the output aperture shown in (a). (c) Model for the whole tapered pinhole device for determining the maximum throughput. Radiation from the left excites a $\lambda/2$ electric dipole. The induced voltage propagates down the tapered transmission line to excite the small electric dipole of size a, which radiates into the far-field on the right.

Since the metal in the structure shown in Figure 3-19a prevents it from radiating into one half-space, the power radiated is actually $P_{rad,half} = 1/2 \times P_{rad,total}$. For the measurement described in Section 3.4, we were also unable to collect all of this light, and thus the measured power further depends on the solid angle collected by the detector. As an example of how the solid angle affects the measured power, consider the power radiated into cones with $\theta, \varphi \in [-\pi/12, \pi/12]$ and $\theta, \varphi \in [-\pi/4, \pi/4]$:

$$P_{rad,\pm 15\deg} = 0.0316 \times P_{rad,total} \approx 1/16 \times P_{rad,half}$$

$$P_{rad,\pm 45\deg} = 0.221 \times P_{rad,total} = 0.442 \times P_{rad,half}$$

Thus, given the solid angle collected by the detector, the total power radiated by the electric dipole can be estimated by scaling the measured power by the appropriate constant factor. The exact scaling factor is not critical for a fixed measurements setup, since this only provides a constant scaling factor for the measured results that does not affect the overall trend of the throughput.

The radiated power formula shown above is also commonly given as a function of the dipole moment p of the radiator [117]:

$$P_{rad,total} = \frac{\omega^4}{12\pi\varepsilon_0 c^3}|p|^2 \Rightarrow P_{rad,half} = \frac{1}{2}\frac{\omega^3}{6\varepsilon_0 c^2}\frac{|p|^2}{\lambda}$$

where $p = Qa$. This radiated power formula is equivalent to the one given above for $I = Q\omega$. We will use this dipole form of the radiated power to estimate the far-field throughput of the NSOM probe, since it can be related to the charge in the structure for a physical model, as well as the voltage in the structure for a circuit theory model.

Also, it should be noted that the above formulae for the radiated power from a electric dipole are only valid for a point dipole ($a, L << \lambda$), as would be the case for a small circular pinhole. However, for channel devices, the length of the device L is larger than λ, which gives a different radiation pattern. The power radiated by a channel device is given by:

$$P_{rad,half} = \frac{|p|^2}{L^2}\frac{\omega^2}{8\pi^2\varepsilon_0 c}\int_0^{\pi}\int_{-\frac{\pi}{2}}^{+\frac{\pi}{2}}\left(\frac{\sin^2(kR\sin\theta\sin\varphi)}{\sin^2\varphi}\right)d\varphi\sin\theta d\theta$$

$$\approx \frac{|p|^2}{L^2}\frac{\omega^2}{8\pi^2\varepsilon_0 c}\frac{\pi^2}{4}kL = \frac{1}{2}\frac{\omega^3}{16\varepsilon_0 c^2}\frac{|p|^2}{L}$$

The derivation for this formula is given in Appendix D, which views the output of the channel device as parallel wires that radiate. This derivation was based on the radiation from a large capacitor that is given in reference [118].

3.5.2 Analysis – Throughput: maximum throughput for pinhole device

In this section, we will determine the maximum throughput for a pinhole aperture NSOM device that can be expected when there are no material losses, based on the concepts of circuit and antenna theory. This maximum value can then be used to gauge the measured performance of our darkfield devices. In order to use both circuit and antenna theory for this analysis, we will begin by relating the charges in the radiating electric dipole shown in Figure 3-19a to the corresponding E field and voltage V in the device.

If we consider the geometry shown in Figure 3-19a, we can use Gauss's law on the rectangular prism surface S depicted by the dashed line:

$$\oint_S E \cdot dA = \frac{Q_{enclosed}}{\varepsilon}$$

If we assume that there is no E field flux through the side and bottom surfaces, and we assume that $l \approx a$, we can relate the charge Q to the E field and voltage V:

$$\Rightarrow E \cdot A = E \cdot (l \cdot L) = E \cdot (a \cdot L) = \frac{Q}{\varepsilon} \quad \Rightarrow E = \frac{Q}{\varepsilon a L} \quad \Rightarrow V = \frac{Q}{\varepsilon L}$$

This is equivalent to the parallel plate capacitor shown in Figure 3-19b that has area $A = aL$ and dielectric spacer thickness a. This can be seen from the standard formula for the capacitance C of a capacitor:

$$C = \frac{Q}{V} = \frac{\varepsilon A}{a} = \frac{\varepsilon a L}{a} = \varepsilon L \qquad \Rightarrow V = \frac{Q}{C} = \frac{Q}{\varepsilon L}$$

Now that we can relate the charge Q of a radiating electric dipole to the voltage V of the tapered transmission line that is feeding it, we can analyze the maximum throughput for the tapered aperture device shown in Figure 3-19c, which does not include the effect of having a grating.

For this tapered pinhole device, we assume that plane wave radiation is incident from the left, which excites a λ/2 dipole. The power input to the device is just the product of the field's intensity and the capture cross section of the input λ/2 dipole antenna, which we assume to just be a λ/2 x λ/2 square:

$$P_{in} = \frac{1}{2}\varepsilon_0 c E_{in}^2 \cdot \left(\frac{\lambda}{2}\right)^2$$

This input electric field creates an input voltage at the beginning of the tapered transmission line, which is given by:

$$V_{in} = E_{in} \cdot \frac{\lambda}{2}$$

On the output side, we assume that $L = a$ for a pinhole. The previously derived result from Gauss's law gives the following output voltage:

$$V_{out} = E_{out} \cdot a = \frac{Q_{out}}{\varepsilon_0 a}$$

For this analysis of the maximum throughput, we are assuming that there are no losses down the tapered transmission line. Based on circuit theory, this means that $V_{out} = V_{in}$. This allows us to relate the Q_{out} and p of the radiating electric dipole to the E_{in} of the input light:

$$Q_{out} = \varepsilon_0 a V_{out} = \varepsilon_0 a V_{in} = \varepsilon_0 a\left(E_{in} \cdot \frac{\lambda}{2}\right)$$

$$|p| = Q_{out} \cdot a = \varepsilon_0 a^2 \left(E_{in} \cdot \frac{\lambda}{2} \right)$$

Plugging this dipole moment into the power radiated by a small electric dipole from Section 3.5.1, we have the following as the output power of the device:

$$P_{rad,half} = \frac{1}{2} \cdot \frac{\omega^4}{12\pi\varepsilon_0 c^3} |p|^2 = \frac{2\pi^3 c}{3\varepsilon_0 \lambda^4} |p|^2 \Rightarrow P_{rad,half,\max,pinhole} = \frac{2\pi^3 c\varepsilon_0}{3} \frac{a^4}{\lambda^4} \left(E_{in} \cdot \frac{\lambda}{2} \right)^2$$

The maximum throughput is just the ratio of the output to the input power:

$$\frac{P_{rad,half,\max,pinhole}}{P_{in}} = \frac{4\pi^3}{3} \left(\frac{a}{\lambda} \right)^4 = \frac{1}{12\pi} (ka)^4$$

Since the throughput has a fourth power dependence on the aperture size of the device, it is therefore the most significant factor in determining the throughput of the device besides propagation losses in the taper. This justifies our neglect of the exact taper angle and shape as long as the taper is not long and narrow, as discussed in Section 3.4.

The experimental throughput measured in Section 3.4 for darkfield pinhole devices (light blue) is plotted along with this theoretical lossless maximum throughput (dark blue) in Figure 3-20. This figure also includes an antenna loss version of the theoretical maximum (red) that takes into account the losses for the radiation, using the methods that will be presented in Section 3.6. This lossy curve does not account for the propagation losses in the tapered transmission line. The discrepancy between the experimental and theoretical maximum curves is due to these propagation losses and the coupling efficiency to the taper. As a reference, the throughput of a standard pulled-fiber NSOM probe (brown) is also shown, which has lower throughput because of greater propagation losses.

One should note that the above approximations only hold for $a << \lambda$, since the throughput exceeds unity as $a \rightarrow \lambda$. The above derivation for this fourth power scaling law for the throughput can be summarized as follows:

$$|p| = Qa \qquad P_{rad} \propto \omega^4 |p|^2 \propto \frac{Q^2 a^2}{\lambda^4} \propto \frac{a^4}{\lambda^4}$$
$$Q = \varepsilon_0 a V$$

The same scaling law for the throughput can also be obtained by using the radiation resistance discussed in Section 3.5.1:

$$I = Q\omega \propto \frac{a}{\lambda} \qquad P_{rad} = I^2 R_{rad} \propto (Q\omega)^2 \frac{a^2}{\lambda^2} \propto \frac{a^4}{\lambda^4}$$
$$R_{rad} \propto \frac{a^2}{\lambda^2}$$

This fourth power scaling law for the maximum throughput is not surprising, based on similar scaling laws for the throughput of small holes [67, 68], and for Rayleigh scattering [119], which is the inverse problem. In particular, this result is very close to the transmission t through a small aperture that is presented by Bouwkamp in reference [68]:

$$t \approx \frac{8}{27\pi^2}(ka)^4 \approx 1.132 \times \frac{P_{rad,half,\max,pinhole}}{P_{in}}$$

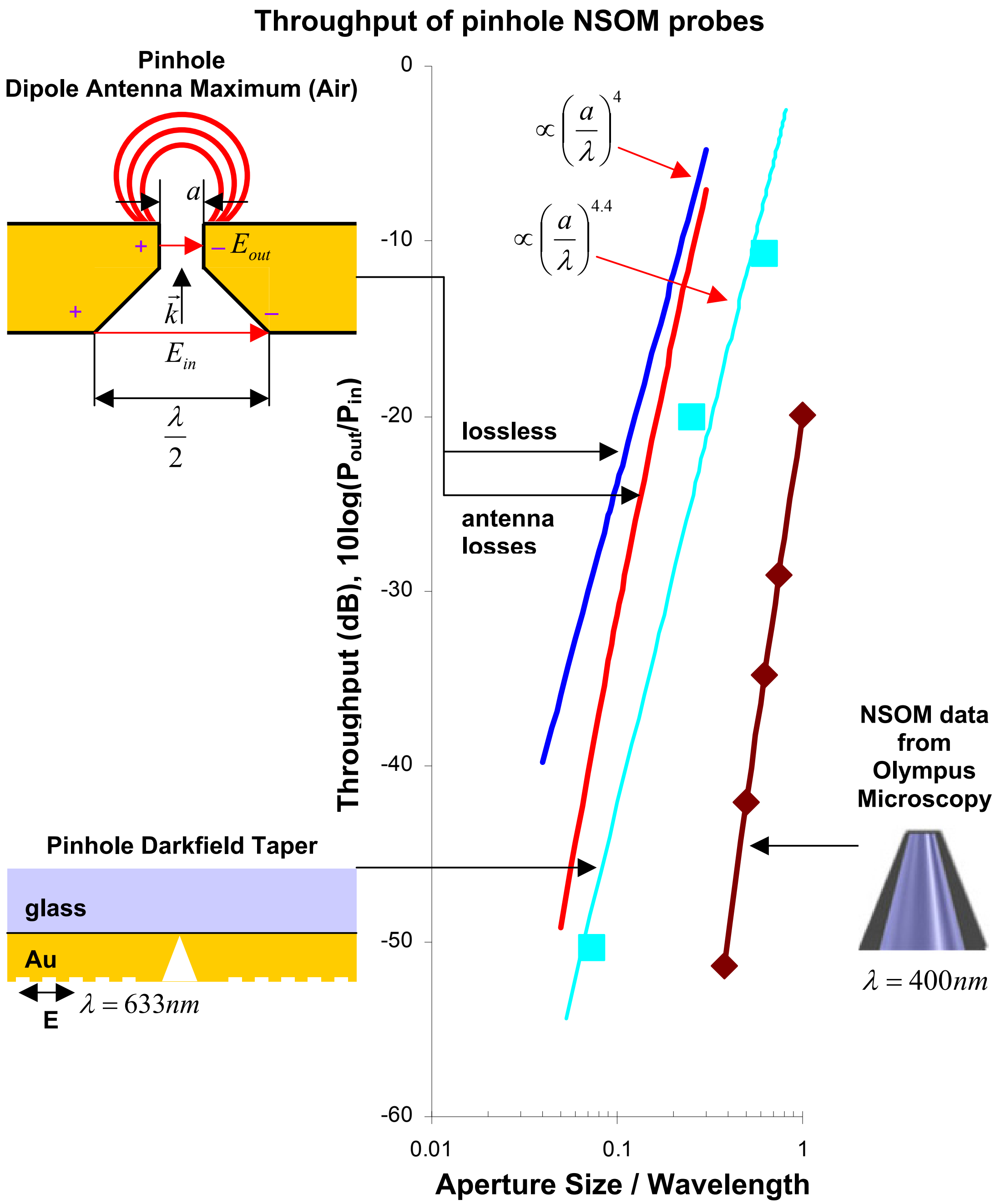

Figure 3-20. Pinhole device throughputs
Throughput of various pinhole NSOM probes: experimentally measured darkfield pinhole device (light blue), theoretical lossless maximum (dark blue), theoretical lossy maximum (red), and standard pulled-fiber NSOM probe (brown).

3.5.3 Analysis – Throughput: maximum throughput for channel device

Next, we will look at the maximum throughput for a channel aperture NSOM device, which can be derived in a similar fashion to that presented in Section 3.5.2 for the pinhole device. For this tapered channel device, we once again assume that plane wave radiation is incident from the left, which excites a λ/2 dipole, as shown in Figure 3-19c. However, since this device has a channel with length L, the power input to the device is incident on an antenna with area λ/2 x L:

$$P_{in} = \frac{1}{2}\varepsilon_0 c E_{in}^2 \cdot \left(\frac{\lambda}{2} \times L\right)$$

The input voltage at the beginning of the tapered transmission line remains the same as for the pinhole case. However, the output voltage now depends on the length of the channel L:

$$V_{out} = E_{out} \cdot a = \frac{Q_{out}}{\varepsilon_0 L}$$

Once again, this allows us to relate the Q_{out} and p of the radiating electric dipole to the E_{in} of the input light:

$$Q_{out} = \varepsilon_0 L V_{out} = \varepsilon_0 L V_{in} = \varepsilon_0 L\left(E_{in} \cdot \frac{\lambda}{2}\right)$$

$$|p| = Q_{out} \cdot a = \varepsilon_0 a L\left(E_{in} \cdot \frac{\lambda}{2}\right)$$

Plugging this dipole moment into the power radiated by parallel wires from Section 3.5.1, we have the following as the output power of the device:

$$P_{rad,half} = \frac{1}{2}\cdot\frac{\omega^3}{16\varepsilon_0 c^2}\frac{|p|^2}{L} = \frac{\pi^3 c}{4\varepsilon_0 \lambda^3 L}|p|^2 \Rightarrow P_{rad,half,\max,channel} = \frac{\pi^3 c\varepsilon_0}{4}\frac{a^2 L}{\lambda^3}\left(E_{in}\cdot\frac{\lambda}{2}\right)^2$$

The maximum throughput is just the ratio of the output to the input power:

$$\frac{P_{rad,half,\max,channel}}{P_{in}} = \frac{\pi^3}{2}\left(\frac{a^2 L}{\lambda^3}\right)\times\left(\frac{\lambda/2}{L}\right) = \frac{\pi^3}{4}\left(\frac{a}{\lambda}\right)^2$$

Thus, the throughput of a channel device scales as the square of the aperture size rather than the fourth power. The experimental throughput measured in Section 3.4 for darkfield channel devices (light blue) is plotted along with this theoretical lossless maximum throughput (dark blue) in Figure 3-21. This figure also includes an antenna loss version of the theoretical maximum (red) that takes into account the losses for the radiation, using the methods that will be presented in Section 3.6. As with the pinhole case, this lossy curve does not account for the propagation losses in the tapered transmission line. Again, the discrepancy between the experimental and theoretical maximum curves is due to these propagation losses and the coupling efficiency to the taper.

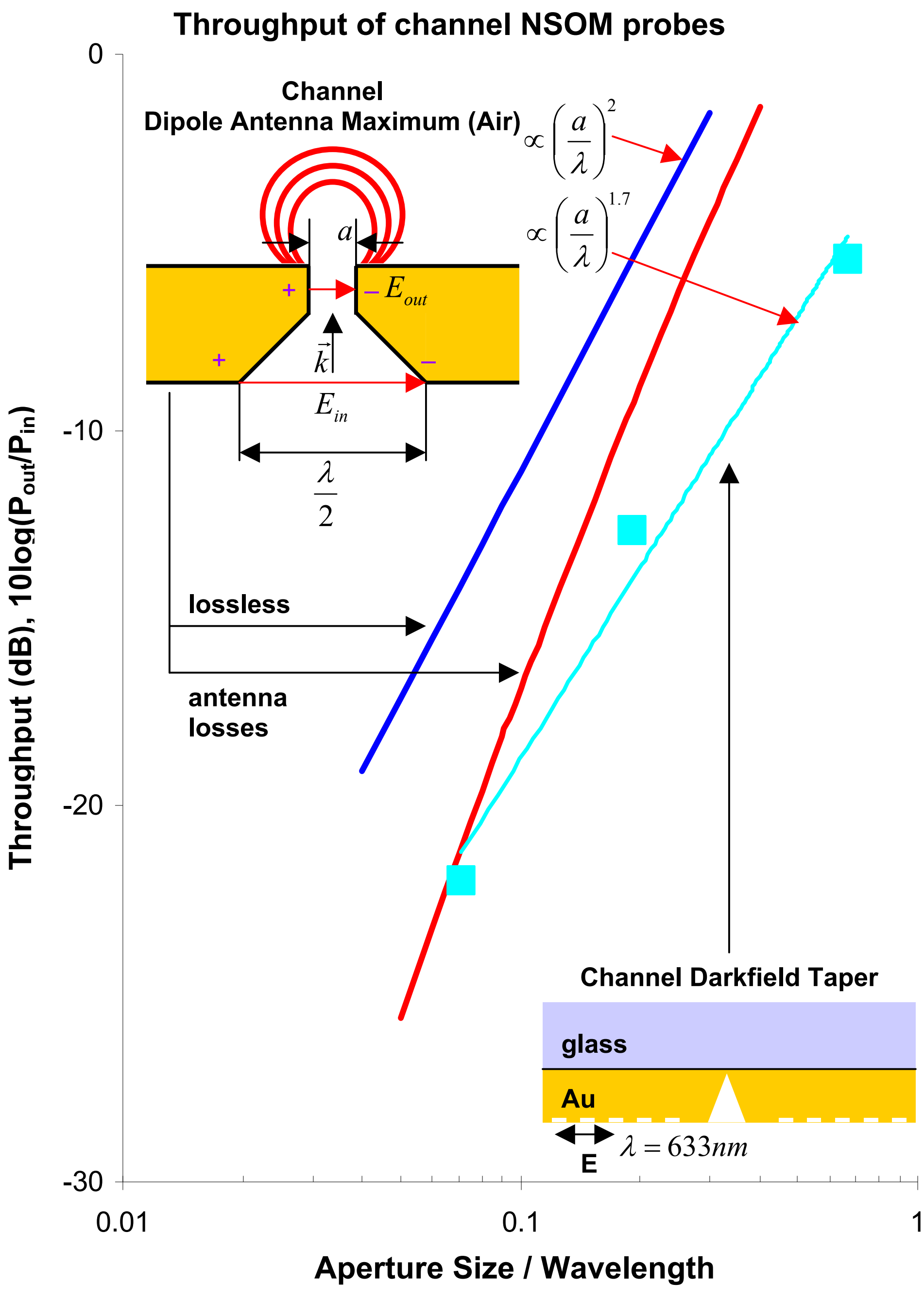

Figure 3-21. Channel device throughputs
Throughput of various channel NSOM probes: experimentally measured darkfield channel device (light blue), theoretical lossless maximum (dark blue), and theoretical lossy maximum (red).

3.6 Analysis – Throughput: losses

There are several mechanisms that could contribute to the losses in the darkfield structure shown in Figure 3-19c. Theses losses can be broken down into the three regions of the device: the input, the tapered transmission line, and the output. This section will look at these various loss mechanisms and introduce ways to estimate the effects of these losses.

3.6.1 Analysis – Losses: loss mechanisms

First, there are losses for coupling to the electric dipole on the input side. However, we will continue to assume that an opening larger than λ/2 will be able to capture at least the power incident on a half-wave dipole. Additionally, a well-designed grating would help to capture even more input power for the device, possibly improving its performance. However, including a grating would complicate the analysis since one would also need to consider grating efficiency as well as the coupling efficiency simulated in Section 3.3.3. Thus, further optimization of the input performance of the device is outside the scope of this dissertation.

Second, there will be propagation losses within the tapered transmission line region of the pinhole or channel. For a channel device, the taper could have as low as 3 dB of loss [55]. For a pinhole device, the imaginary part α of the complex propagation constant $k_z = \beta + i\alpha$ for the modes of the waveguide could be used to determine the propagation losses using, as will be discussed in Section 3.6.4. However, the numerical mode analysis for the pinhole case is difficult, as was discussed in Section 3.3.2. Although we could use FEM simulation like in reference [55] to determine the losses (except in 3D rather than in 2D), we instead choose to use circuit theory to determine the resistive losses in the tapered transmission line. The resistance in the taper can also be related back to α, the imaginary part of the propagation constant. This analysis neglects the reflection losses, which are analogous to an impedance mismatch in the transmission line, since the taper angle is fairly shallow. Also, there may be additional losses in the transmission line if there are flat regions on either side of the taper; a long narrow waveguide at the tip of the taper would introduce significant losses. However, for the purpose of this analysis, we will only consider the taper portion of the transmission line, since the losses in any additional regions of the transmission line can be analyzed based on their resistances in a similar fashion.

Finally, the device will also have losses during the radiation process of the electric dipole at the output aperture. This is the loss that is factored into the lossy maximum throughputs (red) shown in Figure 3-20 and Figure 3-21. We will begin by considering this loss in terms of circuit theory. The resulting concepts can then be applied to the propagation losses in the tapered transmission line.

3.6.2 Analysis – Losses: sheet resistance in a waveguide

In order to estimate the resistive metal losses in a waveguide, we will be using the following formula for the sheet resistance in the metal boundaries of the pinhole waveguide, which is taken from Jackson [49]:

$$R = \frac{2}{\sigma\delta}$$

where σ is the conductivity of the metal and δ is the skin depth of the metal at the frequency of operation. This resistance represents the ohmic resistance in the walls of a waveguide due to the currents induced by the optical fields. A summary of the derivation for this resistance from reference [49] can be found in Appendix E.

This formula can be understood physically by considering the geometry shown in Figure 3-22a, which shows a size L x L portion of the waveguide. Since the current only penetrates into the metal a distance on the order of the skin depth δ, we can consider this piece of the waveguide to be a wire of cross section δ by L. If we assume that the current in the surface traverses a distance 2*L each cycle, we can take 2*L to be the length of this wire. Then, using the standard formula for the resistance of a wire on this piece of the waveguide, the resistance (which is actually a sheet resistance, since it is for a L x L area) is:

$$\begin{aligned}\text{Ohmic Resistance} &= \frac{\text{resistivity} \times \text{length}}{\text{area}} \\ &= \frac{\text{resistivity} \times 2L}{L \times \text{skin depth}} = \frac{2 \times \text{resistivity}}{\text{skin depth}}\end{aligned}$$

This ohmic resistance from the physical model is equivalent to the one from Jackson.

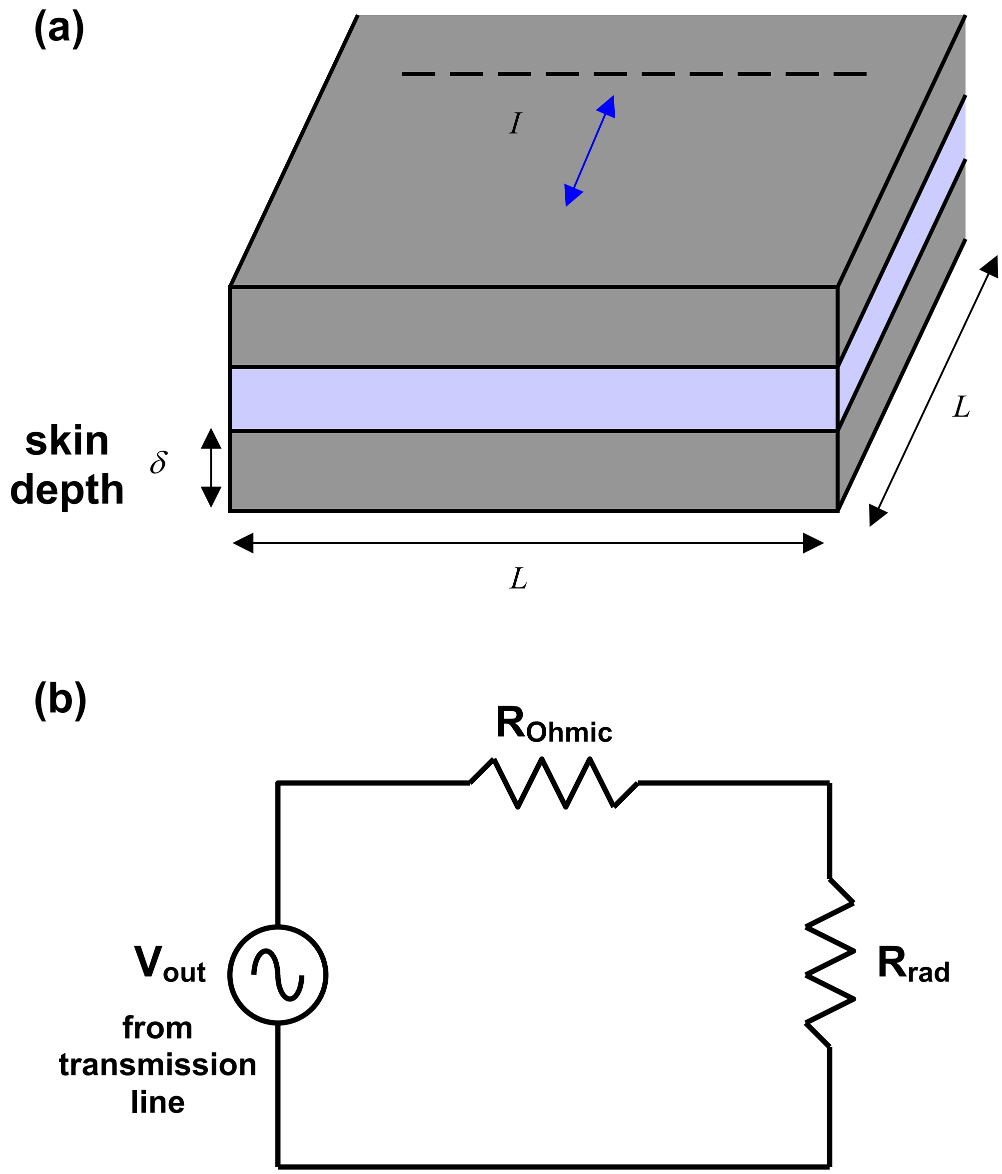

Figure 3-22. Ohmic resistance: physical model and circuit diagram
(a) Physical model for the sheet resistance in the metallic boundaries of a waveguide. (b) Circuit diagram for determining the radiation efficiency based on the ohmic and radiation resistances.

From this physical model, we can see that the thickness of the conducting layer in the boundaries of the waveguide depends on the skin depth. Thus, it may actually be more appropriate to use the surface plasmon's penetration into the metal as the thickness of the conducting layer in the boundary, since this penetration changes with the k-vector of the plasmonic modes. If the mode has a large k-vector, it would have a small penetration depth, which increases the resistance in the boundaries. However, since it is not clear what the magnitude of the k-vector is, we will neglect this effect in our analysis. Instead, we will use the skin depth from free space light impinging on a metal surface.

For Au at a wavelength of 633 nm, the optical dielectric constant is $\varepsilon_m = -11.455 + 1.232i$ [61]. The resistivity at optical frequencies can be determined from the dielectric constant as follows [55]:

$$\rho_{AC} = \mathrm{Re}\left\{\frac{1}{\sigma}\right\} = \mathrm{Re}\left\{\frac{1}{j\omega\varepsilon_0\left(1-\varepsilon_m(\omega)\right)}\right\} = 2.98\times10^{-7}\,\Omega\cdot\mathrm{m} \approx 13\times\rho_{DC}$$

As a reference, the optical AC conductivity is compared to the DC conductivity of Au at room temperature, $\rho_{DC} = 2.21\times10^{-8}\,\Omega\cdot\mathrm{m}$ [120]. The skin depth can be determined using the above optical conductivity [49], which gives a skin depth of $\delta = 30\,\mathrm{nm}$ for normal incidence on a Au film. Combining the above resistivity and skin depth gives an AC ohmic sheet resistance of:

$$R_{Ohmic} = \frac{2\rho_{AC}}{\delta} = 19.9\Omega$$

3.6.3 Analysis – Losses: antenna efficiency

Next, we can use circuit theory to model how this ohmic resistance affects the antenna efficiency of the electric dipole radiator discussed in Section 3.5.2. Using the radiation resistance from Section 3.5.1, we can create a circuit diagram for the antenna, as shown in Figure 3-22b. As you can see, this creates a voltage divider between the ohmic resistance and the radiation resistance, and thus the radiation efficiency is:

$$\eta = \frac{R_{rad}}{R_{rad} + R_{Ohmic}}$$

As an example, if we calculate the radiation resistance for various aperture sizes, we can obtain the following radiation efficiencies:

$$\begin{array}{lll}
\text{pinhole size} = 100\text{ nm} & \Rightarrow R_{rad} = 19.7\Omega & \Rightarrow \eta = 49.7\% \\
\text{pinhole size} = 50\text{ nm} & \Rightarrow R_{rad} = 4.92\Omega & \Rightarrow \eta = 19.8\% \\
\text{pinhole size} = 10\text{ nm} & \Rightarrow R_{rad} = 0.197\Omega & \Rightarrow \eta = 0.98\%
\end{array}$$

This example shows that since the radiation resistance decreases drastically with the size of the pinhole, this also greatly decreases the radiation efficiency since the ohmic resistance is constant for a square aperture. A similar analysis can also be done for channel devices. This radiation efficiency decreases the lossless throughput derived in Sections 3.5.2 and 3.5.3, which gives us the lossy throughput that is plotted in Figure 3-20 and Figure 3-21 (red).

3.6.4 Analysis – Losses: power attenuation from resistive losses

The ohmic resistance R_{Ohmic} can also be related to α, the imaginary part of the propagation constant, as a function of the z position along the waveguide, using the following approximation based on a square waveguide of size a [49]:

$$\alpha(z) \approx \frac{2R_{Ohmic}}{Z_0}\frac{1}{a(z)} \approx \frac{0.106}{a(z)}$$

where $Z_0 \equiv \sqrt{\mu_0/\varepsilon_0} \approx 377\,\text{Ohms}$ is the impedance of free space. We have also assumed that $R_{Ohmic} \approx 20\,\text{Ohms}$ in the Au material system and that it is independent of position for a constant skin depth of $\delta = 30\,\text{nm}$.

If we let z = 0 be the beginning of the waveguide, this α can then be used to determine the decay in power due to propagation losses, relative to the initial power P_0, using the following equation [121]:

$$P(z) = P(z_0)e^{-2\int_{z_0}^{z}\alpha(z)dz} = P_0 e^{-2\int_0^z \alpha(z)dz}$$

For a tapered waveguide with input aperture size a_0, output aperture size a, and film thickness t, we will assume a linear change in the profile:

$$a(z) = \frac{a-a_0}{t}z + a_0 \Rightarrow da = \frac{a-a_0}{t}dz$$

$$\Rightarrow 2\int_0^t \alpha(z)dz \approx 0.212\int_0^t \frac{1}{a(z)}dz = 0.212\frac{t}{a-a_0}\int_{a_0}^{a}\frac{1}{a}da = 0.212\frac{t}{a-a_0}\ln\frac{a}{a_0}$$

Plugging this into the power decay equation, we have the following power throughput or transmittance:

$$T \equiv \frac{P(t)}{P_0} = e^{-0.212\frac{t}{a-a_0}\ln\frac{a}{a_0}} = \left(\frac{a}{a_0}\right)^{0.212\frac{t}{a_0-a}}$$

This confirms our expectation that the throughput decays exponentially in the length of the waveguide (i.e. thickness of the film).

As an example, let us consider a darkfield pinhole device that has an input size $a_0 = \lambda/2 \approx 316\,\text{nm}$ and film thickness $t = 300\,\text{nm}$. This gives the following power throughputs or transmittances T for various pinhole sizes a:

$$\begin{aligned}
&\text{pinhole size} = 100\,\text{nm} && \Rightarrow T = 0.713 \\
&\text{pinhole size} = 50\,\text{nm} && \Rightarrow T = 0.644 \\
&\text{pinhole size} = 10\,\text{nm} && \Rightarrow T = 0.488
\end{aligned}$$

The corresponding taper angles for these geometries are around 40°, since they do not account for the curvature at the input surface. However, the results are still similar to the previously mentioned results for the tapered slab geometry from reference [55], which can have as low as 3 dB of losses in the tapered region. A similar method can also be used to analyze the losses in straight channel regions on either side of the tapered region.

3.7 Analysis – Alternative figures of merit

For the measurements of the darkfield devices discussed in Section 3.4 and of the NSOM structures reported in the literature, far-field throughput is the figure of merit that is used to compare the performance of structures with varying aperture sizes. One reason for using far-field throughput as the point of comparison is because it is easily measured. However, it is difficult to meaningfully compare the far-field throughput of devices with different geometries, since the magnitude of the far-field throughput is dominated by the radiation from the small antenna at the output aperture, which scales as $(a/\lambda)^4$. A high throughput may actually be an indicator of having a good antenna at the output rather than having low losses in the device itself. One example of this effect from the literature is where a grating coupler was added to the output side of a channel device to improve its directionality [59].

Since the ultimate purpose of these devices is to be used as near-field probes, a near-field figure of merit would actually be more appropriate. For example, one might want to compare the strength and/or size distribution of the E field at the output instead. This type of figure of merit would also allow one to compare the performance of a device to the limitations of the material system, such as damage from exceeding the breakdown voltage or from resistive heating. There are also other potential figures of merit which can be derived from the E field, as will be described later in Section 3.7.1. Although it is possible to estimate the E field strength based on the throughput, it requires an accurate model of the dipole size and distribution at the output. Using this model, one could then determine the device's theoretical maximum throughput based on radiated power considerations, similar to what was done for the simple pinhole and channel geometries discussed in Sections 3.5.2 and 3.5.3. For example, if one measures the far-field radiated power $P_{rad,\pm 45^\circ}$ of a pinhole over a solid angle of ±45°, one could work backwards using the formulae in Section 3.5.2 to determine the E field at the output and any related figures of merit F as follows:

$$P_{rad,\pm 45^\circ} \Rightarrow P_{rad,half,measured} \Rightarrow |p| \Rightarrow Q_{out} \Rightarrow E_{out} \Rightarrow F$$

3.7.1 Analysis – Figures of merit: definitions

There are several additional interesting figures of merit that can be derived from the E field, which can be estimated from the throughput as described above. The first is the effective focus size, which is based on the figure of merit presented by Conway in reference [55]. Conway's figure of merit and the effective focus size for the geometry shown in Figure 3-19a are defined as follows:

$$F_{Conway}[\frac{1}{m^2}] \equiv \frac{c\varepsilon\left|E_{\max}\right|^2}{P_{in}} \equiv \frac{1}{(\text{effective focus size})^2} \Rightarrow F_{size}[m] \equiv \frac{1}{\sqrt{F_{Conway}}}$$

For free-space electromagnetic radiation, the minimum F_{size} would simply be the focus size due to the diffraction limit. Thus, a smaller focus size indicates that the E field is stronger that that produced by the diffraction limit.

For the constant voltage transmission line described in Section 3.5.2, smaller gaps are expected to have higher E fields. Thus, in order to compare the effectiveness of structures with varying aperture sizes, another useful figure of merit is to compare the above effective focus size with the actual size a of the device:

$$F_{ratio} \equiv \frac{a}{F_{size}} \equiv a\sqrt{F_{Conway}}$$

A large value for this dimensionless focusing ratio indicates that the device focuses well for its given size.

3.7.2 Analysis – Figures of merit: optimal values

In this section, we will look at the optimal (maximum/minimum) values for the figures of merit defined in Section 3.7.1 for the tapered geometry shown in Figure 3-19c. To determine these values, we will use methods similar to those of the derivations for the maximum throughputs discussed in Sections 3.5.2 and 3.5.3. We will then compare the calculated figures of merit for our experimental results to these optimal values.

For a pinhole device ($L = a$), we have the following expressions for the power input to a λ/2 x λ/2 antenna and for the maximum output E field:

$$P_{in} = \frac{1}{2}\varepsilon_0 c E_{in}^2 \cdot \left(\frac{\lambda}{2}\right)^2 \qquad\qquad E_{out} = \frac{V_{out}}{a} = \frac{V_{in}}{a} = E_{in} \cdot \frac{\lambda}{2} \cdot \frac{1}{a}$$

We can use these expressions to derive the following optimal figures of merit:

$$F_{Conway,pinhole,\max} = \frac{c\varepsilon\left|E_{in}\right|^2 \cdot \left(\frac{\lambda}{2}\right)^2 \cdot \frac{1}{a^2}}{\frac{1}{2}c\varepsilon_0\left|E_{in}\right|^2 \cdot \left(\frac{\lambda}{2}\right)^2} = \frac{2\varepsilon_r}{a^2}$$

$$\Rightarrow F_{size,pinhole,\min} = \frac{a}{\sqrt{2\varepsilon_r}} \qquad\qquad \Rightarrow F_{ratio,pinhole,\max} = \sqrt{2\varepsilon_r}$$

For a channel device (L > λ), we have a similar expression for the power input to a λ/2 x L antenna:

$$P_{in} = \frac{1}{2}\varepsilon_0 c E_{in}^2 \cdot \left(\frac{\lambda}{2} \times L\right)$$

and the same expression for the maximum output E field as for the pinhole case. This gives the following optimal figures of merit:

$$F_{Conway,channel,\max} = \frac{c\varepsilon\left|E_{in}\right|^2 \cdot \left(\frac{\lambda}{2}\right)^2 \cdot \frac{1}{a^2}}{\frac{1}{2}c\varepsilon_0\left|E_{in}\right|^2 \cdot \left(\frac{\lambda}{2}\times L\right)} = \frac{2\varepsilon_r}{a^2}\times\frac{\lambda/2}{L}$$

$$\Rightarrow F_{size,channel,\min} = \frac{a}{\sqrt{2\varepsilon_r}}\times\sqrt{\frac{L}{\lambda/2}} \qquad \Rightarrow F_{ratio,channel,\max} = \sqrt{\varepsilon_r\times\frac{\lambda}{L}}$$

The focusing ratio for the experimental results for the darkfield pinhole and channel devices are plotted relative to their corresponding optimal values in Figure 3-23 and Figure 3-24, respectively. The deviation of the experimental focusing ratio from the maximum values is likely due to the losses discussed in Section 3.6, similar to the throughput results shown in Figure 3-20 and Figure 3-21.

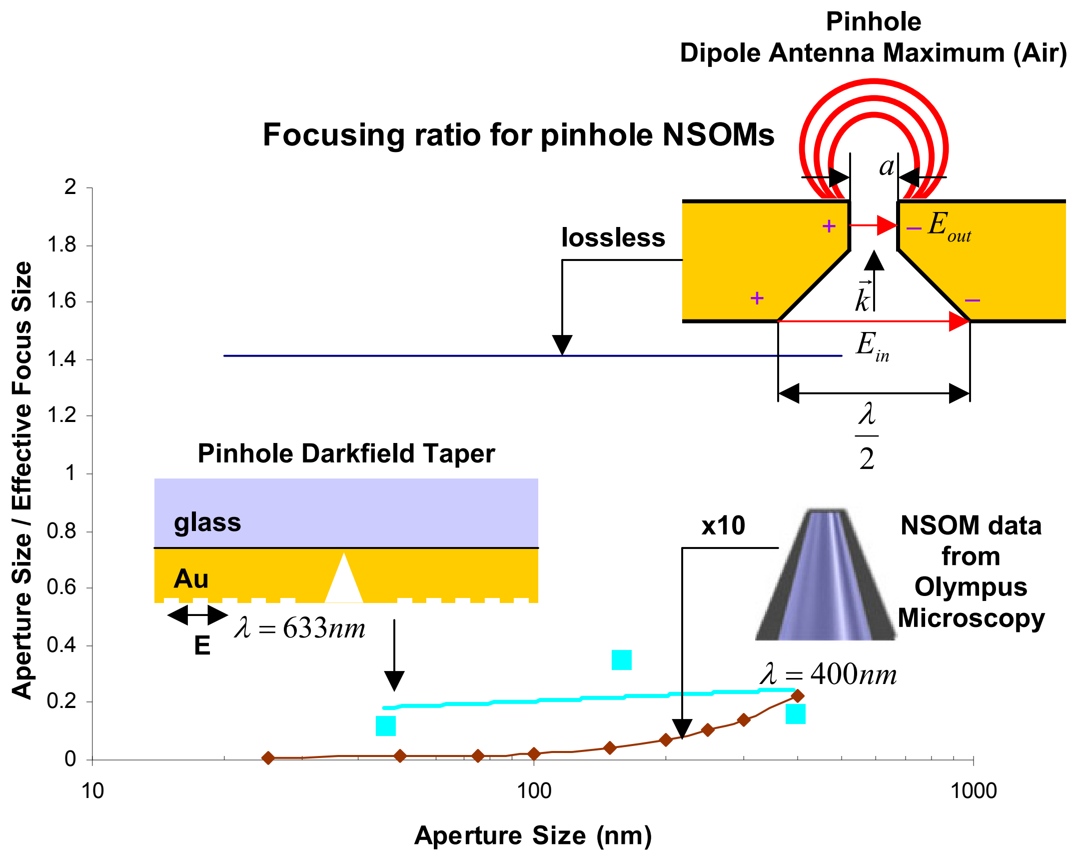

Figure 3-23. Pinhole device focusing ratios
Plot of the focusing ratio figure of merit that is calculated for various pinhole NSOM probes: experimentally measured darkfield pinhole device (light blue), theoretical lossless maximum (dark blue), and standard pulled-fiber NSOM probe, multiplied by 10 (brown).

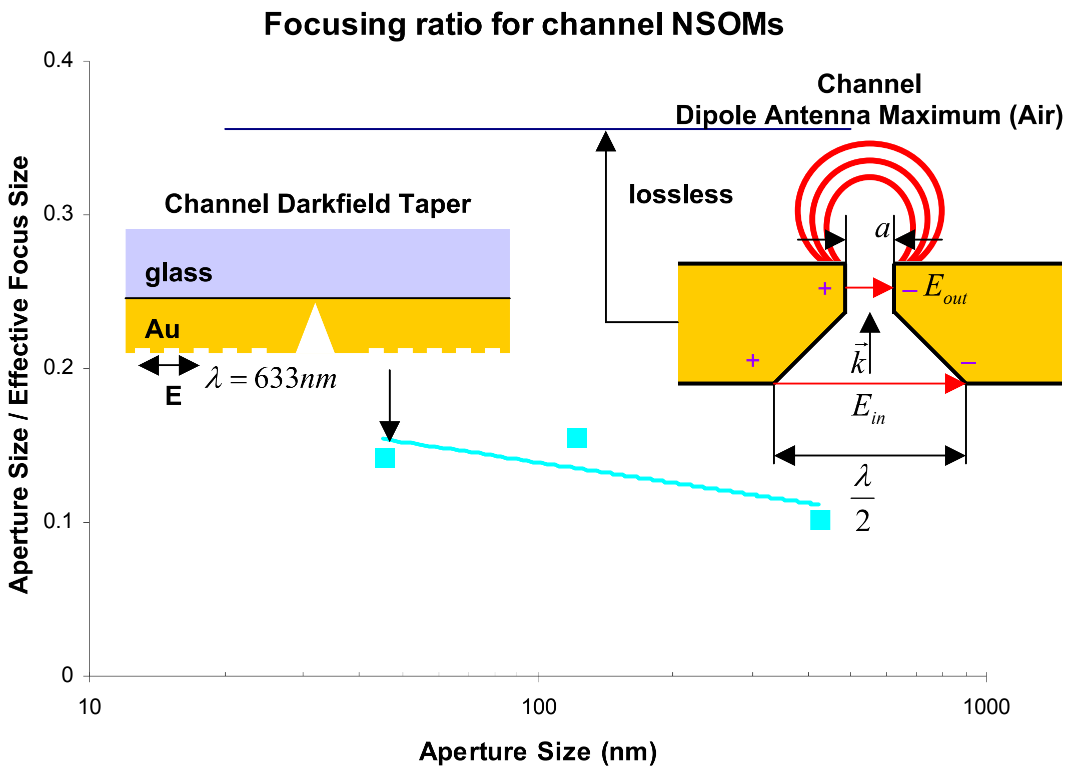

Figure 3-24. Channel device focusing ratios
Plot of the focusing ratio figure of merit that is calculated for various channel NSOM probes: experimentally measured darkfield channel device (light blue) and theoretical lossless maximum (dark blue).

3.8 Conclusion

In summary, this chapter has investigated darkfield taper structures that improve upon the background light limitations of the plasmonic dimple lens presented previously in Chapter 2. The tapered pinhole and channel devices were designed using FEM simulation and mode analysis. The devices were fabricated using FIB milling, and the device performances were determined by measuring the far-field throughput of the devices. The throughput results were interpreted using antenna theory to understand the $(a/\lambda)^4$ dependence of the far-field throughput for pinhole devices. Device losses were also estimated using circuit theory analysis.

In order to have a darkfield device for an NSOM probe, the device must have a small aperture in a metal film, as discussed in Section 3.2. Due to the losses in the cylindrical waveguide of the aperture, the dielectric inside the aperture can be tapered to limit propagation losses. Finally, a grating coupler can be used to capture more power to input to the tapered waveguide. These features are combined in the darkfield taper structure shown in Figure 3-7. In order to make this device compatible with current fiber-based NSOM probes, one could fabricate it at the end of a fiber, as shown in Figure 3-25. This method is similar to the work described in reference [122].

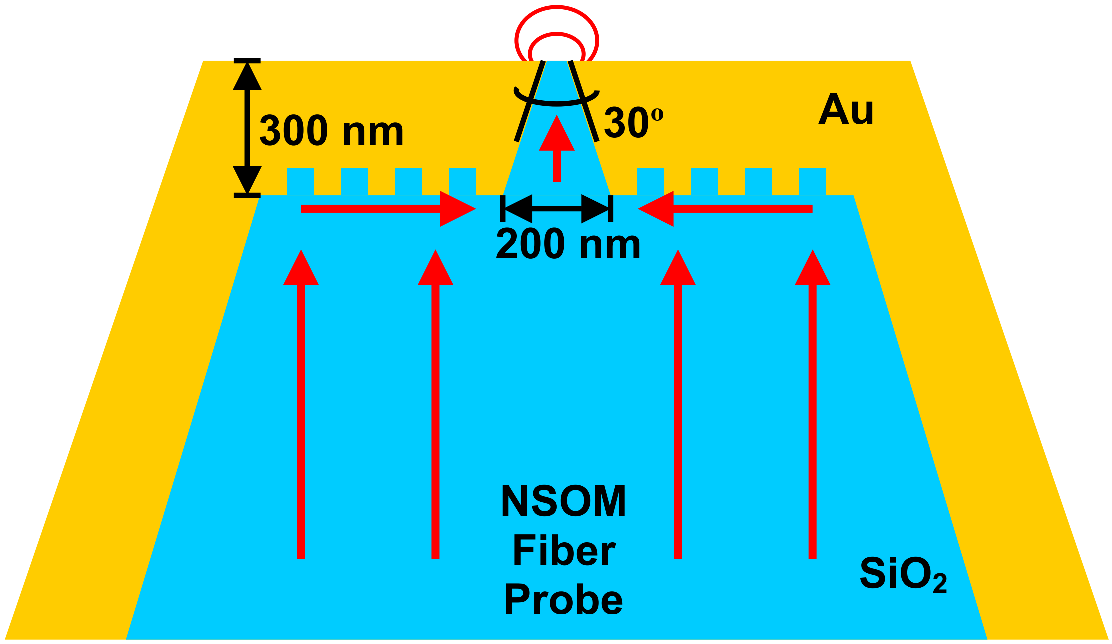

Figure 3-25. NSOM fiber probe with darkfield plasmonic lens
Schematic of a darkfield plasmonic lens integrated onto the end of a fiber-based NSOM probe.

As was discussed in Section 3.7, far-field throughput was compared because it is easily measured. However, since these devices are intended for use as near-field probes, comparing near-field figures of merit is more appropriate than comparing their far-field throughputs for these devices. Although there are ways to estimate the near-field figures of merit related to the E field strength using the far-field throughput measurements, a direct measurement method, such as the near-field measurement schemes shown in Figure 3-12, might be more desirable. Since these types of measurements would greatly increase the complexity of the fabrication process, they were not pursued in this work.

Chapter 4 – Conclusion

In conclusion, this dissertation has presented two tapered devices for focusing optical energy to the nanoscale. In Chapter 2, we discussed the design, fabrication, and measurement of the plasmonic dimple lens structure. The experimental measurements of the optical output of this device demonstrated that this dimple lens structure is able to focus beyond the diffraction limit. However, we were limited in our assessment of the actual resolution of the device by the aperture size of the pulled-fiber probe used in the NSOM measurement system. A higher resolution measurement of the plasmonic dimple lens would require a different measurement technique, such as by using an apertureless NSOM system. Although the presence of extraneous background light in this device makes it ill-suited for certain applications, the final edge-polishing step in the fabrication of the plasmonic dimple lens makes it particularly well-suited for the application of HAMR.

In Chapter 3, we discussed the darkfield plasmonic funnel device. We presented this device as a solution for the background light problem of the plasmonic dimple lens. Based on the insights about tapered structures from the dimple lens design, the tapered funnel device can also be seen as an improvement upon existing bullseye structures by decreasing losses within the pinhole. Using simulation and mode analysis, we determined the design parameters for the shape of this funnel device. Tapered pinhole and channel devices with varying aperture sizes were then fabricated using FIB milling, and the far-field throughputs of each device were measured.

These far-field throughputs were then analyzed using antenna theory. This analysis provides an explanation for their low throughput, since we expect the radiation from pinhole devices to have a $(a/\lambda)^4$ dependence on the aperture size a. Due to the difficulty of measuring or determining the various losses in the system, we instead used circuit theory to estimate the losses. This circuit theory loss analysis once again emphasizes the importance of having a tapered structure to minimize losses in the device. The combination of the propagation losses in the taper and the poor radiation from the aperture gives us a new understanding of the low throughput of these devices. Thus, these antenna and circuit theory concepts could provide an alternative approach to the design of near-field focusing structures, as well as other optical devices at the nanoscale. Additionally, further work can also be done to investigate the losses for the input stage of the darkfield device. For example, one might want to determine the effectiveness of and optimal parameters for incorporating an in-coupling grating into the device.

However, since these devices are meant for near-field measurements, far-field throughputs are not an ideal metric for comparing these devices. Although we have proposed a way of estimating the near-field performance of these devices, a near-field measurement would be the best way to compare device performances. This type of measurement was not performed due to increased fabrication and measurement complexity. Despite the fact that the near-field profile of the darkfield device was not measured, the design and analysis of this device have shown that it should provide a low background, higher resolution, and higher throughput alternative probe structure for NSOM when compared to existing probe types, such as pulled-fiber probes.

Appendix A – Plasmonic Dimple Lens Fabrication Process Flow

March 7, 2007

1) Begin with a 300μm DSP 4” wafer

2) **LPCVD Nitride** (multiple wafers)
   - **PFC** – 10min etch in 100^oC piranha, DI rinse, Verteq spin dry
   - **Deposit** 90sec LPCVD nitride in furnace

3) **Cut** wafer into (9) squares ~1.5 to 2cm on a side

4) **Au Island Patterning**
   - **Clean** – Sonicate in acetone 10sec, solvent (acetone/methanol/IPA), DI, N_2 blow dry
   - **Bake** on R hotplate @ 150^oC for 5min
   - **Ash** 5min in Tegal, $\mathbf{N_2}$ blow dust just before spinning
   - **Spin** AZ5214 @ 3k for 30sec (500rpm for 5sec ramp) on R spinner
   - **Bake** PR @ 110^oC for 90sec on L most hotplate, N_2 before each exposure
   - **Expose** pattern #4 of 09/27/2006 mask for 10sec @ 8.0mW on Suss 2
   - **Develop** for 30sec in 1:4 AZ400K:DI H_2O (~20:80mL), rinse in DI H_2O (may need to refresh developer after half of pieces)
   - Check patterns in microscope

5) **Au Island Deposition** (9 pieces)
   - **Ash** 5min in Tegal
   - **Evaporate** 100nm Au @ 3Å/s in Sloan
   - **Soak** in acetone overnight (e.g. 6 hours)
   - **Liftoff** - Poke edges/sonicate if needed, solvent rinse after liftoff
   - **Rinse** well in DI H_2O (change H_2O every few pieces), N_2 medium blow dry
   - Inspect in microscope

6) **PECVD Nitride** (9 pieces)
   - **Deposit** 300nm SiN using “cal” recipe (15 min) in STS PECVD
   - **Inspect** for bubbles in islands

7) **Cut** glass into ~ 2cm x 2cm pieces (larger than Si pieces)
   - **Inscribe** each piece with a different # (dirty/down side)
   - **Clean** - Sonicate, solvent, water, N_2, 5min ash in Tegal

8) **Glass bonding**
   - Squeeze out necessary amount of Optocast onto piece of foil (return tube to fridge as soon as possible)
   - **Apply** Optocast to Si pieces using a cleaned razor, spread evenly
   - Place glass on top of optocast, clean side down, force air bubbles out by applying pressure from center outwards
   - Keep applying pressure until Au pattern is uniformly visible, and further pressure causes voids that appear (then disappear)
   - Wipe excess epoxy w/ q-tip (especially from glass side)
   - **Cure** on hotplate for 2hrs @ 110^oC

- **Scrape** excess cured epoxy w/ razor (especially from outer glass/Si surfaces)

9) **Bulk Si Removal 1** (3 pieces)
- N_2 blow off scrapings
- Apply cool grease to glass side and paste each piece onto carrier nitride/oxide 4" wafer, move piece(s) around to spread uniformly
- **Etch** 35min in new DRIE using "Fast Nano" recipe (30min for <3 pieces) (central region should not be exposed)
- **Remove** from carrier wafer using methanol, wiping, solvent clean

10) **Bulk Si Removal 2**
- Place samples in DI H_2O
- Prepare 1:1 HF:HNO_3 (100mL:100mL, measure HNO_3 first, stir)
- Remove sample from H_2O, get a good grip, then dip each piece in new 100mL etch until all Si is removed (~20sec), maintaining level-ness and stirring
- Place back in DI H_2O to rinse, N_2 blow dry, inspect for Si islands

11) ***E-beam** for Grating

12) **Au Grating Deposition**
- **Evaporate** 30nm Au @ 3Å/s in Sloan
- **Soak** 2hrs in acetone, 1hr warm (120^{o}C hotplate, stirred) acetone (cracks appear if soak too long in cold acetone)
- **Liftoff** - Poke edges/sonicate up to 1min, solvent, DI H_2O rinse after liftoff, gentle N_2
- Inspect in microscope/AFM

13) ***E-beam** for Dimple, AFM

14) **Evaporate** upper 100nm Au @ 3Å/s in Sloan

15) ***E-beam** for SU-8

16) **Etch** upper Au in Oxford for 3min 45sec using "Agetch" recipe

17) **Bond** to glass using Norland 81
- **Cure** under UV lamp for 2hrs
- **Age** on hotplate for 12 hrs at 50^{o}C

18) Edge ***Polish**

Appendix B – Metamaterials

Metamaterials have many interesting properties, including that they can be considered to have high effective refractive indexes [28]. These metamaterials, consisting of alternating thin layers of metal and dielectric, can also have anisotropic effective dielectric constants, which result in hyperbolic dispersion equations [93, 94]. Based on this effect, one type of lens that these references propose is a cylindrical 'hyperlens' for converting light spots spaced closer than the diffraction limit into spots that can be resolved in the far-field. This type of lens has also been demonstrated experimentally in reference [95].

Similarly, one could use these lenses in reverse to focus light to smaller than a diffraction-limited spot. One drawback of these cylindrical lenses is that they work on curved surfaces. One solution to this is presented in Figure B-1a, where layers of variable thickness are used to separate the light spots by guiding them from a flat input surface to a curved expansion region and back to a flat output surface. This effect can also be used in other ways to guide light, such as in the 'waveguide' structure shown in Figure B-1b that maintains the sub-diffraction size and separation of the light spots within the waveguide.

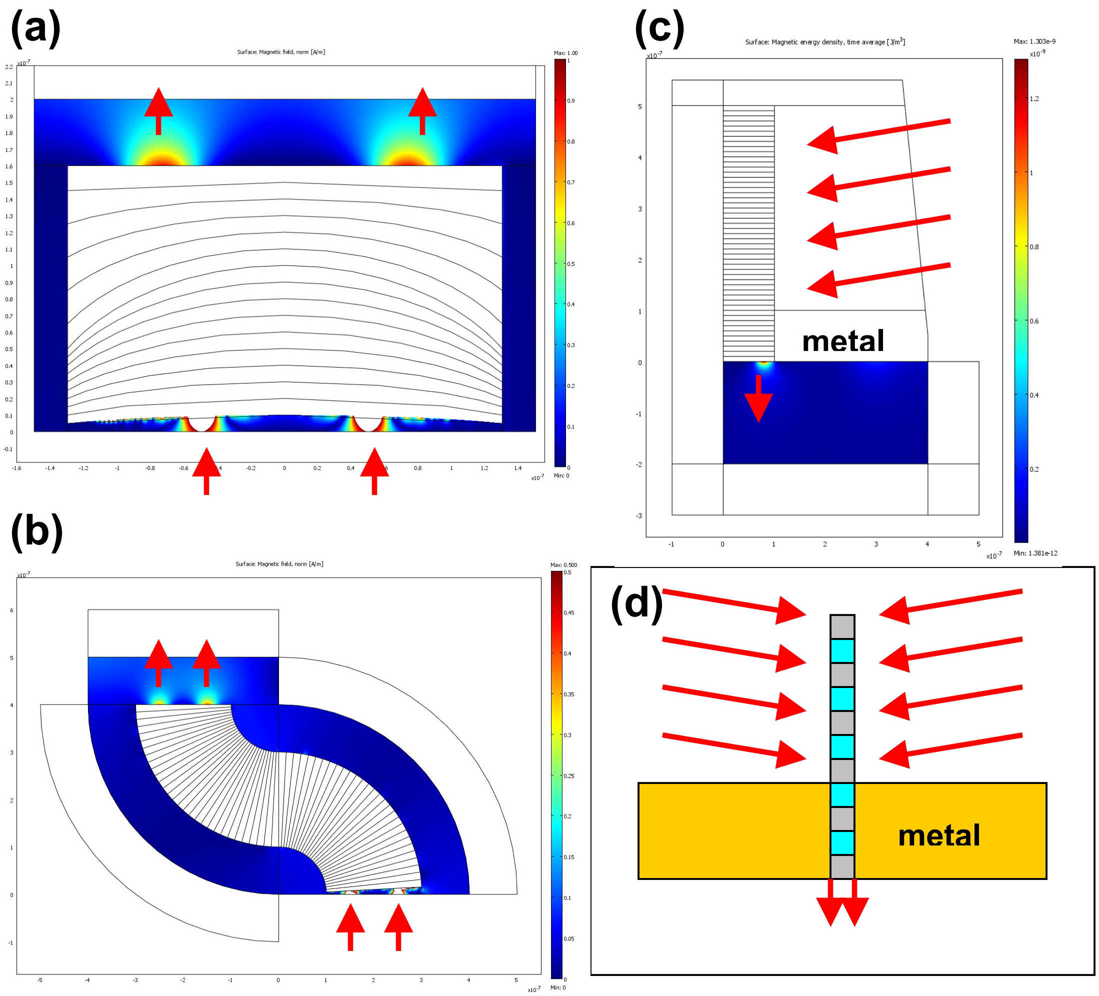

Figure B-1. Metamaterial structures
(a) Metamaterial stack based on the hyperlens, modified to have flat input and output surfaces. Two 25 nm spots separated by 100 nm are input to the bottom of the lens. The output at the top surface consists of two 37 nm spots separated by 150 nm. (b) Metamaterial waveguide that maintains a 100 nm separation between the two input light spots. (c) Metamaterial lens based on the oblique cut stack. The cut angle is taken to be completely vertical to minimize the spot size, and a 100 nm metal layer is used to block the input light coming from the right. (d) Concept for a metamaterial stack combined with a pinhole.

Another alternative to using the curved hyperlens geometry is to use the oblique cut metamaterial stacks, which is also proposed in reference [93]. By using this device in reverse and incorporating a thick metal film to help block light, this device can also focus light to a sub-diffraction limited spot size. Figure B-1c shows the limiting case of such an oblique stack that minimizes the output spot size. In this structure, the light coming from the right impinges upon a completely vertical wall of a metamaterial stack in which the light can only propagate vertically downwards. The spot size in this case is determined solely by the evanescent penetration of the light into the metamaterial stack, without the additional size due to the projected area of the input face as in the non-vertical oblique cut case. This device also uses a metal film to prevent the input light from the upper right from reaching the bottom of the device, thereby maintaining a darkfield output. The commercially available FEM software COMSOL was used to simulate the above structures.

An alternative design for this type of metamaterial stack based device would be to shape the metamaterial stack into a pillar, which would cause the spot size to be determined by the cross sectional shape of this pillar. If one neglects the part of the pillar that sticks out above the metal film (which serves to capture more power), this structure would be similar to filling a pinhole device with a metamaterial. To determine if such a device would be better than a plain pinhole, one would have to look at the loss and propagation characteristics of light within a metamaterial-filled pinhole. If a metamaterial-filled pinhole structure has desirable propagation and loss characteristics, then one would need to determine the best type of metamaterial stack to capture and focus power to this pinhole, which may be similar to the curved hyperlens described above.

Appendix C – Plasmonic modes of a cylindrical waveguide

C.1 Cylindrical plasmonic mode – Motivation

In this appendix, we will derive the plasmonic modes for a cylindrical dielectric waveguide surrounded by metal (e.g. a pinhole in an infinite metal film). The reason we are trying to derive these modes is to gain a physical understanding of what these modes looks like, to see how we can couple to these modes, and to determine the modes' propagation and loss characteristics. This is inspired by the idea we had for a "darkfield" plasmonic dimple lens discussed in Chapter 3. The basic idea for this darkfield structure is to put a pinhole at the center of the unpolished version of the normal dimple lens presented in Chapter 2, where the pinhole is used to out-couple the light instead of a polished facet. This is similar to the "bullseye" (pinhole with grating) concept [42, 43, 48], except that the double-sided surface plasmon mode at the center of the dimple is more closely matched in size to the cylindrical waveguide than the single-sided plasmon of the bullseye case, which might allow it to couple more efficiently. A schematic of this darkfield structure is shown below in Figure 3-3a.

C.2 Cylindrical plasmonic mode – General field equations

In this section, we derive the general equations for the fields in a cylindrical waveguide, which are then tailored to be plasmonic rather than the typical modes. Subsequent sections of this appendix will go into more detail regarding specific modes and their analyses. For this derivation, we will analyze a cylindrical waveguide following the formulation given in Section 8.9 – "Circular Waveguides" of reference [103]. We will also be following Conway's plasmon mode derivations given in Chapter 2 of reference [55].

The geometry for this waveguide is shown in Figure 3-4, where a cylindrical dielectric of radius a and dielectric constant $\varepsilon_d' > 0$ (Region 1) is embedded in an infinite metal slab with a dielectric constant of $\varepsilon_m' < -\varepsilon_d' < 0$ (Region 2). These restrictions are for the real parts of the dielectric constants; they may have imaginary components as well, which we will neglect for this derivation. The coordinate system is defined so that the z direction is along the axis of the waveguide and the origin is located somewhere on the axis of the waveguide.

Since we are looking for plasmon modes, we will consider only the n = 0 transverse magnetic (TM) and n > 0 hybrid modes of the above waveguide that have fields peaking at the interface and decaying exponentially away from it. We are most interested in a mode that has anti-symmetric charges, similar to the double-sided surface plasmon for the planar MIM case. As in reference [103], we assume that the wave is propagating in the z direction with a propagation constant k_z, so that the mode has a z and time dependence of $e^{j(\omega t - k_z z)}$. Given this temporal and z dependence, the curl equations of Maxwell's equations in cylindrical coordinates can be solved to give E_r, E_φ, H_r, and H_φ in terms of E_z and H_z. These are given below, where we define $k^2 = \omega^2 \mu\varepsilon$ with a frequency of operation ω (Eq. 8.9.1-4 of [103]):

$$E_r = -\frac{j}{k^2 - k_z^2}[k_z \frac{\partial E_z}{\partial r} + \frac{\omega\mu}{r}\frac{\partial H_z}{\partial \varphi}] \qquad E_\varphi = \frac{j}{k^2 - k_z^2}[-\frac{k_z}{r}\frac{\partial E_z}{\partial \varphi} + \omega\mu \frac{\partial H_z}{\partial r}]$$

$$H_r = \frac{j}{k^2 - k_z^2}[\frac{\omega\varepsilon}{r}\frac{\partial E_z}{\partial \varphi} - k_z \frac{\partial H_z}{\partial r}] \qquad H_\varphi = -\frac{j}{k^2 - k_z^2}[\omega\varepsilon \frac{\partial E_z}{\partial r} + \frac{k_z}{r}\frac{\partial H_z}{\partial \varphi}]$$

Given the above Maxwell's equations, we can then derive the electromagnetic fields that satisfy them. The following sections will be explained for the E fields, since the equations would be similar for the H fields. Assuming the same z and time dependence, the Helmholtz equations (wave equations for the phasor fields) for E can be written (Eq. 8.2.1 of [103]):

$$\nabla_t^2 \vec{E} = -(k^2 - k_z^2)\vec{E} \qquad \rightarrow \qquad \nabla_t^2 E_z = -(k^2 - k_z^2) E_z$$

In cylindrical coordinates, this is (Eq. 8.9.6 of [103]):

$$\nabla_t^2 E_z = \frac{1}{r}\frac{\partial}{\partial r}(r\frac{\partial E_z}{\partial r}) + \frac{1}{r^2}\frac{\partial^2 E_z}{\partial \varphi^2} = -(k^2 - k_z^2)E_z = -k_r^2 E_z$$

Assuming a product solution to the wave equation where the r and φ dependence are separable, the r dependence has Bessel function solutions and φ dependence has sinusoidal solutions:

$$E_z(r, \varphi, z, t) = R(r)F(\varphi)\mathrm{Z}(\mathrm{z}, \mathrm{t})$$

where (Eq. 7.20.5 of [103]):

$$R(r) = AJ_n(k_r r) + BN_n(k_r r) \qquad k_r^2 = k^2 - k_z^2$$

$$F(\varphi) = C\cos(n\varphi) + D\sin(n\varphi)$$

$$Z(z,t) = e^{j(\omega t - k_z z)}$$

and we can choose our coordinate system for φ such that D = 0 and C = 1.

For a plasmon mode, we assume that $k_z >> k$, and hence k_r is large and imaginary (analogous to k_x for the surface plasmon case in reference [55]). Since r is real, this means that the arguments to the Bessel functions are imaginary. If we let $k_r = j\tau$, $\tau > 0$, we can use a solution for R(r) based on modified Bessel functions:

$$R(r) = AI_n(\tau r) + BK_n(\tau r)$$

where (Eq. 7.14.16-17 of [103]):

$$I_n(\tau r) = j^{-n} J_n(j\tau r) \qquad \tau^2 = -k_r^2 = k_z^2 - k^2 = k_z^2 - \frac{\varepsilon_r \omega^2}{c^2}$$

$$K_n(\tau r) = \frac{\pi}{2} j^{n+1} H_n^{(1)}(j\tau r)$$

The functions I_n and K_n are modified Bessel functions of the first and second kinds, respectively. These functions are exponentials in cylindrical coordinates, analogous to the exponentials that are used for normal surface plasmon modes. Here, τ plays the role of K, the decay constant into the dielectric or metal. Since I_n diverges as $r \to \infty$ and K_n diverges at r = 0, this means that we must have A = 0 in region 1 and B = 0 in region 2 of the cylindrical waveguide geometry.

C.3 Cylindrical plasmonic mode – TM n = 0 mode

Given the general solutions from the previous section, let us first consider a TM n = 0 mode. Since $H_z = 0$ for TM modes, the Maxwell's equations simplify to the following:

$$E_r = -\frac{jk_z}{k^2 - k_z^2}\frac{\partial E_z}{\partial r} \qquad E_\varphi = -\frac{jk_z}{k^2 - k_z^2}\frac{1}{r}\frac{\partial E_z}{\partial \varphi}$$

$$H_r = \frac{j\omega\varepsilon}{k^2 - k_z^2}\frac{1}{r}\frac{\partial E_z}{\partial \varphi} \qquad H_\varphi = -\frac{j\omega\varepsilon}{k^2 - k_z^2}\frac{\partial E_z}{\partial r}$$

where the E and H fields are related by $E_r = ZH_\varphi$ and $E_\varphi = -ZH_r$, with $Z = k_z/\omega\varepsilon$.

Since these fields are related, we will list only the complete solutions for the E fields in each region of the waveguide. The modified Bessel function solutions for E_z are as follows:

$$E_{z1}(r,z,t) = BK_0(\tau_m r)e^{j(\omega t - k_z z)} \qquad E_{z2}(r,z,t) = AI_0(\tau_d r)e^{j(\omega t - k_z z)}$$

which can be plugged into the Maxwell's equations to give:

$$E_{r1}(r,z,t) = \frac{jk_z}{\tau_m^2}\frac{\partial E_{z1}}{\partial r} = \frac{jk_z}{\tau_m}BK_0'(\tau_m r)e^{j(\omega t - k_z z)} \qquad E_{\varphi 1}(r,z,t) = \frac{jk_z}{\tau_m^2}\frac{1}{r}\frac{\partial E_{z1}}{\partial \varphi} = 0$$

$$E_{r2}(r,z,t) = \frac{jk_z}{\tau_d^2}\frac{\partial E_{z2}}{\partial r} = \frac{jk_z}{\tau_d}AI_0'(\tau_d r)e^{j(\omega t - k_z z)} \qquad E_{\varphi 2}(r,z,t) = \frac{jk_z}{\tau_d^2}\frac{1}{r}\frac{\partial E_{z2}}{\partial \varphi} = 0$$

where $\tau_{d,m}^2 = k_z^2 - \frac{\varepsilon_{d,m}\omega^2}{c^2} = k_z^2 - \varepsilon_{d,m}k_0^2$.

The field and charge distribution of the n = 0 mode are shown in Figure 3-5a,c. However, the charge distribution is symmetric for this mode. Thus, it does not correspond to the double-sided surface plasmon from the planar MIM case.

C.4 Cylindrical plasmonic mode – Hybrid n > 0 modes

The higher order modes of the cylindrical waveguides are not strictly TE or TM, but are instead hybrid modes. The modified Bessel function solutions for E_z and H_z for n > 0 are as follows:

$$E_{z1}(r,\varphi,z,t) = BK_n(\tau_m r)\cos(n\varphi)e^{j(\omega t - k_z z)}$$

$$E_{z2}(r,\varphi,z,t) = AI_n(\tau_d r)\cos(n\varphi)e^{j(\omega t - k_z z)}$$

$$H_{z1}(r,\varphi,z,t) = DK_n(\tau_m r)\sin(n\varphi)e^{j(\omega t - k_z z)}$$

$$H_{z2}(r,\varphi,z,t) = CI_n(\tau_d r)\sin(n\varphi)e^{j(\omega t - k_z z)}$$

which can be plugged into the Maxwell's equations to give:

$$\begin{aligned} E_{\varphi 1}(r,\varphi,z,t) &= -\frac{j}{\tau_m^2}[-\frac{k_z}{r}\frac{\partial E_{z1}}{\partial \varphi} + \omega\mu_0 \frac{\partial H_{z1}}{\partial r}] \\ &= -\frac{j}{\tau_m^2}[\frac{k_z}{r}BK_n(\tau_m r)n\sin(n\varphi) + \omega\mu_0\tau_m DK'_n(\tau_m r)\sin(n\varphi)]e^{j(\omega t - k_z z)} \end{aligned}$$

$$\begin{aligned} E_{\varphi 2}(r,\varphi,z,t) &= -\frac{j}{\tau_d^2}[-\frac{k_z}{r}\frac{\partial E_{z2}}{\partial \varphi} + \omega\mu_0 \frac{\partial H_{z2}}{\partial r}] \\ &= -\frac{j}{\tau_d^2}[\frac{k_z}{r}AI_n(\tau_d r)n\sin(n\varphi) + \omega\mu_0\tau_d CI'_n(\tau_d r)\sin(n\varphi)]e^{j(\omega t - k_z z)} \end{aligned}$$

$$\begin{aligned} H_{\varphi 1}(r,\varphi,z,t) &= \frac{j}{\tau_m^2}[\omega\varepsilon_m\varepsilon_0 \frac{\partial E_{z1}}{\partial r} + \frac{k_z}{r}\frac{\partial H_{z1}}{\partial \varphi}] \\ &= \frac{j}{\tau_m^2}[\omega\varepsilon_m\varepsilon_0\tau_m BK'_n(\tau_m r)\cos(n\varphi) + \frac{k_z}{r}DK_n(\tau_m r)n\cos(n\varphi)]e^{j(\omega t - k_z z)} \end{aligned}$$

$$\begin{aligned} H_{\varphi 2}(r,\varphi,z,t) &= \frac{j}{\tau_d^2}[\omega\varepsilon_d\varepsilon_0 \frac{\partial E_{z2}}{\partial r} + \frac{k_z}{r}\frac{\partial H_{z2}}{\partial \varphi}] \\ &= \frac{j}{\tau_d^2}[\omega\varepsilon_d\varepsilon_0\tau_d AI'_n(\tau_d r)\cos(n\varphi) + \frac{k_z}{r}CI_n(\tau_d r)n\cos(n\varphi)]e^{j(\omega t - k_z z)} \end{aligned}$$

$$E_{r1}(r,\varphi,z,t)=\frac{j}{\tau_m^2}[k_z\frac{\partial E_{z1}}{\partial r}+\frac{\omega\mu_0}{r}\frac{\partial H_{z1}}{\partial\varphi}]$$
$$=\frac{j}{\tau_m^2}[k_z\tau_m BK_n'(\tau_m r)\cos(n\varphi)+\frac{\omega\mu_0}{r}DK_n(\tau_m r)n\cos(n\varphi)]e^{j(\omega t-k_z z)}$$

$$E_{r2}(r,\varphi,z,t)=\frac{j}{\tau_d^2}[k_z\frac{\partial E_{z2}}{\partial r}+\frac{\omega\mu_0}{r}\frac{\partial H_{z2}}{\partial\varphi}]$$
$$=\frac{j}{\tau_d^2}[k_z\tau_d AI_n'(\tau_d r)\cos(n\varphi)+\frac{\omega\mu_0}{r}CI_n(\tau_d r)n\cos(n\varphi)]e^{j(\omega t-k_z z)}$$

$$H_{r1}(r,\varphi,z,t)=-\frac{j}{\tau_m^2}[\frac{\omega\varepsilon_m\varepsilon_0}{r}\frac{\partial E_{z1}}{\partial\varphi}-k_z\frac{\partial H_{z1}}{\partial r}]$$
$$=-\frac{j}{\tau_m^2}[-\frac{\omega\varepsilon_m\varepsilon_0}{r}BK_n(\tau_m r)n\sin(n\varphi)-k_z\tau_m DK_n'(\tau_m r)\sin(n\varphi)]e^{j(\omega t-k_z z)}$$
$$H_{r2}(r,\varphi,z,t)=-\frac{j}{\tau_d^2}[\frac{\omega\varepsilon_d\varepsilon_0}{r}\frac{\partial E_{z2}}{\partial\varphi}-k_z\frac{\partial H_{z2}}{\partial r}]$$
$$=-\frac{j}{\tau_d^2}[-\frac{\omega\varepsilon_d\varepsilon_0}{r}AI_n(\tau_d r)n\sin(n\varphi)-k_z\tau_d CI_n'(\tau_d r)\sin(n\varphi)]e^{j(\omega t-k_z z)}$$

where $\tau_{d,m}^2=k_z^2-\varepsilon_{d,m}k_0^2$.

The field and charge distribution of the n = 1 hybrid mode are also shown in Figure 3-5b,d. This mode has an anti-symmetric charge distribution that corresponds to the double-sided surface plasmon in the planar MIM case.

C.5 Cylindrical plasmonic mode – Dispersion relations

In order to calculate the dispersion relations for these plasmonic modes for a given cylinder of radius a, we must ensure that the modes satisfy the boundary conditions at r = a, which is continuity for the transverse fields E_z, E_φ, H_z, and H_φ, as well as for the displacement current normal to the boundary, $D_r = \varepsilon_{d,m}\varepsilon_0 E_r$. This can be accomplished by solving for the relative values of the constants A, B, C, and D in the above field equations. By eliminating these four unknowns, we can obtain a relationship between ω and k_z for each mode. Since A, B, C, and D can be scaled up or down arbitrarily relative to one another, we choose A = 1.

C.5.1 Cylindrical plasmonic mode – Dispersion relations for n = 0 (TM)

For the n = 0 TM mode, let us consider the continuity of E_z and D_r at r = a:

$$E_z : BK_0(\tau_m a) = I_0(\tau_d a)$$

$$D_r : \varepsilon_m \frac{jk_z}{\tau_m} BK_0'(\tau_m a) = \varepsilon_d \frac{jk_z}{\tau_d} I_0'(\tau_d a)$$

Solving each of these equations for B and equating the results gives:

$$\Rightarrow \frac{\varepsilon_m}{\varepsilon_d}\frac{\tau_d}{\tau_m}\frac{I_0(\tau_d a)}{K_0(\tau_m a)} = \frac{I_0'(\tau_d a)}{K_0'(\tau_m a)}$$

where $\tau_{d,m}^2 = k_z^2 - \varepsilon_{d,m} k_0^2$.

This gives us an implicit equation relating ω and k_z, which can be solved numerically for a given size a. Using these formulae for the derivatives (Eq. 7.15.14-15 of [103]):

$$I_0'(x) = I_1(x) \qquad\qquad K_0'(x) = -K_1(x)$$

we can rewrite the above dispersion equation as:

$$\varepsilon_m \tau_d I_0(\tau_d a) K_1(\tau_m a) + \varepsilon_d \tau_m K_0(\tau_m a) I_1(\tau_d a) = 0$$

This dispersion relation equation for the n = 0 TM mode was solved numerically in Matlab for varying values of a in the Ag/SiO_2 material system, using only the real parts of the dielectric constants, and the results are plotted in Figure C-1a. For holes below a certain size (between 50 and 100 nm), it appears that n = 0 modes no longer exist below the surface plasmon resonance frequency. It also seems that for smaller radius cylinders, the n = 0 modes have k-vectors smaller than that of single-sided surface plasmons, which is opposite to the behavior of double-sided surface plasmon modes.

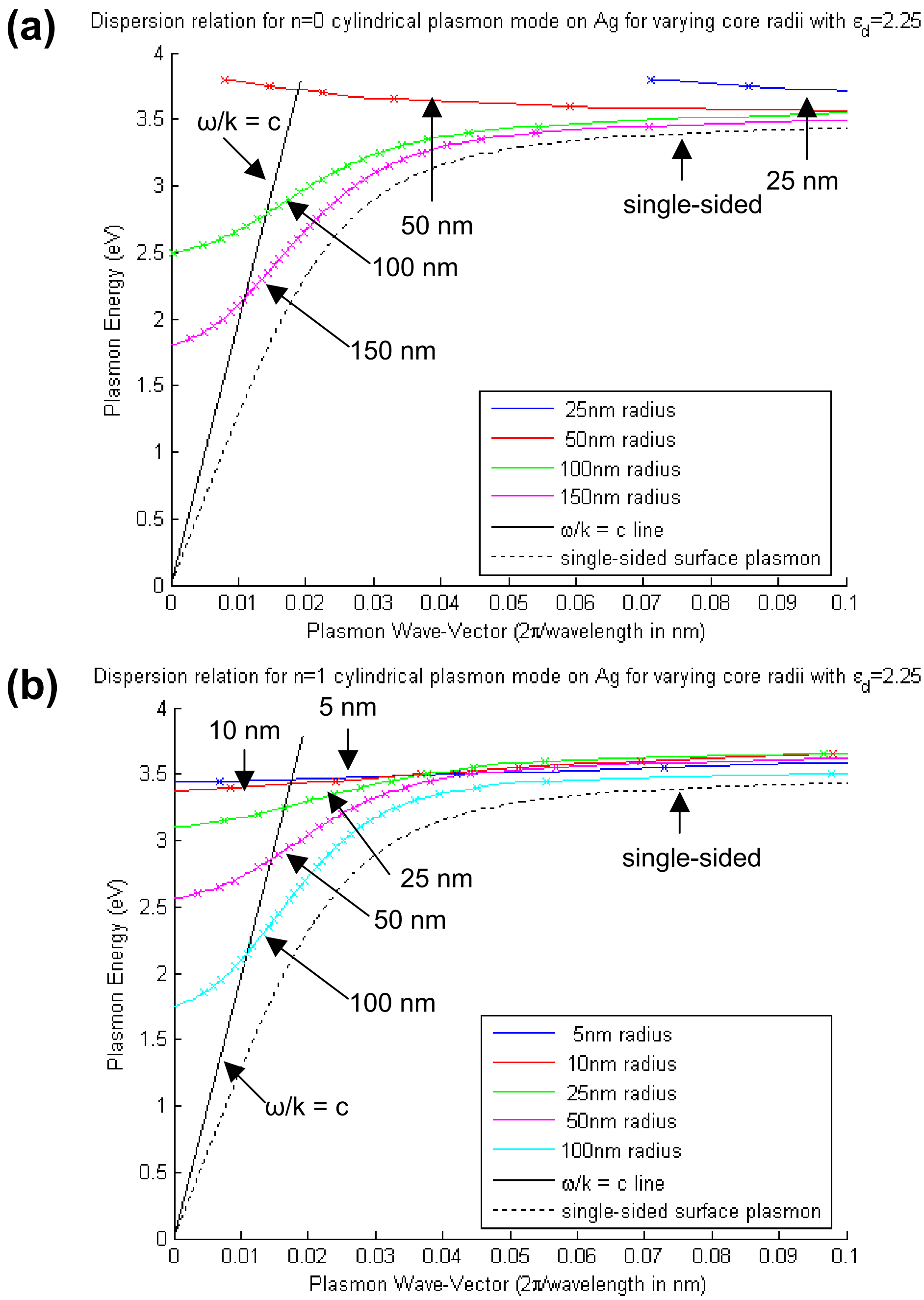

Figure C-1. Ag plasmonic mode dispersion relations
Dispersion relations for the (a) n = 0 TM and (b) n = 1 hybrid plasmon modes in a cylindrical waveguide for varying radii for the Ag/SiO_2 system. These relations were obtained from a numerical solution of the implicit dispersion relation in Matlab.

C.5.2 Cylindrical plasmonic mode – Dispersion relations for n > 0 (hybrid)

For the n > 0 hybrid modes, let us consider the continuity of the transverse E and H fields at r = a:

$$E_z : BK_n(\tau_m a) = AI_n(\tau_d a)$$

$$H_z : DK_n(\tau_m a) = CI_n(\tau_d a)$$

$$E_\varphi : \frac{1}{\tau_m^2}[\frac{nk_z}{a} BK_n(\tau_m a) + \omega\mu_0\tau_m DK_n'(\tau_m a)] = \frac{1}{\tau_d^2}[\frac{nk_z}{a} AI_n(\tau_d a) + \omega\mu_0\tau_d CI_n'(\tau_d a)]$$

$$H_\varphi : \frac{1}{\tau_m^2}[\omega\varepsilon_m\varepsilon_0\tau_m BK_n'(\tau_m a) + \frac{nk_z}{a} DK_n(\tau_m a)] = \frac{1}{\tau_d^2}[\omega\varepsilon_d\varepsilon_0\tau_d AI_n'(\tau_d a) + \frac{nk_z}{a} CI_n(\tau_d a)]$$

Once again, we let A = 1, and eliminate B, C, and D from these equations to obtain:

$$\Rightarrow [\frac{\varepsilon_d}{\tau_d}\frac{I_n'(\tau_d a)}{I_n(\tau_d a)} - \frac{\varepsilon_m}{\tau_m}\frac{K_n'(\tau_m a)}{K_n(\tau_m a)}][\frac{1}{\tau_d}\frac{I_n'(\tau_d a)}{I_n(\tau_d a)} - \frac{1}{\tau_m}\frac{K_n'(\tau_m a)}{K_n(\tau_m a)}] = \frac{n^2k_z^2}{a^2k_0^2}[\frac{1}{\tau_d^2} - \frac{1}{\tau_m^2}]^2$$

where $\tau_{d,m}^2 = k_z^2 - \varepsilon_{d,m}k_0^2$.

Just as for the n = 0 case, this is an implicit equation relating ω and k_z, which can be solved numerically for a given size a. Using the following general formulae for the derivatives (Eq. 7.15.14-15 of [103]):

$$I_n'(x) = \frac{n}{x}I_n(x) + I_{n+1}(x) \qquad\qquad K_n'(x) = \frac{n}{x}K_n(x) - K_{n+1}(x)$$

and letting $I_n = I_n(\tau_d a)$, $I_{n+1} = I_{n+1}(\tau_d a)$, $K_n = K_n(\tau_m a)$, and $K_{n+1} = K_{n+1}(\tau_m a)$, we can rewrite the dispersion relation equation as:

$$
\begin{aligned}
&\Rightarrow [\frac{\varepsilon_d}{\tau_d}[\frac{n}{\tau_d a} I_n + I_{n+1}]K_n - \frac{\varepsilon_m}{\tau_m}[\frac{n}{\tau_m a} K_n - K_{n+1}]I_n] \\
&\times [\frac{1}{\tau_d}[\frac{n}{\tau_d a} I_n + I_{n+1}]K_n - \frac{1}{\tau_m}[\frac{n}{\tau_m a} K_n - K_{n+1}]I_n] \\
&= \frac{n^2 k_z^2}{a^2 k_0^2}[\frac{\tau_m^2 - \tau_d^2}{\tau_d^2 \tau_m^2}]^2 (I_n K_n)^2
\end{aligned}
$$

$$
\begin{aligned}
&\Rightarrow [[\varepsilon_d \tau_m^2 - \varepsilon_m \tau_d^2] I_n K_n + \frac{a}{n}\tau_d \tau_m [\varepsilon_d \tau_m I_{n+1} K_n + \varepsilon_m \tau_d I_n K_{n+1}]] \\
&\times [[\tau_m^2 - \tau_d^2] I_n K_n + \frac{a}{n}\tau_d \tau_m [\tau_m I_{n+1} K_n + \tau_d I_n K_{n+1}]] \\
&- \frac{k_z^2}{k_0^2}[\tau_m^2 - \tau_d^2]^2 (I_n K_n)^2 = 0
\end{aligned}
$$

This dispersion relation equation for the n = 1 hybrid mode was solved numerically in Matlab for varying values of a in the Ag/SiO_2 material system, using only the real parts of the dielectric constants. The results are plotted in Figure C-1b. These curves are similar to those of reference [105] for an Al/glass material system. Similar to the n = 0 case, it also seems that for smaller radius cylinders, the n = 1 modes have k-vectors smaller than that of single-sided surface plasmons.

As you can see from the dispersion plot, there is a band of allowed frequencies of light for a cylinder of a given size. The upper bound of this range appears to always be the surface plasmon resonance frequency, as one might expect. As the size of the hole decreases, the band becomes narrower, with the lower limit increasing in frequency, but the upper limit staying the same. Thus, for smaller hole sizes one would have to operate closer to the surface plasmon resonance frequency. Since very high k-vectors are present at the surface plasmon resonance, there are always some allowed modes at the resonance for any size cylinder.

However, one must also consider the losses for these modes. Although there is a non-zero real part for these propagation constants, the relative size of the imaginary part would tell us how quickly it decays compared to the wavelength of the mode in the waveguide. Unfortunately, after including the imaginary part of the metal's dielectric constant in the implicit dispersion relation equation, the numerical solver was unable to provide reliable values for the complex propagation constants. Instead, we turn to other methods to estimate the losses for these modes, as was discussed in Chapter 3 and will also be discussed in the following section.

C.6 Cylindrical plasmonic mode – Loss considerations

Let us examine the losses for the n = 1 mode, since it has a charge distribution that is similar to that of the double-sided surface plasmon for the MIM slab geometry. First, consider the high-k limit, where $\tau_d \approx \tau_m \approx k_z \approx \tau$. In this limit, the n > 0 dispersion relation becomes:

$$\Rightarrow [\varepsilon_d \frac{I_n'(\tau a)}{I_n(\tau a)} - \varepsilon_m \frac{K_n'(\tau a)}{K_n(\tau a)}][\frac{I_n'(\tau a)}{I_n(\tau a)} - \frac{K_n'(\tau a)}{K_n(\tau a)}] = 0$$

Expanding the first of these terms gives:

$$\Rightarrow \varepsilon_d K_n(\tau a)[\frac{n}{\tau a} I_n(\tau a) + I_{n+1}(\tau a)] - \varepsilon_m I_n(\tau a)[\frac{n}{\tau a} K_n(\tau a) - K_{n+1}(\tau a)] = 0$$

We can use the following two asymptotic forms (Eq. 7.15.5-6 of [22]):

$$\lim_{x->\infty} I_n(x) = \sqrt{\frac{1}{2\pi x}} e^x \qquad \lim_{x->\infty} K_n(x) = \sqrt{\frac{\pi}{2x}} e^{-x}$$

to evaluate the limit of the left hand side of the above high-k limit dispersion relation equation for $\tau a \to \infty$, which gives:

$$\Rightarrow \varepsilon_d[\frac{n}{\tau a} + 1] - \varepsilon_m[\frac{n}{\tau a} - 1] = 0 \qquad \Rightarrow \tau a = n\frac{(\varepsilon_m - \varepsilon_d)}{(\varepsilon_m + \varepsilon_d)}$$

For a 2.6 eV photon (476 nm wavelength) of light in the Ag/SiO_2 material system, this gives:

$$\tau a = n(1.94 + 0.0527i) \qquad \Rightarrow \lambda_p = \frac{2\pi}{\tau'} = \frac{3.24}{n} a$$

$$\Rightarrow \alpha^{-1} = \frac{2\pi}{\tau''} = \frac{19}{n} a$$

For the n = 1 mode, this means the decay length is about ten times the waveguide diameter. For example, for a = 50 nm, the decay length is almost 1 μm.

We can compare this above result with the lossless decay length for a normal TE/TM mode of a cylindrical waveguide, when the wavelength is larger than the cutoff wavelength for the given radius. The propagation constant k_z in the cylindrical waveguide is given by (Eq. 8.9.5 of [103]):

$$k_z^2 = k^2 - k_c^2$$

where k_c is the cutoff wave-vector. When $k < k_c$, k_z becomes imaginary, and hence the mode decays rather than propagating in the waveguide (even without considering material losses, i.e. complex dielectric constants). The cylindrical waveguide mode with the lowest cutoff is the TE_{11} mode, which has a cutoff of (Table 8.9 of [103]):

$$k_c = \frac{1.84}{a}$$

For 2.6 eV light, we can find the cutoff radius a_c (where $k = k_c$) to be:

$$a_c = \frac{1.84}{k} = \frac{1.84}{2\pi\sqrt{\varepsilon_d}}\lambda = 93nm$$

So, for waveguides of radius less than a_c = 93 nm, the mode decays even without loss. Let us again consider the waveguide with radius a = 50 nm. This gives us

$$k = \frac{2\pi\sqrt{\varepsilon_d}}{\lambda} = \frac{2\pi(1.5)}{476nm} = 0.0198nm^{-1}$$

$$k_c = \frac{1.84}{a} = \frac{1.84}{50nm} = 0.0368nm^{-1}$$

$$k_z = \sqrt{k^2 - k_c^2} = \sqrt{(0.0198nm^{-1})^2 - (0.0368nm^{-1})^2} = i0.0310nm^{-1}$$

$$\alpha = k_z'' = 0.0310 nm^{-1} \qquad \rightarrow \qquad \alpha^{-1} = 32 nm$$

In this case, the decay length is roughly of the same order as the radius of the waveguide. This decay length decreases for smaller radii, as can be seen from a Taylor series expansion on the decay length for $k_c >> k$, which gives:

$$\alpha^{-1} = (k_c^2 - k^2)^{-1/2} = \frac{1}{k_c}[1-(\frac{k}{k_c})^2]^{-1/2} \approx \frac{a}{1.84}[1+\frac{1}{2}(\frac{k}{k_c})^2] \rightarrow \frac{a}{1.84}$$

Thus, as the radius of the waveguide decreases ($a << a_c$), the decay length tends towards about half the radius. For small waveguides, this lossless decay length for the TE_{11} mode is 35 times smaller than the decay length of the n = 1 plasmonic mode due to losses in the high-k limit for the Ag/SiO_2 material system with 2.6 eV light. Thus, the high-k plasmonic modes of these waveguides should have lower losses than the conventional optical modes of the waveguides that are cutoff for small sizes. If we can efficiently excite/couple to these specific modes, we would be able to propagate light through the pinhole better.

Appendix D – Electric dipole radiation of parallel wires

D.1 Wire dipole radiation – Introduction

In this appendix, we will derive an expression for the power that is radiated by closely spaced parallel wires ($a << \lambda$) that are longer than the wavelength of interest ($L > \lambda$). Each wire has a uniform spatial charge distribution that varies only in time. Thus, these wires can be viewed as an electric dipole that is large in one dimension but small in the other two dimensions, as shown in Figure D-11a. This is similar to the case of a capacitor, which is large in two dimensions but small in the third. The radiation from a capacitor was derived in reference [118], and thus the derivations are similar.

In order to determine the total power radiated by parallel wires, we will break the wires into small pieces that are regular sub-wavelength dipole radiators. We can then sum the radiation resulting from each of these pieces to determine the total radiation pattern produced by the radiating wires. This radiation pattern can then be integrated over the desired solid angle to determine the total power radiated by the parallel wires.

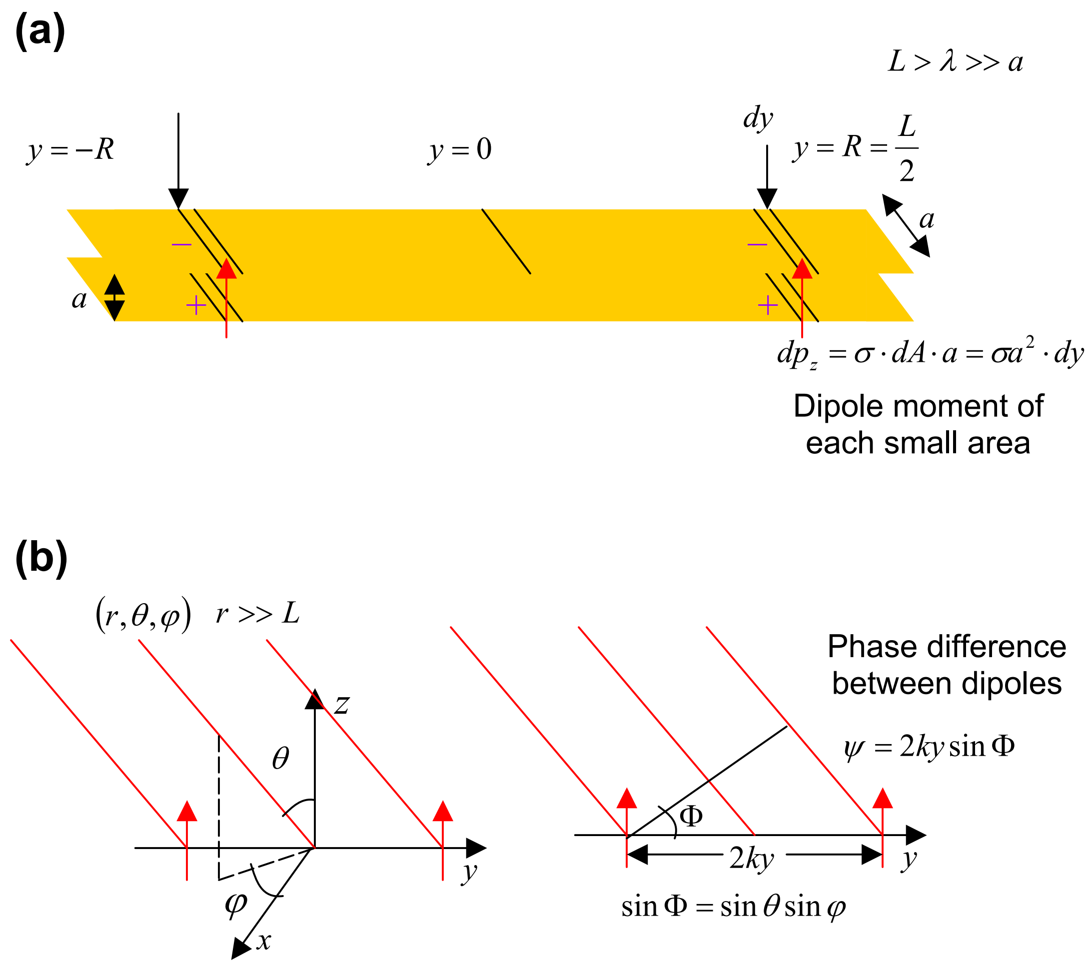

Figure D-1. Wire dipole radiation geometry
(a) Geometry and coordinate system for determining the dipole radiation of parallel wires. (b) Schematic for determining the phase difference between two symmetric electric dipoles in order to sum their E fields at a distant point.

D.2 Wire dipole radiation – Radiation pattern

In order to derive the radiation pattern from parallel wires, we first break up the wire into little sub-wavelength pieces of length dy, area $dA = a \cdot dy$, and dipole moment $dp_z = \sigma \cdot dA \cdot a = \sigma a^2 \cdot dy$, as shown in Figure D-1a. The charge density σ can be related to the total charge Q by $\sigma = Q/aL$, and the total dipole moment of the wire is $|p| = \int dp_z = \sigma a^2 \cdot 2R = \sigma a^2 L = Qa$.

For a point (r, θ, φ) far away from the wires (r >> L), the E field due to one of these electric dipoles dp_z is independent of the position y of the dipole, and is given by the following expression:

$$dE_0 = \frac{1}{4\pi\varepsilon_0}\frac{\omega^2}{c^2 r} dp_z \sin\theta \cos(\omega t - kr)$$

where $k = \omega/c = 2\pi/\lambda$.

Next, let us sum the field from two symmetric electric dipoles (located at equal distances from the center of the wire, y = 0), as shown in Figure D-1b. Although the E fields of the electric dipoles are independent of the dipole positions, the phase difference between the two dipoles is $\psi = 2ky\sin\Phi$. This gives the following expression for the summed E field:

$$dE = 2dE_0 \cos\left(\frac{\psi}{2}\right) = \frac{1}{2\pi\varepsilon_0}\frac{\omega^2}{c^2 r}\sigma a^2 dy \sin\theta \cos(ky\sin\theta\sin\varphi)\cos(\omega t - kr)$$

We can then integrate this expression over one half of the wire to find the total E field due to the wires at the distant point (r, θ, φ):

$$E(r,\theta,\varphi)=\int dE=\frac{\sigma a^2}{2\pi\varepsilon_0}\frac{\omega^2}{c^2 r}\sin\theta\int_0^R\cos(ky\sin\theta\sin\varphi)dy\cos(\omega t-kr)$$

$$\Rightarrow\frac{\sigma a^2}{2\pi\varepsilon_0}\frac{\omega^2}{c^2 r}\sin\theta\frac{1}{k\sin\theta\sin\varphi}\sin(kR\sin\theta\sin\varphi)\cos(\omega t-kr)$$

$$\Rightarrow\frac{\sigma\omega a^2}{2\pi\varepsilon_0 cr}\frac{1}{\sin\varphi}\sin(kR\sin\theta\sin\varphi)\cos(\omega t-kr)$$

This formula for the E field produced by the parallel wires can then be used to find the Poynting vector, or radiation pattern.

The Poynting vector can be related to the square of the E field in free space by the following expression [17]:

$$S=E\times H=\frac{1}{2}c\varepsilon_0|E|^2$$

If we consider only the θ, φ dependence of the radiation, the $|E|^2$ radiation pattern varies with the size of the wire ($kR=2\pi R/\lambda$), as shown in Figure D-2. As expected, this radiation pattern has the typical dipole radiation pattern for small kR, which is almost a torus-shape as a function of θ, φ (i.e. no variation with φ). As the length of the wire increases, this torus is modified by becoming more collimated in the φ dependence, similar to how light will have a smaller divergence angle from wide planar waveguides.

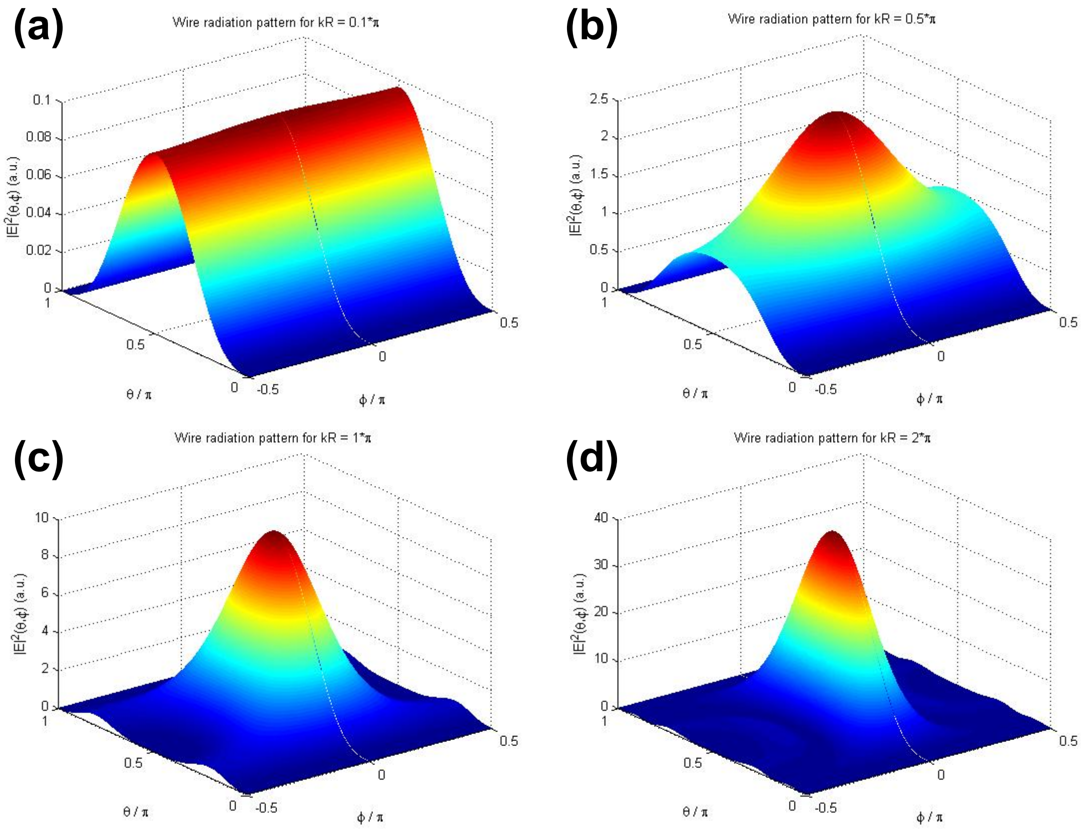

Figure D-2. Wire dipole radiation pattern
The θ, φ dependence of the $|E|^2$ radiation patterns for wires of varying lengths, L = 2R: (a) kR = π/10, (b) kR = π/2, (c) kR = π, and (d) kR = 2π.

D.3 Wire dipole radiation – Total radiated power

Now that we have the $|E|^2$ radiation pattern from the previous section, we can integrate in spherical coordinates over the desired solid angle to determine the total radiated power using the following formula:

$$P_{rad} = \oint_A (E \times H) \cdot \hat{n} dA = \iint \left(\frac{1}{2} c \varepsilon_0 |E|^2 \right) r^2 \sin\theta d\theta d\varphi$$
$$= \frac{1}{2} c \varepsilon_0 \iint \left(\frac{\sigma^2 \omega^2 a^4}{4\pi^2 \varepsilon_0{}^2 c^2} \frac{1}{\sin^2\varphi} \sin^2(kR\sin\theta\sin\varphi) \right) \sin\theta d\theta d\varphi$$

Since our darkfield devices are limited to radiating into only one half-space, $\varphi \in [-\pi/2, \pi/2]$, we calculate just this half of the radiated power:

$$P_{rad,half} = \frac{|p|^2}{L^2} \frac{\omega^2}{8\pi^2 \varepsilon_0 c} \int_0^{\pi} \int_{-\frac{\pi}{2}}^{+\frac{\pi}{2}} \left(\frac{\sin^2(kR\sin\theta\sin\varphi)}{\sin^2\varphi} \right) d\varphi \sin\theta d\theta$$

For small R (R << λ), this gives:

$$P_{rad,half} \approx \frac{|p|^2}{L^2} \frac{\omega^2}{8\pi^2 \varepsilon_0 c} \int_0^{\pi} \int_{-\frac{\pi}{2}}^{+\frac{\pi}{2}} \left(\frac{(kR\sin\theta\sin\varphi)^2}{\sin^2\varphi} \right) d\varphi \sin\theta d\theta$$

$$\Rightarrow \frac{|p|^2}{4R^2} \frac{\omega^2}{8\pi^2 \varepsilon_0 c} k^2 R^2 \int_0^{\pi} \sin^3\theta d\theta \int_{-\frac{\pi}{2}}^{+\frac{\pi}{2}} d\varphi$$
$$\Rightarrow \frac{1}{2} \frac{|p|^2 \omega^4}{16\pi^2 \varepsilon_0 c^3} \frac{4}{3} \pi = \frac{1}{2} \frac{\omega^4}{12\pi \varepsilon_0 c^3} |p|^2$$

As expected, this power radiated by a short wire is the same as the power radiated by a simple sub-wavelength dipole, as presented in Section 3.5.1.

In general, the radiated power cannot be calculated analytically because there is no closed form solution for the integral. However, if we let $A = kR\sin\theta$, where

$\theta \in [0,\pi] \Rightarrow A \in [0,kR]$, we can calculate the power radiated by large wires (L = 2R > λ) by using the following approximation for large A, which was calculated numerically:

$$\int_{-\frac{\pi}{2}}^{+\frac{\pi}{2}} \left(\frac{\sin^2(A\sin\varphi)}{\sin^2\varphi} \right) d\varphi \approx \pi A$$

This approximation can also be derived analytically for large A. First, let $x = A\sin\varphi$, which gives $dx = A\cos\varphi \cdot d\varphi, \cos\varphi = \sqrt{1 - x^2/A^2}$. The integral can then be rewritten:

$$2\int_0^{\frac{\pi}{2}} \left(\frac{\sin^2(A\sin\varphi)}{\sin^2\varphi} \right) d\varphi = 2A\int_0^A \left(\frac{\sin^2 x}{x^2\sqrt{1 - x^2/A^2}} \right) dx$$

Next, we take the limit for large A:

$$\lim_{A\to\infty} \int_0^A \left(\frac{\sin^2 x}{x^2\sqrt{1 - x^2/A^2}} \right) dx = \int_0^\infty \left(\frac{\sin^2 x}{x^2} \right) dx = \frac{\pi}{2}$$

$$\Rightarrow \lim_{A\to\infty} \int_{-\frac{\pi}{2}}^{+\frac{\pi}{2}} \left(\frac{\sin^2(A\sin\varphi)}{\sin^2\varphi} \right) d\varphi = 2A \cdot \frac{\pi}{2} = \pi A$$

This gives the same result as that obtained from numerical integration.

Now that we have an approximation for this integral, we can use it to calculate the power radiated into one half-space for parallel wires with length L > λ:

$$P_{rad,half} \approx \frac{|p|^2}{L^2} \frac{\omega^2}{8\pi^2\varepsilon_0 c} \int_0^\pi (\pi kR\sin\theta)\sin\theta d\theta$$

$$\Rightarrow \frac{|p|^2}{L^2} \frac{\omega^2}{8\pi^2\varepsilon_0 c} \pi kR \frac{\pi}{2} = \frac{1}{2} \frac{\omega^3}{16\varepsilon_0 c^2} \frac{|p|^2}{L}$$

Appendix E – Sheet resistance in the boundaries of a waveguide

This appendix gives a summary of the derivation for the sheet resistance in the metal boundaries around a dielectric optical waveguide. This resistance is used in Section 3.6 to estimate various losses in tapered darkfield structures. The following derivation is based on Section 8.1 – "Fields at the Surface of and within a Conductor" of Jackson [49]. We will be considering the geometry shown in Figure E-1, which represents a square L x L portion of the metal boundary of the waveguide.

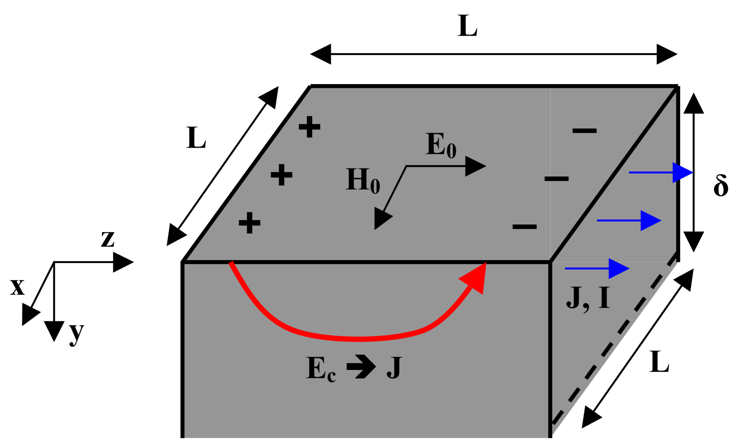

Figure E-1. Metal boundary of a waveguide
Model of the geometry for considering the currents in the metal boundaries of a waveguide to determine the corresponding sheet resistance.

For this derivation, we will neglect the displacement current assuming L << λ. Given the tangential H field at the surface, the E field and current density J in the metal are given by Ampere's law:

$$J = \sigma E_c \approx \nabla \times H$$

The geometric conduction model described in Section 3.6.2 can be used to give a physical understanding of this current density; this model would approximate the current density as $J \approx I/\delta \cdot L$.

Next, let us assume that the H field has a penetration into the metal with skin depth δ. Since we can neglect variations in x, z for L, δ << λ, we have the following simplification for the curl of H:

$$H_c = H_0 e^{-(1-i)y/\delta} \Rightarrow \nabla \times H \approx -\frac{\partial H}{\partial y}\hat{z} \Rightarrow \left|\nabla \times H\right| \approx \frac{1}{\delta}\left|H\right|$$

Since the current has a small penetration into the metal, let us also define an effective surface current K:

$$\frac{I}{L} \equiv K_{eff} \equiv \int_0^\infty J\partial y \Rightarrow \left|K_{eff}\right| \approx \left|\int_0^\infty (\nabla \times H)\partial y\right| \approx \left|\int_0^\infty \frac{\partial H}{\partial y}\partial y\right| \Rightarrow \left|K_{eff}\right| \approx \left|H_0\right|$$

Finally, we will use the Poynting vector S to determine the power flow into the metal surface. This represents the power lost into the boundaries of the waveguide due to resistance. The power lost in the L x L area is given by:

$$\frac{P_{loss}}{L^2} \equiv S \equiv \left|E_0 \times H_0^*\right| \approx \left|\frac{1}{\sigma}(\nabla \times H_0) \times H_0^*\right| \approx \frac{1}{\sigma}\frac{1}{\delta}\left|H_0\right|^2$$
$$\approx \frac{1}{2}\frac{2}{\sigma\delta}\left|K_{eff}\right|^2 = \frac{1}{2}\frac{2}{\sigma\delta}\frac{\left|I\right|^2}{L^2} = \frac{1}{2}R\frac{\left|I\right|^2}{L^2}$$

Since this resistance R is for an L x L area, the above gives us the sheet resistance in the metal boundary of the waveguide, $R = 2/\sigma\delta$.

References

[1] G. Binnig, C. F. Quate, and C. Gerber, "Atomic Force Microscope," Phys. Rev. Lett. 56, 930 (1986)

[2] E. Ruska, "The Development of the Electron Microscope and of Electron Microscopy," Nobel Lecture, December 8, 1986

[3] "Electron microscopy in the 1990s," http://www.sfc.fr/Material/hrst.mit.edu/hrs/materials/public/ElectronMicroscope/EM1990s.htm

[4] R. Y. Tsien, "The Green Fluorescent Protein," Annu. Rev. Biochem. 67, 509 (1998)

[5] P. G. Wu and L. Brand, "Resonance Energy Transfer: Methods and Applications," Analytical Biochemistry 218, 1 (1994)

[6] "Olympus FluoView Resource Center: FRET Introductory Concepts," http://www.olympusfluoview.com/applications/fretintro.html

[7] F. H. Dill, W. P. Hornberger, P. S. Hauge, and J. M. Shaw, "Characterization of Positive Photoresist," IEEE Trans. of Electron Devices 22, 445 (1975)

[8] AZ5214E Image Reversal Photoresist Product Data Sheet, Clariant

[9] A. Ashkin, "Acceleration and Trapping of Particles by Radiation Pressure," Phys. Rev. Lett. 24, 156 (1970)

[10] A. Ashkin, "History of Optical Trapping and Manipulation of Small-Neutral Particle, Atoms, and Molecules," IEEE J. on Selected Topics in Quantum Electronics 6, 841 (2000)

[11] C. Bustamante, Z. Bryant, and S. B. Smith, "Ten years of tension: single-molecule DNA mechanics," Nature 421, 423 (2003)

[12] R. E. Rottmayer, S. Batra, D. Buechel, W. A. Challener, J. Hohlfeld, Y. Kubota, L. Li, B. Lu, C. Mihalcea, K. Mountfield, K. Pelhos, C. Peng, T. Rausch, M. A. Seigler, D. Weller, and X.-M. Yang, "Heat-Assisted Magnetic Recording," IEEE Trans. on Magnetics 42, 2417 (2006)

[13] W. A. Challener, C. Peng, A. V. Itagi, D. Karns, W. Peng, Y. Peng, X. M. Yang, X. Zhu, N. J. Gokemeijer, Y.-T. Hsia, G. Ju, R. E. Rottmayer, M.A. Seigler and E. C. Gage, "Heat-assisted magnetic recording by a near-field transducer with efficient optical energy transfer," Nature Photonics 3, 220 (2009)

[14] T. W. Mcdaniel, W. A. Challener, and K. Sendur, "Issues in Heat-Assisted Perpendicular Recording," IEEE Trans. on Magnetics 39, 1972 (2003)

[15] C. T. Rettner, et al., "Optical aperture for data recording having transmission enhanced by surface plasmon resonance," U.S. Patent 6,982,844 (2006)

[16] W. Srituravanich, L. Pan, Y. Wang, C. Sun, D. B. Bogy, and X. Zhang, "Flying plasmonic lens in the near field for high-speed nanolithography," Nature Nanotech. 3, 733 (2008)

[17] J. M. Liu, Photonic Devices, (Cambridge University Press, 2005)

[18] H. Raether, Surface Plasmons on Smooth and Rough Surfaces and on Gratings, (Springer-Verlag, 1988)

[19] A. V. Zayats, I. I. Smolyaninov, and A. A. Maradudin, "Nano-optics of surface plasmon polaritons," Physics Reports 408, 131 (2005)

[20] A. N. Grigorenko, N. W. Roberts, M. R. Dickinson, and Y. Zhang, "Nanometric optical tweezers based on nanostructured substrates," Nature Photonics 2, 365 (2008)

[21] A. Nahata, R. A. Linke, T. Ishi, and K. Ohashi, "Enhanced nonlinear optical conversion from a periodically nanostructured metal film," Optics Lett. 28, 423 (2006)

[22] M. I. Stockman, "Spasers explained," Nature Photonics 2, 327 (2008)

[23] M. T. Hill, Y. S. Oei, B. Smalbrugge, Y. Zhu, T. De Vries, P. J. Van Veldhoven, F. W. M. Van Otten, T. J. Eijkemans, J. P. Turkiewicz, H. De Waardt, E. Jan Geluk, S. H. Kwon, Y. H. Lee, R. Notzel, and M. K. Smit, "Lasing in metallic-coated nanocavities," Nature Photonics 1, 589 (2007)

[24] H. A. Wheeler, "Fundamental Limits of Small Antennas," Proceedings of the I.R.E. 35, 1479 (1947)

[25] "Nikon MicroscopyU: Concepts and Formulas in Microscopy: Resolution" http://www.microscopyu.com/articles/formulas/formulasresolution.html

[26] ITRS 2000 Update – Lithography

[27] "Introducing the World's First 32nm SRAM logic technology. Only from Intel." http://www.intel.com/technology/architecture-silicon/32nm/index.htm?iid=tech_sil+32nm

[28] I. I. Smolyaninov, Y.-J. Hung, and C. C. Davis, "Magnifying Superlens in the Visible Frequency Range," Science 315, 1699 (2007)

[29] I. I. Smolyaninov, J. Elliott, A. V. Zayats, and C. C. Davis, "Far-Field Optical Microscopy with a Nanometer-Scale Resolution Based on the In-Plane Image Magnification by Surface Plasmon Polaritons," Phys. Rev. Lett. 94, 057401 (2005)

[30] W. L. Barnes, A. Dereux, and T. W. Ebbesen, "Surface plasmon subwavelength optics," Nature 424, 824 (2003)

[31] S. A. Maier, "Plasmonics: The Promise of Highly Integrated Optical Devices," IEEE J. of Selected Topics in Quantum Electronics 12, 1671 (2006)

[32] H. J. Lezec, J. A. Dionne, and H. A. Atwater, "Negative Refraction at Visible Frequencies," Science 316, 430 (2007)

[33] G. Binnig and H. Rohrer, "Scanning tunneling microscopy (Reprinted from IBM Journal of Research and Development, vol 30, 1986)," IBM Journal of Research and Development 44, 279 (2000)

[34] M. I. Stockman, “Nanofocusing of Optical Energy in Tapered Plasmonic Waveguides,” Phys. Rev. Lett. 93, 137404 (2004)

[35] C. Ropers, C. C. Neacsu, T. Elsaesser, M. Albrecht, M. B. Raschke, and C. Lienau, “Grating-Coupling of Surface Plasmons onto Metallic Tips: A Nanoconfined Light Source,” Nano Letters 7, 2784 (2007)

[36] X. L. Shi and L. Hesselink, “Design of a C aperture to achieve lambda/10 resolution and resonant transmission,” J. Opt. Soc. Am. B 21, 1305 (2004)

[37] X. L. Shi, R. L. Thornton, and L. Hesselink, “A Nano-aperture with 1000× Power Throughput Enhancement for Very Small Aperture Laser System (VSAL),” Proc. SPIE 4342, 320 (2002)

[38] L. Wang and X. Xu, “High transmission nanoscale bowtie-shaped aperture probe for near-field optical imaging,” Appl. Phys. Lett. 90, 261105 (2007)

[39] K. Ishihara, K. Ohashi, T. Ikari, H. Minamide, H. Yokoyama, J. Shikata, and H. Ito, “Terahertz-wave near-field imaging with subwavelength resolution using surface-wave-assisted bow-tie aperture,” Appl. Phys. Lett. 89, 201120 (2006)

[40] A. Sundaramurthy, K. B. Crozier, G. S. Kino, D. P. Fromm, P. J. Schuck, and W. E. Moerner, “Field enhancement and gap-dependent resonance in a system of two opposing tip-to-tip Au nanotriangles,” Phys. Rev. B 72, 165409 (2005)

[41] A. Degiron, H. J. Lezec, N. Yamamoto, and T. W. Ebbesen, “Optical transmission properties of a single subwavelength aperture in a real metal,” Optics Comm. 239, 61 (2004)

[42] C. Genet and T. W. Ebbesen, “Light in tiny holes,” Nature 445, 39 (2007)

[43] H. J. Lezec, A. Degiron, E. Devaux, R. A. Linke, L. Martin-Moreno, F. J. Garcia-Vidal, and T. W. Ebbesen, “Beaming light from a subwavelength aperture,” Science 297, 820 (2002)

[44] F. I. Baida, A. Belkhir, and D. Van Labeke, “Subwavelength metallic coaxial waveguides in the optical range: Role of the plasmonic modes,” Phys. Rev. B 74, 205419 (2006)

[45] “Nikon MicroscopyU | Stereomicroscopy | Darkfield Illumination,” http://www.microscopyu.com/articles/stereomicroscopy/stereodarkfield.html

[46] L. Novotny, D. W. Pohl, and B. Hecht, “Light confinement in scanning near-field optical microscopy,” Ultramicroscopy 61, 1 (1995)

[47] B. Hecht, B. Sick, U. P. Wild, V. Deckert, R. Zenobi, O. J. F. Martin, and D. W. Pohl, “Scanning near-field optical microscopy with aperture probes: Fundamentals and applications,” J. Chem. Phys. 112, 7761 (2000)

[48] T. Thio, K. M. Pellerin, R. A. Linke, H. J. Lezec, and T. W. Ebbesen, “Enhanced light transmission through a single subwavelength aperture,” Optics Lett. 26, 1972 (2001)

[49] J. D. Jackson, Classical Electrodynamics, (John Wiley & Sons, 1962)

[50] A. Bouhelier, J. Renger, M. R. Beversluis, and L. Novotny, “Plasmon-coupled tip-enhanced near-field optical microscopy,” J. of Microscopy 210, 220 (2003)

[51] W. Ding, S. R. Andrews, and S. A. Maier, “Internal excitation and superfocusing of surface plasmon polaritons on a silver-coated optical fiber tip,” Phys. Rev. A 75, 063822 (2007)

[52] S. W. Hell, “Toward fluorescence nanoscopy,” Nature Biotech. 21, 1347 (2003)

[53] M. J. Rust, M. Bates, and X. Zhuang, “Sub-diffraction-limit imaging by stochastic optical reconstruction microscopy (STORM),” Nature Methods 3, 793 (2006)

[54] E. Betzig, G. H. Patterson, R. Sougrat, O. Wolf Lindwasser, S. Olenych, J. S. Bonifacino, M. W. Davidson, J. Lippincott-Schwartz, and H. F. Hess, “Imaging Intracellular Fluorescent Proteins at Nanometer Resolution,” Science 313, 1642 (2006)

[55] J. A. Conway, “Efficient Optical Coupling to the Nanoscale,” Ph.D. thesis, University of California, Los Angeles (2006)

[56] H. Lee, S. Vedantam, J. Tang, J. Conway, M. Staffaroni, and E. Yablonovitch, “Demonstration of a Plasmonic Dimple Lens for Nanoscale Focusing of Light,” arXiv:0810.1553v1, (2008)

[57] S. Vedantam, H. Lee, J. Tang, J. Conway, M. Staffaroni, and E. Yablonovitch, “A Plasmonic Dimple Lens for Nanoscale Focusing of Light,” Nano Letters 9, 3447 (2009)

[58] D. F. P. Pile and D. K. Gramotnev, “Adiabatic and nonadiabatic nanofocusing of plasmons by tapered gap plasmon waveguides,” Appl. Phys. Lett. 89, 041111 (2006)

[59] L. Martin-Moreno, F. J. Garcia-Vidal, H. J. Lezec, A. Degiron, and T. W. Ebbesen, “Theory of Highly Directional Emission from a Single Subwavelength Aperture Surrounded by Surface Corrugations,” Phys. Rev. Lett. 90, 167401 (2003)

[60] H. T. Miyazaki and Y. Kurokawa, “Squeezing Visible LightWaves into a 3-nm-Thick and 55-nm-Long Plasmon Cavity,” Phys. Rev. Lett. 96, 097401 (2006)

[61] P. B. Johnson and R. W. Christy, “Optical Constants of the Noble Metals,” Phys. Rev. B 6, 4370 (1972)

[62] P. B. Johnson and R. W. Christy, “Optical constants of transition metals: Ti, V, Cr, Mn, Fe, Co, Ni, Pd,” Phys. Rev. B 9, 5056 (1974)

[63] M. A. Ordal, R. J. Bell, R. W. Alexander, Jr, L. L. Long, and M. R. Querry, “Optical properties of fourteen metals in the infrared and far infrared: Al, Co, Cu, Au, Fe, Pb, Mo, Ni, Pd, Pt, Ag, Ti, V, and W,” Appl. Optics 24, 4493 (1985)

[64] J. Lu, C. Petre, E. Yablonovitch, and J. Conway, “Numerical optimization of a grating coupler for the efficient excitation of surface plasmons at an Ag-SiO2 interface,” J. Opt. Soc. Am. B 24, 2268 (2007)

[65] G. A. Valaskovic, M. Holton, and G. H. Morrison, "Parameter control, characterization, and optimization in the fabrication of optical fiber near-field probes," Appl. Optics 34, 1215 (1995)

[66] "Olympus Microscopy Resource Center: Near-Field Scanning Optical Microscopy – NSOM Probe Aperture Throughput," http://www.olympusmicro.com/primer/java/nearfield/probeaperture/index.html

[67] H. A. Bethe, "Theory of Diffraction by Small Holes," The Phys. Rev. 66, 163 (1944)

[68] C. J. Bouwkamp, "Diffraction Theory," Reports on Progress in Physics 17, 35 (1954)

[69] A. Bendavid, P. J. Martin, and L. Wieczorek, "Morphology and optical properties of gold thin films prepared by filtered arc deposition," Thin Solid Films 354, 169 (1999)

[70] R. Petrovic, S. Strbac, N. Bundaleski, and Z. Rakocevic, "Surface roughness minimum: Ag thin layer deposited on glass," J. Serb. Chem. Soc. 66, 483 (2001)

[71] A. Devasahayam, "Magnetic head processing technology for small form-factor hard drives," Solid State Tech. 48, S16 (2005)

[72] S. Vedantam, H. Lee, J. Tang, J. Conway, M. Staffaroni, J. Lu, and E. Yablonovitch, "Nanoscale Fabrication of a Plasmonic Dimple Lens for Nano-focusing of Light," Proc. of SPIE 6641, 66411J (2007)

[73] "Coefficients of Linear Expansion," http://www.engineeringtoolbox.com/linear-expansion-coefficients-d_95.html

[74] "Tangram Technology Ltd. – Polymer Data File – PMMA," http://www.tangram.co.uk/TI-Polymer-PMMA.html

[75] K. R. Williams and R. S. Miller, "Etch Rates for Micromachining Processing," J. of Microelectromechanical Systems 5, 256 (1996)

[76] K. R. Williams, K. Gupta, and M. Wasilik, "Etch Rates for Micromachining Processing – Part II," J. of Microelectromechanical Systems 12, 761 (2003)

[77] H. Robbins and B. Schwartz, "Chemical Etching of Silicon II. The System HF, HNO_3, H_2O, and $HC_2H_3O_2$," J. of the Electrochemical Society 107, 108 (1960)

[78] H. Robbins and B. Schwartz, "Chemical Etching of Silicon I. The System HF, HNO_3, and H_2O," J. of the Electrochemical Society 106, 505 (1959)

[79] B. Schwartz and H. Robbins, "Chemical Etching of Silicon IV. Etching Technology," J. of the Electrochemical Society 123, 1903 (1976)

[80] B. Schwartz and H. Robbins, "Chemical Etching of Silicon III. A Temperature Study in the Acid System," J. of the Electrochemical Society 108, 365 (1961)

[81] J. Kim and K. B. Song, "Recent progress of nano-technology with NSOM," Micron 38, 409 (2007)

[82] A. Bek, “Apertureless SNOM: A New Tool for Nano-Optics,” Ph.D. thesis, EPFL (2004)

[83] M. Brehm, H. G. Frey, R. Guckenberger, R. Hillenbrand, D. Kazantsev, F. Keilmann, N. Ocelic, and T. Taubner, “Consolidating Apertureless SNOM,” J. of Korean Phys. Soc. 47, S80 (2005)

[84] D. W. Pohl and L. Novotny, “Near-field optics: Light for the world of NANO,” J. Vac. Sci. Tech. B 12, 1441 (1994)

[85] M. N. Islam, X. K. Zhao, A. A. Said, S. S. Mickel, and C. F. Vail, “High-efficiency and high-resolution fiber-optic probes for near field imaging and spectroscopy,” Appl. Phys. Lett. 71, 2886 (1997)

[86] T. Yatsui, M. Kourogi, and M. Ohtsu, “Increasing throughput of a near-field optical fiber probe over 1000 times by the use of a triple-tapered structure,” Appl. Phys. Lett. 73, 2090 (1998)

[87] V. P. Adiga, P. W. Kolb, G. T. Evans, M. A. Cubillos-Moraga, D. C. Schmadel, R. Dyott, and H. D. Drew, “Development of high-throughput, polarization-maintaining, near-field probes,” Appl. Optics 45, 2597 (2006)

[88] Y. C. Kim, D. W. Kim, M. Joo, S. S. Choi, and M. J. Park, “Characteristics of Light Transmission Through Nano-Apertures on Pyramidal Probes,” J. of Korean Phys. Soc. 50, 712 (2007)

[89] P. N. Minh, T. Ono, S. Tanaka, and M. Esashi, “Near-field optical apertured tip and modified structures for local field enhancement,” Appl. Optics 40, 2479 (2001)

[90] L. Wang and X. Xu, “High transmission nanoscale bowtie-shaped aperture probe for near-field optical imaging,” Appl. Phys. Lett. 90, 261105 (2007)

[91] L. Novotny, D. W. Pohl, and B. Hecht, “Scanning near-field optical probe with ultrasmall spot size,” Optics Lett. 20, 970 (1995)

[92] X. Wei, X. Luo, X. Dong and C. Du, “Localized surface plasmon nanolithography with ultrahigh resolution,” Optics Express 15, 14177 (2007)

[93] A. Salandrino and N. Engheta, “Far-field subdiffraction optical microscopy using metamaterial crystals: Theory and simulations,” Phys. Rev. B 74, 075103 (2006)

[94] Z. Jacob, L. V. Alekseyev, and E. Narimanov, “Optical Hyperlens: Far-field imaging beyond the diffraction limit,” Optics Express 14, 8247 (2006)

[95] X. Zhang and Z. Liu, “Superlenses to overcome the diffraction limit,” Nature Materials 7, 435 (2008)

[96] J. B. Pendry, “Negative Refraction Makes a Perfect Lens,” Phys. Rev. Lett. 85, 3966 (2000)

[97] J. B. Pendry and S. A. Ramakrishna, “Refining the perfect lens,” Physica B 338, 329 (2003)

[98] H. Rigneault, J. Capoulade, J. Dintinger, J. Wenger, N. Bonod, E. Popov, T. W. Ebbesen, and P.-F. Lenne, "Enhancement of Single-Molecule Fluorescence Detection in Subwavelength Apertures," Phys. Rev. Lett. 95, 117401 (2005)

[99] D. Gérard, J. Wenger, N. Bonod, E. Popov, H. Rigneault, F. Mahdavi, S. Blair, J. Dintinger, and T. W. Ebbesen, "Nanoaperture-enhanced fluorescence: Towards higher detection rates with plasmonic metals," Phys. Rev. B 77, 045413 (2008)

[100] J. Takahara, S. Yamagishi, H. Taki, A. Morimoto, and T. Kobayashi, "Guiding of a one-dimensional optical beam with nanometer diameter," Optics Lett. 22, 475 (1997)

[101] F. I. Baida, A. Belkhir, D. Van Labeke, and O. Lamrous, "Subwavelength metallic coaxial waveguides in the optical range: Role of the plasmonic modes," Phys. Rev. B 74, 205419 (2006)

[102] F. J. Garcia-Vidal, H. J. Lezec, T.W. Ebbesen, and L. Martin-Moreno, "Multiple Paths to Enhance Optical Transmission through a Single Subwavelength Slit," Phys. Rev. Lett. 90, 213901 (2003)

[103] S. Ramo, J. R. Whinnery, and T. Van Duzer, Fields and Waves in Communication Electronics, (John Wiley and Sons, New York, 1994)

[104] T. Ono, M. Esashi, H. Yamada, Y. Sugawara, J. Takahara, and K. Hane, "Integrated and Functional Probes," Nano-Optics, (Springer, Berlin, 2002)

[105] L. Novotny and C. Hafner, "Light propagation in a cylindrical waveguide with a complex, metallic, dielectric function," Phys. Rev. E 50, 4094 (1994)

[106] C. A. Pfeiffer, E. N. Economou, and K. L. Ngai, "Surface polaritons in a circularly cylindrical interface: Surface plasmons," Phys. Rev. B 10, 3038 (1974)

[107] Private communications with Steve Franz on April 21, 2008

[108] C. H. Sow, A. A. Bettiol, Y. Y. G. Lee, F. C. Cheong, C. T. Lim, and F. Watt, "Multiple-spot optical tweezers created with microlens arrays fabricated by proton beam writing," Appl. Phys. B 78, 705 (2004)

[109] T.-D. Onuta, M. Waegele, C. C. DuFort, W. L. Schaich, and B. Dragnea, "Optical Field Enhancement at Cusps between Adjacent Nanoapertures," Nano Letters 7, 557 (2007)

[110] Y. Wang and D. W. van der Weide, "Microfabrication and application of high-aspect-ratio silicon tips," J. Vac. Sci. Tech. B 23, 1582 (2005)

[111] J. R. Krogmeier and R. C. Dunn, "Focused ion beam modification of atomic force microscopy tips for near-field scanning optical microscopy," Appl. Phys. Lett. 79, 4494 (2001)

[112] Private communications with Sergey Prikhodko on April 29, 2008

[113] H. G. Frey, F. Keilmann, A. Kriele, and R. Guckenberger, "Enhancing the resolution of scanning near-field optical microscopy by a metal tip grown on an aperture probe," App. Phys. Lett. 81, 5030 (2002)

[114] T. H. Taminiau, R. J. Moerland, F. B. Segerink, L. Kuipers, and N. F. van Hulst, "λ/4 Resonance of an Optical Monopole Antenna Probed by Single Molecule Fluorescence," Nano Letters 7, 28 (2007)

[115] R. Fitzpatrick, "The Hertzian dipole," http://farside.ph.utexas.edu/teaching/em/lectures/node94.html

[116] R. P. Feynman, R. B. Leighton, and M. Sands, The Feynman Lectures on Physics Vol. 1, (Addison-Wesley, 1963)

[117] D. J. Griffiths, Introduction to electrodynamics, (Prentice Hall, 1999)

[118] T. C. Choy, "Capacitors can radiate: Further results for the two-capacitor problem," Am. J. Phys. 72, 662 (2004)

[119] L. Rayleigh, "On the Diffraction of Light by Spheres of Small Relative Index," Proceedings of the Royal Society of London. Series A, Containing Papers of a Mathematical and Physical Character 90, 219 (1914)

[120] D. R. Lide, CRC Handbook of Chemistry and Physics, (CRC Press, 1992)

[121] L. Novotny and B. Hecht, Priniciples of Nano-Optics, (Cambridge University Press, 2006)

[122] Y. Wang, W. Srituravanich, C. Sun, and X. Zhang, "Plasmonic Nearfield Scanning Probe with High Transmission," Nano Letters 8, 3041 (2008)